Closed-Loop Control of Constrained Flapping Wing Micro Air Vehicles

DISSERTATION

Garrison J. Lindholm, Captain, USAF

AFIT-ENY-DS-14-M-02

DEPARTMENT OF THE AIR FORCE
AIR UNIVERSITY

AIR FORCE INSTITUTE OF TECHNOLOGY

Wright-Patterson Air Force Base, Ohio

AFIT-ENY-DS-14-M-02

Closed-Loop Control of Constrained Flapping Wing Micro Air Vehicles

DISSERTATION

Presented to the Faculty

Graduate School of Engineering and Management

Air Force Institute of Technology

Air University

Air Education and Training Command

In Partial Fulfillment of the Requirements for the

Degree of Doctor of Philosophy

Garrison J. Lindholm, B.S.A.E.M., M.S.E.

Captain, USAF

March 2014

AFIT-ENY-DS-14-M-02

CLOSED-LOOP CONTROL OF CONSTRAINED FLAPPING WING
MICRO AIR VEHICLES

Garrison J. Lindholm, B.S.A.E.M., M.S.E.

Captain, USAF

Approved:

//signed//	3 Mar 2014
Dr. Richard G. Cobb	Date
Dissertation Advisor	
//signed//	3 Mar 2014
Dr. Mark F. Reeder	Date
Committee Member	
//signed//	3 Mar 2014
Dr. David R. Jacques	Date
Committee Member	

Accepted:

Dr. Adedeji B. Badiru	Date
Dean, Graduate School	
of Engineering and Management	

This dissertation is dedicated to the memory of my beloved father. It is you who exposed me at an early age to technology and encouraged me to push myself in life.

Acknowledgements

I would never have been able to finish my dissertation without the guidance of my committee members, help from classmates, and support from my family and wife.

First and foremost, I would like to express my thanks to my advisor, Dr. Richard Cobb, for your dedication and support in helping me complete this journey with you. As a mentor, colleague, and friend, your guidance has made this a thoughtful and rewarding journey. I would like to thank Dr. Mark Reeder and Dr. David Jacques for your time, guidance and support as I moved ideas to a completed study. I would also like to thank Mr. Jay Anderson and the entire ENY lab staff for your continuing support with equipment, space, and knowledge.

I would like to thank my classmates in the AFIT FWMAV group; LtCol Anthony DeLuca, Lt Nate Sladek, Lt Justin Carl, Lt Robert Lenzen, LCDR Zachery Brown, and Mr. Nelson Freeman who provided support and ideas on a daily basis, and without whom the keeping a handle on the ever changing lab configurations would have gotten extremely challenging.

Additionally, a large thank you is owed to Maj Michael Anderson and Maj Ryan O'Hara. Thank you for your guidance and willingness to share your knowledge of flapping wing micro air vehicle production and testing techniques. This knowledge not only gave me a jump start, but also a beginning point in this broad area of research.

I would also like to thank my family who was always supporting me and encouraging me with their best wishes.

Finally, I would like to thank my wife. She was always there to listen, support, and push, and was always by my side through the good times and bad.

<div align="center">Garrison J. Lindholm</div>

AFIT-ENY-DS-14-M-02

Abstract

Micro air vehicles have a maximum dimension of 15 cm or less, which makes them ideal in confined spaces such as indoors, urban canyons, and caves. Flapping wing micro air vehicles have an additional advantage over fixed wing or rotary wing micro air vehicles in that the flapping motion mimics birds and insects, thus concealing their appearance while also providing benefits of unsteady aerodynamics. Considerable research has been invested in the areas of unsteady and low Reynolds number aerodynamics, as well as techniques to fabricate small scale prototypes. Control of these vehicles has been less studied, and most control techniques proposed have only been implemented within simulations without concern for power requirements, sensors and observers, or actual hardware demonstrations. In this work, power requirements while using a piezo-driven, resonant flapping wing control scheme, Bi-harmonic Amplitude and Bias Modulation, were studied. In addition, the power efficiency versus flapping frequency was studied and shown to be maximized while flapping at the piezo-driven system's resonance. Then prototype hardware of varying designs were used to capture the impact of a specific component of the flapping wing micro air vehicle, the passive rotation joint. The passive rotation joint was optimized through a range of different angle of attack stops and rotation joint stiffness to maximize lift and thrust force development. Optical tracking software was then developed to provide feedback information for use in closed-loop control experiments. Finally, closed-loop control of different constrained configurations were demonstrated using the resonant flapping Bi-harmonic Amplitude and Bias Modulation scheme with the optimized hardware. This work is important in the development and understanding of eventual free-flight capable flapping wing micro air vehicles.

Table of Contents

List of Figures

xiii

List of Tables

List of Abbreviations

Closed-Loop Control of Constrained Flapping Wing Micro Air Vehicles

I. Introduction

1.1 Motivation

Unmanned aerial vehicles (UAVs) have become critical to the modern warfighter. They provide an ideal platform to perform the mundane or dangerous missions without putting the operator at risk. They are used as intelligence, surveillance, and reconnaissance (ISR) platforms, strike vehicles, and command and control (C2) communication nodes.

Micro air vehicles (MAVs) have started to play a greater role in the modern combat environment as well, particularly in the area of ISR. Flapping wing MAVs (FWMAVs) are in development to extend the MAVs capabilities. FWMAVs offer several advantages over fixed and rotary wing MAVs. Specifically, they offer the superior agility similar to a rotary wing MAV combined with a low acoustic and small visibility signature that tends to hide in plain sight by resembling insects.

1.2 Research Challenges for Flapping Wing Micro Air Vehicles

There are many challenges to developing an operational FWMAV. The following areas present challenges to a prospective FWMAV designer. Aerodynamics of the FWMAV regime is not entirely understood. Effects, such as leading edge vortex (LEV), delayed stall, clap and fling, and other low Reynolds number and unsteady effects are being explored but not yet fully explained. Predicting FWMAV stability, performance, and fluid-structure interaction for use in FWMAV development currently offers a challenge to any FWMAV designer.

The micro fabrication and design process is another challenging aspect to FWMAV design. Most tools used today are intended for larger macro fabrication or for

nano-scaled devices used in the semiconductor industry. The FWMAV designer has to use a blend of these two very different tool sets in order to manufacture FWMAVs repeatably, quickly, and cheaply. Power storage and amplification circuitry is a large, weight limiting factor, and without significant advancement it will limit the payload, flight time, and capabilities of any future operational FWMAV.

Last, minimally actuated, minimum power controllers, capable of stabilizing the FWMAV in a hover as well as through maneuvers, have yet to be developed and demonstrated. To make this challenge more difficult, many FWMAV platforms lack on-board sensors, which would typically provide feedback information for a prospective controller.

The research challenges for designing and operating a FWMAV are numerous; but significant progress has been made. Demonstrations of power-tethered[1] uncontrolled flight have been performed, advances in aerodynamics have come closer to explain the aerodynamics of the small scale, manufacturing techniques and process have evolved so that fast and efficient prototyping can be performed. However, demonstration of a control scheme capable of autonomously stabilizing a power-tethered FWMAV has yet to be demonstrated and will be the focus of this research. Different constrained configurations were used as demonstrations to future control cases for the FWMAV. The additional challenge is to demonstrate such control using as few actuators as possible to minimize weight of the FWMAV, and have the control algorithm optimized for power consumption to maximize flight time. In addition, providing feedback signals for the controller is required, and current prototypes lack sensors traditionally used for feedback.

1.3 Problem Statement

The goal of this research is to develop a two wing, two actuator biomimetic FWMAV prototype capable of power-tethered constrained flight and use this prototype as

---

[1]Power-tethered refers to the use of an off-board power supply and power amplifiers. Miniaturized power systems is a necessary, but separate research area.

a testbed for FWMAV control research. Specifically, the control research will focus on a minimum actuated, minimum power consumption controller capable of stabilizing the FWMAV in different constrained configurations by only closing the loop on the FWMAV as a whole, and letting the wings themselves be controlled by an open-loop controller.

> *Thesis statement: Open-loop wing control combined with closed-loop control about FWMAV position and pose is sufficient to stabilize a minimally actuated, power-tethered FWMAV in constrained configurations.*

1.4   Assumptions and Limitations

There are some assumptions and limitations made in the course of this research. First, all hardware prototypes were to be driven with piezoelectric actuators. This was done as it is assumed at the scale of work, that piezoelectric actuators would be more efficient than rotary DC motors, typically used in larger FWMAVs. Next, it was assumed that cycle-averaged forces and moments were adequate to study when designing controllers based on stabilizing and controlling the FWMAV as a whole system. This is in contrast to examining forces and moments within the flapping wing cycle, typically done in flapping wing aerodynamic research.

Only commercial actuators were used in the course of this research. This was done in order to reduce the variability of custom made actuators and also minimize prototype production time. This limited the FWMAVs produced by increasing their size and weight significantly, when compared to custom actuators, and thus reducing their performance. Finally, due to the size of power amplification equipment and the controller used, there would be wires providing the drive signals to any hardware prototypes. This limited the dynamic capability of these prototypes by adding additional weight and undesirable spring-like resistance.

1.5 *Expected Contributions*

There were numerous expected contributions to the field of FWMAVs. First, power measurements were made and presented for both varying flapping frequencies and control parameters. These measurements provide prospective FWMAV designers with first-order numbers on how large a battery will need to be sized. They also should show the most efficient flapping frequency and which control parameters use the most power.

Next, improvements to the current prototype design were to be made, specifically in the passive rotation joint. Two elements were to be examined and optimized for lift and thrust production. Increasing these forces should lead to better performing FWMAV. Also, a FWMAV would be designed that would incorporate a biomimetic *Manduca Sexta* wing for the first time. This serves to combine previous work into one unified design.

It was expected that performing constrained closed-loop demonstrations would be made using an open-loop wing trajectory controller. Previously, this controller was used statically and shown to have direct influence on 5 of the 6 degrees of freedom of a FWMAV. The next step in the development of this control scheme was to use it in dynamic closed-loop demonstrations. In order to accomplish these closed-loop demonstrations, some form of feedback was required. It was expected an off-board camera based tracker would provide sufficient feedback data to perform the closed-loop demonstrations.

Last, through the production of many hardware prototypes it was expected additional knowledge of manufacturing techniques and methodologies would be found. These techniques and methods are included in this document to help future FWMAV researchers.

1.6 *Document Overview*

A thorough review of previously reported background work is provided in Chapter II including the development of the algorithm that is used to control the wing stroke function. Then, Chapter III will detail the different hardware experiment testing methods used to collect the data that are presented later. Chapter IV presents the results of the studies conducted on the electrical power requirements of the control algorithm and the electrical power efficiency of piezoelectric actuator driven flapping mechanisms. Chapter V details the design study of the passive rotation joint and the results of the lift and thrust generation optimization done on two different components of the passive rotation joint. In Chapter VI the development of the optical trackers used to provide feedback data for the closed-loop control experiments is presented. Chapter VII presents the results of the constrained, closed-loop control experiments performed. Finally, in Chapter VIII research conclusions, contributions, and recommendations for future work will be discussed.

II. Background and Literature Review

This chapter presents a study of topics relevant to FWMAV control research. It covers some of the fundamental research in the field of flapping wing aerodynamics in order to give an understanding of the forces and moments influencing a FWMAV. Next, the construction techniques for creating a bio-inspired FWMAV are examined. Designing and constructing at the scale of a FWMAV proposes unique challenges when compared to traditional aircraft construction and must be well understood in order to produce prototypes for FWMAV control experimentation. Finally a review of FWMAV stability and control literature is provided to establish a starting point for research proposed in this document.

2.1 Flapping Wing Aerodynamics

In 1984, a review of previous flapping wing aerodynamic work and some impacts on the validity of quasi-steady approaches to flapping wing aerodynamics was done [2]. Specifically, it was found that as forward flight velocity increased, the quasi-steady approach is valid. But as forward flight velocity drops to zero, the quasi-steady approach consistently under predicts forces and moments for the class of flapping wing fliers that makes up most insects and hummingbirds. Large bird and butterfly "clap-and-fling" classes of flapping wing fliers have different results due to their dissimilar methods of creating lift. In this work we are more concerned with the aerodynamics of the non-clap-and-fling insects and hummingbirds, which take advantage of LEV, delayed stall, and wake capture.

Later, Ellington reviewed the low Reynolds number and unsteady lift mechanisms identified to date for several insect species [3]. He identified design ratios linking insect wing area, flapping frequency, body weight, and forward velocity to each other. Finally, he identified wing trajectories of insects and how they impact insect flight trajectory, essentially learning how insects control their flight trajectories. Insect passive pitch stability due to the body acting like a pendulum is identified along with the insect changing the stroke plane by modifying the mean flapping angle.

Combining the passive pitch stability technique with asymmetric angle of attack for a flapping cycle is the process by which the studied insects transition from hover to forward flight with the stroke plane angled proportionally to the forward flight speed. The angle of attack variation within the flapping cycle is very similar to a technique that is used in this research, split-cycle wing trajectory, which will be reviewed in section 2.3.

Studies into the effects of the wing flip at the end of each flapping cycle were performed in [4, 5]. A dynamically scaled, mechanically driven wing was used to measure lift and drag as different flapping parameters were varied. It was found that angle of attack, flip duration, and flip timing relative to stroke reversal play a major role in the lift generation and lift to drag ratio. This result motivated the study in Chapter V on optimizing the passive rotation joint of the prototype FWMAV with the goal of generating more lift. The passive rotation joint is the only component in the current FWMAV design capable of influencing the angle of attack, through limit stops, flip duration, joint stiffness, flip timing, and joint position relative to the wing.

A mechanical flapper was created and used to model both the steady and unsteady aerodynamic forces and moments in [6]. The primary goal was to create a methodology to measure and model the aerodynamics for use within a FWMAV design and development framework. The technique presented could be repeated for any given wing design and flapping trajectory to build up an aerodynamic model for a given flapping wing mechanism.

In [7] Ansari et al. compiled an in-depth review of techniques used to model flapping wing aerodynamics. They went through the various methods: steady-state, quasi-steady, semi-empirical, and unsteady, and found that blade-element predictions are more accurate as free-stream velocity is increased, but poor in slow speed and hover. They reviewed the important flow-field structures such as the LEV, wake capture, and clap and fling mechanisms. After the review of previous work, they detailed their previously proposed unsteady solution that uses a quasi-3D approach

and throws away small-angle approximations. They compared the model's predictions to measured forces of a hawk moth and fruit fly reported previously. The model was reported to be the best performing model that had been seen to date.

In [8] Adity and Malolan documented their experiment of testing a FWMAV in a wind tunnel and attempted to see how Strouhal number effects the peak thrust forces developed. They provide details on the test configuration and custom force balance. They used a DC motor to drive a 4-bar mechanism to create the flapping motion. Their MAV design did not include any sort of rotation, passive or otherwise. They found that there is a small range of Strouhal numbers that provides best force development for given configuration and free-stream velocity. In the case of the paper, Strouhal numbers were typically in the 0.1-0.4 range with lower speeds corresponding to higher Strouhal numbers. Strouhal number is defined in Eq. (2.1) where: f is flapping frequency, A is max tip displacement, b_{semi} is the semi-span, U_∞ is the free-stream velocity, and ϕ_{max} is the max flapping stroke angle.

$$S_N = \frac{fA}{U_\infty} = \frac{2fb_{semi}\sin\left(\frac{\phi_{max}}{2}\right)}{U_\infty} \tag{2.1}$$

Whitney and Wood derived a thorough analysis of the mechanics of passive rotation as it pertains to flapping wing flight in [9]. They went through the non-dimensional parametrization of a wing and found that by defining radius moments there is a correlation between the first, center of area, and second radius moments for insect wings. This points to insects, through thousands of years of subtle changes, having an optimal distribution of area for a flapping wing. They then analyzed the kinematics of flapping with a passive rotation joint. Three angles are used to describe the wing position as it flaps: ϕ the flapping angle, ψ the rotation angle, and θ the deviation angle. For their work, they found that the deviation angle can typically be assumed to be zero. The angular velocity for a flapping wing was found by the sum

of the flapping, rotation, and deviation velocities seen below.

$$\boldsymbol{\omega} = -\dot{\phi}\boldsymbol{e}_{X'} + +\dot{\theta}\boldsymbol{e}_{z''} + \dot{\psi}\boldsymbol{e}_{x}, \tag{2.2}$$

where the X', z'', and x axes are all defined in Figure 2.1.
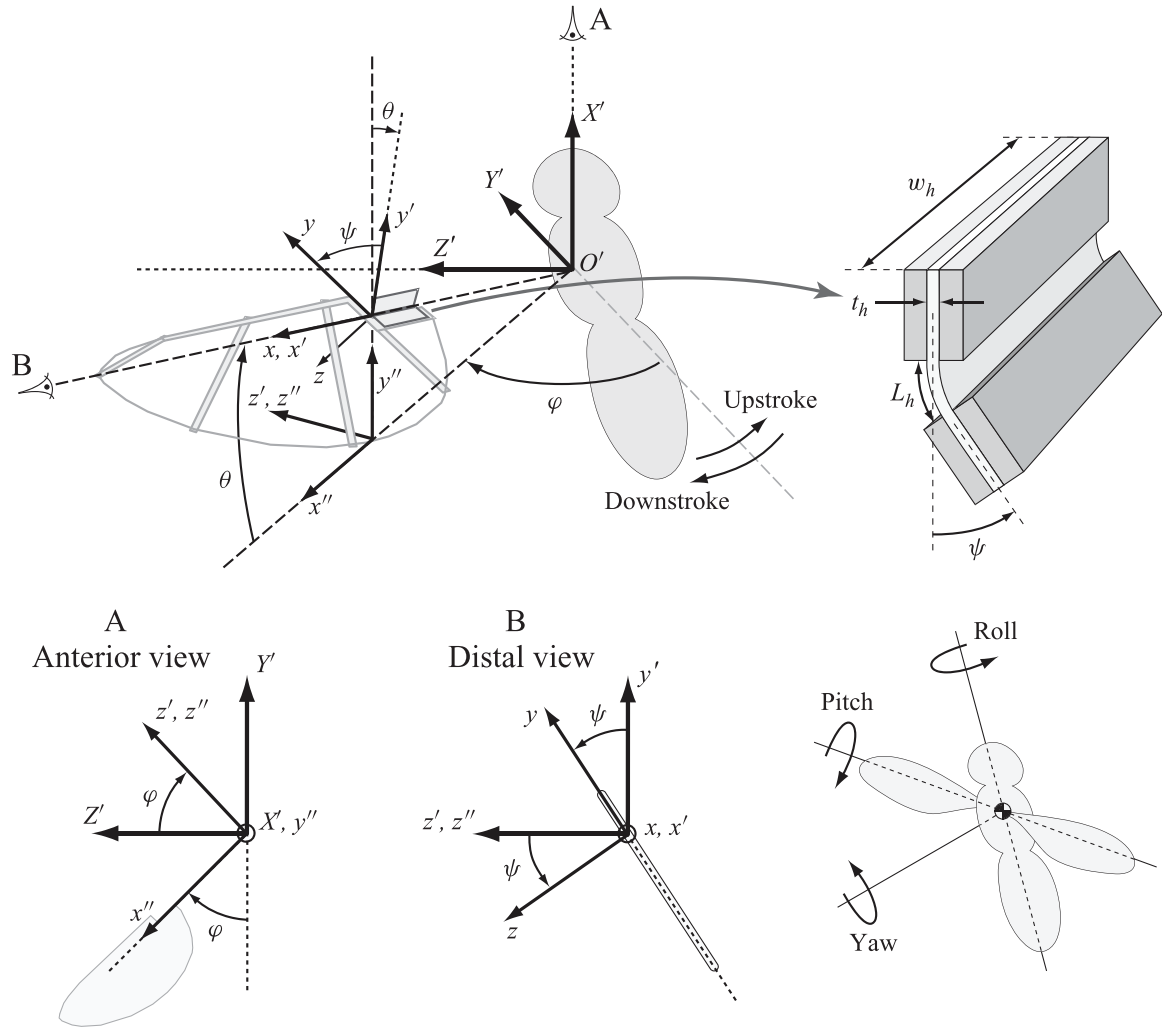
Figure 2.1: Coordinate systems and angles used to specify wing kinematics. All coordinate frames share the same origin, O'. An example passive rotation hinge is shown. A driving spar would be mounted to the top of the hinge and the wing would be mounted to the bottom [9].

9

For the wing bound frame Eq. (2.2) becomes:

$$\boldsymbol{\omega} = \left(\dot{\psi} - \dot{\phi}\sin\theta\right)\boldsymbol{e}_x + \left(-\dot{\phi}\cos\theta\cos\psi + \dot{\theta}\sin\psi\right)\boldsymbol{e}_y + \left(\dot{\phi}\cos\theta\sin\psi + \dot{\theta}\cos\psi\right)\boldsymbol{e}_z \quad (2.3)$$

They state aerodynamic forces and moments are not directly related to the angle of rotation, ψ, but rather to the angle of attack, α, defined as the angle between the wing chord and the instantaneous local velocity:

$$\alpha = \text{atan2}\left(-\omega_y, \omega_z\right) \quad (2.4)$$

Using linear elastic beam theory, the stiffness of the passive rotation hinge is approximated by:

$$\kappa_h = \frac{E_h t_h^3 w_h}{12 L_h}, \quad (2.5)$$

where t_h, w_h, and L_h are the thickness, width, and length of the middle layer of the hinge and E_h is the modulus of the middle layer material. Next, they developed the passive rotation equations of motion. They made the assumption of a thin wing allowing $I_{xz} = I_{yz} = 0$ and using the perpendicular-axis theorem, $I_{xx} + I_{yy} = I_{zz}$ giving the resulting equation of motion

$$M_x = I_{xx} + \left(\dot{\omega}_x + \omega_y \omega_z\right) + I_{xy}\left(\dot{\omega}_y - \omega_x \omega_z\right). \quad (2.6)$$

Assuming there is no out-of-plane motion, $\theta = 0$, it simplifies to

$$I_{xx}\ddot{\psi} = M_x + I_{xy}\ddot{\phi}\cos\psi + \tfrac{1}{2}I_{xx}\dot{\phi}^2\sin 2\psi, \quad (2.7)$$

where M_x includes the aerodynamic moments and the elastic restoring moment due to the wing hinge. Now given $\phi(t)$ and $\theta(t)$, a model of aerodynamic torque, a model for the elastic wing hinge, and the inertia terms I_{xx} and I_{xy}, Eq. (2.7) can be integrated in time to determine the passive rotation angle $\psi(t)$. Next, they derived a blade-element model to provide a model of aerodynamic torque. They concluded that calculating and

10

measuring the rotational moment is very difficult due to the sensitivity of the location of the center of pressure. They then showed a model for aerodynamic damping of the rotation joint. Without this additional model they found their calculations were severely under-damped when compared to experimental results. Next, they show a model for "added-mass effects" to improve their model of the moments about the hinge further. They then went into detail about their experiment setup using stereoscopic reconstruction to capture the wing motion variables, ϕ, ψ, and θ, of their prototype flapping mechanism. They also measured lift generated by the flapper. Next, they compared the measured wing position to the predicted location based on the models and equation of motion presented earlier. They found very good agreement with wing position and predictions. They also compared the predicted lift to measured lift and found good agreement there as well. Last, they repeated their experiment using a split-cycle input. Their wing kinematic model continued to find good agreement with experimental data and they saw very little reduction in lift when using the split-cycle input. They did not, however, have a sensor to measure the thrust generated by the split-cycle input.

Particle image velocimetry (PIV) data and thrust measurements were collected across a range of Reynolds numbers and flapping wing trajectories [10] and later in [11]. From the data collected at the *M. sexta* Reynolds number, the optimal angle of attack limit stop was found to be near 30 degrees. Work shown in Chapter V will test this result on actual hardware, as opposed to larger scaled devices tested in equivalent Reynolds number ranges, with the goal of finding the optimal angle of attack limit stop for lift generation.

2.2   *Construction of Bio-inspired Flapping Wing Micro Air Vehicles*

In [12], Yan et al. detailed the design and construction of a 5-bar spherical transmission to be used on a micromechanical fly. The transmission was driven by a piezoelectric actuator and there was a load cell placed on the transmission in an attempt to measure forces to be used for tracking the wing within the cycle. They then

briefly discuss a controller to drive the wings in a closed-loop fashion. This is all early work done on the UC Berkeley Micromechanical Flying Insect project. Later versions of the micromechanical flying insect moved to a double 4-bar per wing setup, where each 4-bar is driven by an actuator pair and the 4-bars drive the forward and aft wing spar independently allowing control of the stroke angle and angle of attack [13–16]. This design showed promise, however, the additional actuator requirements along with the weight of the double 4-bar transmission led the researchers to other transmission designs detailed below.

In [17] Avadhanula et al. refined the design presented in [12] with the goal of improving the lift force generated. The main change to their design at this stage was an improved implementation of the thorax, or transmission. Fewer flexures were needed to implement the spherical 4-bar joints that make up the 5-bar transmission. This increased stiffness and provided more power to the wing, and also improved manufacturing time due to decreased parts. They also present a quasi-static aerodynamic model for the flapping wing. The last major change in design was no longer seeking to close the loop on wing tracking and now using an open-loop control strategy for driving the wings. They then tested the proposed design measuring lift and wing deflection and then compared them to predictions. The results compared favorably to predictions, and they also reported enough lift was generated to attempt flight for the first time.

Efficiency of electric motors is known to decrease as they are miniaturized, due to friction in the gearbox becoming more significant as the scale of the work shrinks. The scale of the prototypes lend themselves to using piezoelectric driven FWMAVs [18]. Wood et al. derived the optimal energy density and nonlinear performance limits for a piezoelectric bending actuator in [12, 19]. They found the ideal actuator was not feasible due to load concentrations at the tip of the triangular shaped piezoelectric ceramic, and used a near optimal design with a width ratio of 1.5 and a extension ratio of 1. The thickness ratio used was 0.35. They then derived equations relating displacement and blocking force requirements to a length and width. Last, they dis-

cussed different electrical drive configurations and found that a dual-source bias drive configuration gives the best performance, as it allows a greater field drive. They conclude by stating the four techniques that improved the energy density of the actuators: width tapering, extension, high performance materials, and high field drive.
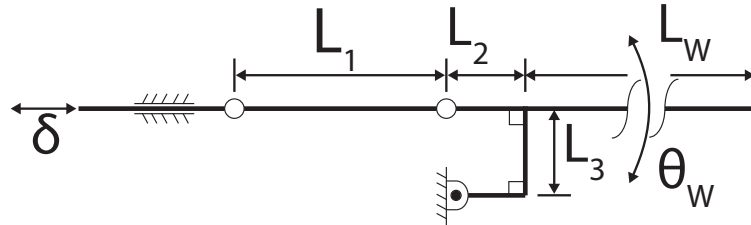
Figure 2.2: Diagram of 4-bar linkage. δ represents the actuator input and θ_W represents the wing stroke angle.

In [20] Wood detailed the process of design, fabrication, and analysis of a proposed FWMAV. This design used a 4-bar transmission tied to a passive rotation joint to achieve the desired wing motion. The kinematics defined by the 4-bar mechanism, shown in Figure 2.2, are:

$$\theta_w = \arccos\left(\frac{\delta^2 - 2\delta L_1 + 2L_3^2}{2L_3\sqrt{(L_1 - \delta)^2 + L_3^2}}\right) + \arctan\left(\frac{L_3}{L_1 - \delta}\right) - \frac{\pi}{2} \tag{2.8}$$

This equation was found useful in analyzing the system, but less useful in design due to its complexity. What was desired was a ratio relating the output angular displacement to the input linear displacement. They assumed δ and θ_w were small and then made the following approximation:

$$T \equiv \frac{\theta_w}{\delta} \approx \frac{1}{L_3} \tag{2.9}$$

This now allows L_3 to be determined for a desired angular displacement given a linear input. Typically it is desired for L_3 to be as small as feasible thus increasing the transmission ratio, T. They then discuss sizing of L_1, done by observation of Eq. (2.8) and of L_2, small as feasible. Next, they derived a model to predict the resonance of

13

the system made up of the wing and transmission. It was found that for a linearized system, the system resonance is defined by a function of equivalent stiffness, k_{eq} detailed in [21], inertia of the mass of the wing, J_{yy}, and inertia of the apparent mass from the air, J_{air}:

$$\omega_n = \sqrt{\frac{k_{eq}}{J_{yy} + J_{air}}} \tag{2.10}$$

Additional work found that simply maximizing the transmission ratio is not the ideal case [22]. Using a lumped linear model, it was found that designs with maximized transmission ratios would have lower resonant frequencies and therefore lower lift. So what is desired to be maximized is the characteristic velocity of the wing as the product of the stroke amplitude and the resonant frequency:

$$\dot{\phi} = |\phi|\,\omega_d \tag{2.11}$$

where ω_d is the resonant system frequency calculated by using Eq. (2.12).

$$\omega_d = \sqrt{\frac{m_a + T^2 J_\phi}{k_a + T^2 k_t}} \sqrt{1 - \frac{b_{eq}^2}{4\left(m_a + T^2 J_\phi\right)\left(k_a + T^2 k_t\right)}} \tag{2.12}$$

where m_a, J_ϕ, k_a, k_t, and b_{eq} are actuator mass, wing inertia, actuator stiffness, transmission stiffness, and equivalent damping respectively. These values are found by using the linear lumped parameter model and fitting experimental data to these parameters as described in [22]. By using models that predict these parameters for the actuator and transmission, the transmission design can be optimized for maximum lift generation for a given wing design.

Next, the passive rotation was designed. The passive rotation hinge was designed such that the geometry limits the flexure joint motion and thus max angle of attack. A function was presented that predicts the maximum geometric angle of

attack from the length of the flexure, L_f and thickness of structural component, t_s.

$$\phi_{max} = \frac{\pi}{2} - \frac{L_f}{t_s} \tag{2.13}$$

They also presented a function predicting the resonance of this passive rotation joint from the stiffness of the rotation joint and the inertia of the wing:

$$\omega_r = \sqrt{k_r/J_{xx}} \tag{2.14}$$

Additionally, they noted that quasi-static passive wing rotation will only occur with a wing drive frequency significantly below w_r. Next, they presented brief notes on the actuator, fabrication methodology, and resulting forces developed. They concluded the design has merit and warn that a potential future MAV will have stability and control issues and that there is a trade off between complexity and the ability to control a potential FWMAV.

Wilson and Wereley did a study of lift force generation and power requirements for a range of wing and transmission designs with an emphasis in predicting the power requirements for hover using rotary electric motors as the driving actuator [23]. Their conclusion states that a stiffer wing spar and wing membrane lead to typically higher values of generated lift and that, as expected, higher frequencies tend to generate greater lift than lower frequencies. Their testing was limited by materials to testing done at or below 30 Hz.

In [21] Wood et al. detailed their novel methodology of constructing MAV scale devices using a system they call smart composite microstructures (SCM). SCM consists of using a stack of different thin materials, which have all been cut according to schematics using precision laser manufacturing, bonded together and then cut free from its frame. The freed piece can then be folded along flexures as required and glued into the desired shape. This allows a 2.5D technique to create 3D objects with very high precision and minimal time. They then went into detail about creating a 5-bar

15

and 4-bar mechanism using this technique and some of the design considerations when making these devices. They also discussed the inclusion of piezoelectric ceramics into SCM as well as conductive layers to act as wires, without causing binding on any flexible joints. Last, they showed an example MAV and a micro crawling robot created using the technique. Using SCM, Wood created the first takeoff of a biologically inspired at-scale insect, detailed in [24]. Design techniques and construction of some of the components is discussed along with the power densities of the actuator used along with the final vehicle, $>150\text{Wkg}^{-1}$ and $>100\text{Wkg}^{-1}$ respectively. The MAV had a thrust to weight ratio of approximately 2 and was guided by wires to restrict movements in undesired directions. The MAV was also power-tethered, as previously defined. Finally a predicted distribution of total MAV mass is presented, leading to the ultimate goal of a free-flight fully autonomous flying robotic insect.

Oppenheimer et al. proposed a control scheme called Split-Cycle Constant-Period Frequency Modulation with Wing Bias for use with a FWMAV that has only two actuators [25–27]. Previous work showed the ability to control a FWMAV using a similar technique; however, they used an additional third actuator to control the vehicle's center of gravity [28]. In both efforts, instantaneous and cycle-averaged aerodynamic models, stability and control derivatives, and a simulation environment to demonstrate the schemes were created. It was shown that these control approaches can be utilized to provide 6 degrees of freedom (DOF) control of a FWMAV similar to the one discussed in [24] with either 2 or 3 actuators. All results were based on the simulation and models that were developed using quasi-steady based approaches to modeling the aerodynamics.

Anderson et al. detailed the process of designing and fabricating a FWMAV at insect scale, though larger than had been demonstrated in the past. They used a modified form of the SCM described earlier with process changes emphasizing repeatability in manufacturing by removing human error from the process [29]. They also discussed initial testing of prototypes produced using these techniques.

Recently, techniques have been demonstrated that provide rapid production, without a highly skilled technician for the assembly process. [30] The key to the technique is to create a monolithic design with all FWMAV components included along with 4-bar alignment and rotation joints to position the FWMAV components as the overall layup is moved through a predefined 1 DOF motion. After expansion, the FWMAV joints are secured and the scaffolding and alignment tools are removed with laser micro machining. This process demonstrates that once a FWMAV design is set, FWMAV can be created quickly, inexpensively, and in large numbers. The key challenge to this technique is creating the alignment and rotation joints for a given design. Tools have yet to be developed to assist the design engineer in this task.

In recent years a great deal of work has been done on creating a wing using the SCM design and manufacturing process that matches the structural dynamic properties of a *M. sexta* forewing [31–34]. The research used finite element modeling, system identification, and biological materials properties research in order to create a detailed structural model of a biological wing. Then a wing was engineered to match the structural properties and create significant lift. This engineered wing will be used as the starting point in designing the next Air Force Institute of Technology (AFIT) prototype FWMAV.

2.3   Stability and Control of Flapping Wing Micro Air Vehicles

Insect aerodynamic models were used along with insect inertial terms to develop a linearized model for the desert locust, *Schistocerca gregaria* [35]. The techniques to develop the aerodynamic model placed emphasis on eliminating as much of the natural control system of the insect in order to obtain an open-loop model with as little control influence possible. The authors describe this as a "broken-loop" model. After the model was developed, classic linear analysis was performed to determine the system's stability. The resultant eigenanalysis showed a positive real-root complex pair, a fast negative real-root, and a slow real-root. This shows that the system is longitudinally unstable without some sort of active control. Monte Carlo simulations

17

were done to analyze any effects of error within the linearized model. Five thousand test cases were run with random perturbations on the aerodynamic model terms. The simulation result showed constant unstable oscillatory pairs with two stable first-order poles.

Later, work was performed comparing a linear time invariant analysis approach to one using a nonlinear time periodic approach in [36]. Taylor, Bomphrey, and Hoen found that when the insect's flapping frequency is less than ten times faster than the slowest mode, the linear time invariant approach loses effectiveness. The proposed nonlinear time periodic approach followed from rotary aircraft theory. They found that the resulting system can only be stabilized within stable limit cycles and that control of such a vehicle would involve moving from one stable limit cycle to another. Of course they were studying one of the larger flight capable insects, the desert locust, and it correspondingly has a slower flapping frequency. Later, studies performed on the hovering bumblebee [37] and hoverflies [38] used the linear time invariant approach to modeling the longitudinal flight dynamics, again minimizing the effects of the insects active control. Both these studies saw the same modes with one unstable complex pair and two stable real roots. This demonstrates that using cycle-averaged forces and classical linear analysis approach can give consistent results for FWMAV class problems.

The mathematical modeling and subsequent control for a proposed micromechanical flying insect was detailed in [39, 40]. The modeling section of the work details a multi-part simulation environment which includes models for aerodynamics, sensors, actuators, and body dynamics. This model was then used for a multi-tiered control study, where the controller was split into three parts; wing trajectory, flight mode stabilizer, and navigation. The final control "actuators" were the left and right wing trajectory kinematic parameters. Hardware-based FWMAVs would typically have less control over wing trajectory due to weight limitations and minimally actuated systems. The control approach was to split the dynamics into slow and periodic components. Averaging was then used to remove the higher frequency periodic dynamic effects. Fi-

18

nally, linear quadratic regulator (LQR) and linear quadratic Gaussian (LQG) control approaches were used to stabilize the system with full state information and stabilize the system in the presence of imperfect information by use of noise added to sensor dynamics. The simulation showed stable motion and fast response to perturbations; however, analysis was limited only to the longitudinal dynamics.

A time-averaged based approach to longitudinal FWMAV control was done in [41]. The aerodynamics of the system were approximated by a Fourier series which allowed the aerodynamics to be split into slow changing parameters and periodic, fast changing parameters. The slow changing parameters were used with a nonlinear control law to stabilize the longitudinal dynamics of the system. The control law was then tested with a high fidelity simulation including the higher-order aerodynamic terms. Longitudinal stability and control was demonstrated within this simulation.

The subject of open-loop stability of a hovering FWMAV was studied in [42]. Bolender derives two sets of nonlinear longitudinal equations of motion, point-mass and three degrees-of-freedom multi-body model, using a blade-element aerodynamic model. He used Floquet theory and showed that the FWMAV was open-loop unstable. An analytical solution was presented for the simple point-mass case, and a numerical solution was found for the three degrees-of-freedom model. He concluded that additional degrees-of-freedom and higher fidelity aerodynamic models should be investigated as it may change the result of his analysis.

The longitudinal linear dynamics about a hover were derived for the FWMAV in [43]. The aerodynamics used in this study are based on quasi-steady aerodynamic models. Two different models were developed. The first model used the insect's halteres as a stability augmentation system, while the second did not use halteres. The model with the halteres providing rate feedback was found to be statically stable. However, the model lacking the rate feedback was found to be statically unstable, with the result being one unstable complex pole and two stable real poles. In a similar study, the lateral-directional linear dynamics about a hover were derived for

19

a FWMAV [44]. Again, the quasi-steady approach to approximate the aerodynamics was used. The resulting linear lateral-directional system was found to have two stable real poles and two nearly unstable complex poles. The simulations used to generate data included a model of the halteres to provide roll-based feedback, which was key in keeping the models near the equilibrium point.

A complete six DOF simulation was developed and used as a starting point for FWMAV control research done in [45]. The complex model was based on both computational fluid dynamics and experimental results. The initial goal was to develop a longitudinal control algorithm, thus the lateral-directional states were held fixed and the complex model was simplified to just the longitudinal states. However, the system was still more complex than desired for control algorithm development. To simplify the model, a time-averaged approach was used. The simplified model consisted of two states and two control parameters, stroke angle and rotation angle, which were symmetric for both wings. A controller was then developed using these parameters that stabilized the FWMAV in hover, low-speed flight, and altitude change. Then the controller was used with the full fidelity simulation, while keeping the lateral-directional terms constant, and control was demonstrated using the simplified model controller. This result demonstrates, in software, that a time-averaged approach to FWMAV control, as shown in Chapter VII, is feasible. Of course, this study also had direct control of the FWMAV wing trajectory, something that a minimally actuated hardware-based FWMAV will not have. Numerous other examples of similar studies have been performed as simulated models and direct control of the wing kinematics [46–54].

A hardware based FWMAV, *Golden Snitch*, was demonstrated with altitude control using a off-board stereo vision system to provide navigational data [55]. The vehicle has tail surfaces for use as stability and control, and as such the demonstration was done not in a hover, but with a constant forward velocity. The approach used was to linearize the system about the steady cruise condition and use the linearized plant model and classical feedback control to design the controller. This demonstrates

that when properly linearized, classical control techniques can be applied to FWMAV control problems as shown in Chapter VII and that vision-based systems can provide adequate feedback parameters for use in FWMAV control as developed in Chapter VI.

Attempts to control the altitude of a FWMAV were demonstrated in [55, 56] by using an adaptive feedforward based approach. The feedforward approach was used due to the weight limitations of current FWMAV prototypes prohibiting the use of a sensor for altitude based feedback control. A single actuator driven FWMAV was used for the development and testing of the control scheme. The fundamental approach used was to map the displacement of the actuator to the average lift force generated. Using this mapping, adaptive control laws were developed to track an altitude trajectory. Both amplitude modulation and frequency modulation approaches were demonstrated. The challenge still remains to control the altitude of a FWMAV while simultaneously maintaining control over the other DOF of the FWMAV.

Successful altitude control of a FWMAV was first demonstrated in [57]. The technique to control the FWMAV was a two-step process. First, system identification was performed on the input-output combination of the actuator to lift generation, and second, a linear time invariant control law was developed. The demonstrated flight required guide wires constraining the FWMAV to motion in the vertical plane only and prohibited the FWMAV to change orientation, similar to experiments described in Chapter VII. One of the primary conclusions of this effort was to ignore the complex dynamics and aerodynamics of the FWMAV system and instead treat it as a black box with known input-output relationships. The work also suggests that the closed-loop gains can be found experimentally as was done in section 7.1 or through the use of a linearized model as proposed in section 7.2.

Many other prototype demonstration flights have been accomplished [58–61]. These demonstrations have, up to this point, been accomplished with one or more of the following limitations: tethered for power or stability, significant passive stabilization augmentations, or with a traditional aircraft tail for use in stability and control

loops [57, 60, 62–65]. The majority of these vehicles are driven using electric rotary motors and many also use a four wing clap-and-fling design. The research herein differs in that the FWMAV will use a minimal actuated configuration consisting of just two piezoelectric actuators. The next section describes a unique open-loop wing trajectory controller used to drive each actuator and thus each wing separately.

2.4 *Bi-harmonic Amplitude and Bias Modulation Controller*

In [1, 66–68] Anderson et al. developed a novel control technique for FWMAVs, Bi-harmonic Amplitude and Bias Modulation (BABM). The technique shows promise and has been demonstrated to have direct influence on five DOF of a FWMAV's six DOF. Control of the sixth DOF can be achieved indirectly by yawing or rolling the vehicle first. The controller is based around modulating three wing stroke angle parameters, amplitude, bias, and split-cycle. Each wing can be modulated independently giving six total parameters. These parameters are varied continuously by a control law to control the FWMAV. The BABM control scheme is used in the presented research, so the technique will be developed in detail as follows.
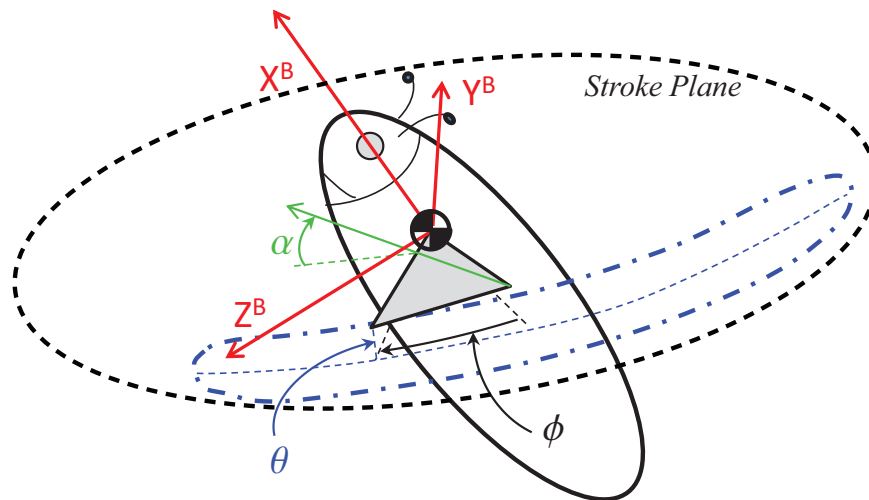
Figure 2.3: FWMAV coordinate frame definitions. [1]

Consider Figure 2.3, which defines the FWMAV wing kinematics and body-fixed coordinate frame. Three angles define the position of the wing at any point in a

stroke cycle: ϕ, stroke angle, θ, elevation angle, and α, angle of attack. For the BABM controller, the elevation angle is fixed and the angle of attack is controlled by an angle limited passive rotation joint, that is assumed to be constant during the up and down half-stroke cycles. This assumption is an approximation to the true motion which has been measured experimentally, as shown in [11], and modeled in [9], however keeping this assumption of constant α prevents predictions and data analysis from becoming intractable. In addition, the cycle-averaged forces are the main concern, as opposed to the inter-cycle forces. Therefore, for BABM control only the stroke angle of each wing is modified. The stroke angle function is controlled through three control parameters; amplitude, split-cycle parameter, and bias that directly influence the motion of the FWMAV, thereby allowing for full control of the vehicle. The split-cycle parameter creates a wing trajectory where the upstroke and downstroke are asymmetric, shifted approximately by $\pm\tau$, as shown in Figure 2.4. This asymmetric waveform creates a non-zero net drag force over the cycle of the flapping wing, while only marginally decreasing lift, and is used in the control of the FWMAV [9, 67]. It is desirable to maximize this net drag force per value of τ for a given FWMAV. The term $\partial T/\partial \tau$ will be used to represent the amount of net drag force or thrust, produced per τ used. For simplicity, Eq. (2.15) shows the split-cycle stroke angle function without the amplitude or bias parameters,

$$\phi\left(t\right) = \begin{cases} \cos\left[\omega\left(1-\Delta\right)t\right] & \text{for} \quad 0 \leq t \leq \frac{\pi}{\omega(1-\Delta)} \\ \cos\left[\omega\left(1+\Sigma\right)t+\xi\right] & \text{for} \quad \frac{\pi}{\omega(1-\Delta)} < t \leq \frac{2\pi}{\omega} \end{cases} \tag{2.15}$$

where, $\Sigma = \frac{\Delta}{1-2\Delta}$, $\xi = \frac{-2\pi\Delta}{1-2\Delta}$, and $\Delta = \frac{2\tau}{1+2\tau}$ thereby making the split-cycle stroke angle function in terms of τ, split-cycle parameter, and ω, flapping frequency.

In practice, it was found that the FWMAV wings did not adequately track the split-cycle waveform while flapping at the mechanism's first resonant frequency, but a truncated Fourier sum approximation of Eq. (2.15) of the trajectory could be tracked by using a discrete harmonic plant compensation (DHPC) technique. Using DHPC,

23
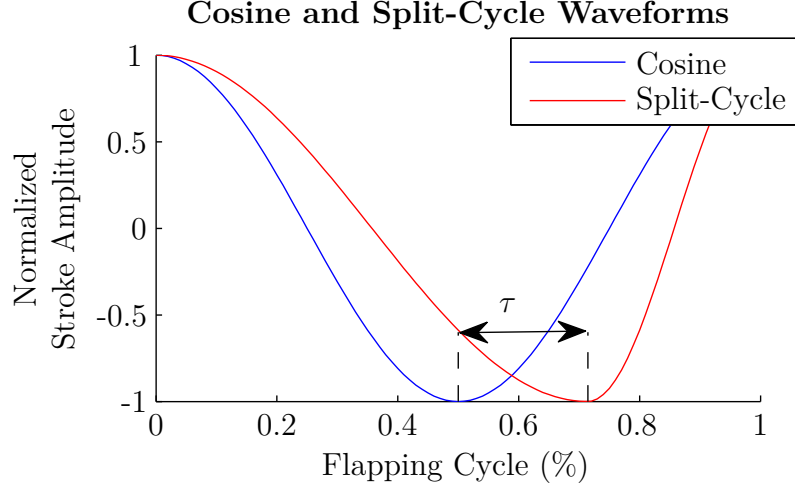
Figure 2.4: Idealized split-cycle wing trajectory.

the stroke angle function Eq. (2.15) can be approximated by the following stroke angle function in Eq. (2.16). The addition of an amplitude and bias term completes the BABM stroke angle function. The control parameters in the stroke angle function can then be applied symmetrically to both wings or asymmetrically as needed in order to obtain the desired control response. Using this method of control, it has been shown that five of the DOF can be controlled, thus allowing sufficient control over the vehicle for flight [1]. As implemented, the DHPC-BABM control is given as:

$$\phi(t) = A\{M_1(\tau)\cos[\omega t + \beta(\tau)] - M_2(\tau)\sin[2\omega t + 2\beta(\tau)]\} + \eta \qquad (2.16)$$

where ω is the flapping frequency and the three control parameters are: A, stroke amplitude, τ, split-cycle parameter, and η, stroke bias and M_1, M_2, and, β are harmonic coefficients and phase shifts that are functions of τ defined as:

$$M_1(\tau) = \frac{\cos(2\tau)}{M_{\omega_n}} \qquad (2.17)$$

$$M_2(\tau) = \frac{0.34\sin(3.3\tau)}{M_{2\omega_n}} \qquad (2.18)$$

$$\beta(\tau) = -2\tau - \phi_{\omega_n} \qquad (2.19)$$

24

where M_{ω_n} is the magnitude of the wing displacement at the first system resonance as measured by a frequency response function (FRF), $M_{2\omega_n}$ is the magnitude of the wing displacement at twice the first system resonance, and ϕ_{ω_n} is the phase of the wing displacement at the first system resonance. The FRF was found by measuring the actuator tip displacement as the output while a low amplitude swept sine wave drive signal was used as the input. The FRF of the flapper was then modeled using an eigensystem realization algorithm (ERA) as a four state, discrete state-space model to extract parameters of M_{ω_n}, $M_{2\omega_n}$, and ϕ_{ω_n} [69, 70].

2.5 Summary

This concludes the summary of the background research on flapping wing aerodynamics, design and construction of bio-inspired FWMAVs, and stability and control of FWMAVs. It also detailed the BABM control scheme approach. The review showed that the DHPC-BABM control scheme had matured in development to the point that experiments that close the loop on the FWMAV position and orientation were ready to be accomplished but had not yet been attempted. Also, measured forces and moments using the DHPC-BABM approach with hardware prototypes were considered relatively small but, the biomimetic *M. Sexta* wing prototypes were proving to generate significant forces. By leveraging these two previous AFIT research results(DHPC-BABM and the biomimetic *M. Sexta* wing) it was expected that the forces and moments generated by prototypes would be sufficient to close the loop on the FWMAV position and orientation using the DHPC-BABM approach. Figure 2.5 shows the progression of AFIT FWMAV research in four primary fields: biomimetic structures, FWMAV aerodynamics, FWMAV manufacturing, and FWMAV control. Previous work is at the top of the figure, with latest work at the bottom of the figure. The work presented here uses the results of Major Anderson's open-loop wing control and Major O'Hara's biomimetic wing and combines them to perform constrained closed-loop control demonstrations using the latest manufacturing techniques available.
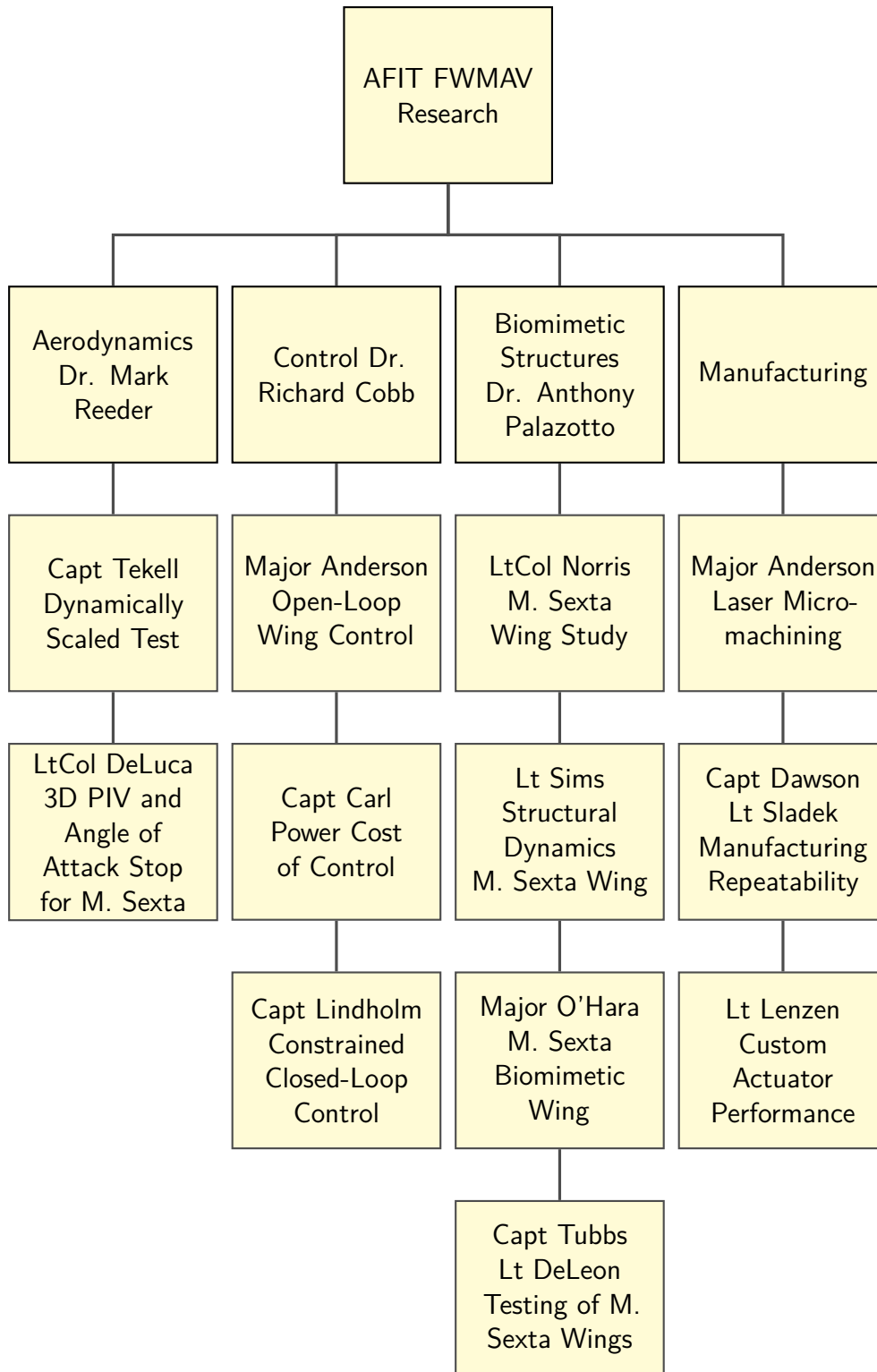
Figure 2.5: AFIT FWMAV research overview, faculty advisers are shown in the top level, projects are listed chronologically flowing down the chart.

The next chapter will detail the three different types of prototypes used to perform experiments. Also, the two different hardware experiment setups, the open-loop static setup and the closed-loop dynamic setup, used to collect the data that is presented later in Chapters IV, V and VII.

III. Experiment Methodology

This chapter will present the three different hardware prototype configurations used in this research. These hardware prototypes were used in two distinctly different experimental setups used in this research. The first was a static open-loop driven setup used to measure FRFs and collect aerodynamic force and moment data. The second is a dynamic closed-loop setup used in the demonstration of closed-loop control utilizing the DHPC-BABM control scheme.

3.1 Tested Hardware and Test Objectives

In this research three different hardware prototype configurations were used. Two of the three configurations were from previous work [29, 33]. The first was a single-wing flapper using a biomimetic *M. sexta* wing. This single-wing flapper was used in static open-loop testing. These static tests were done in order to measure the electrical power consumption of the single-wing flapper as frequency and control parameters were varied. Then, static tests were performed in an effort to optimize two components of the single-wing flapper.

The second configuration was a scaled FWMAV, smaller than the single-wing flapper, and it was used by a previous student in static experiments as well as open-loop dynamic experiments [1, 29, 67]. This small FWMAV was used in the initial dynamic closed-loop demonstrations. This small FWMAV had limitations of smaller forces and moments and also a limited supply of the appropriate sized actuators. This led to a blending of these two configurations into the last configuration.

The last configuration was a dual-wing biomimetic FWMAV that utilized the *M. sexta* wings. This configuration was used in the final closed-loop control demonstrations. Figure 3.1 show the three configurations, with the single-wing flapper at the top left, the small FWMAV at the top right, and the *M. sexta* based FWMAV shown at the bottom.
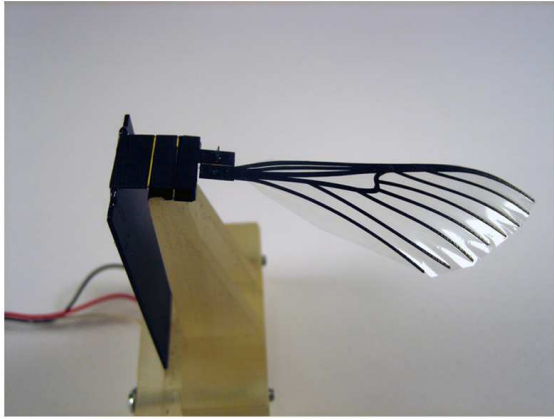
Single-Wing Flapper
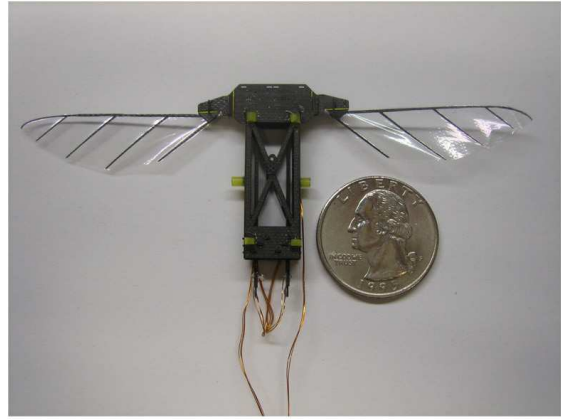
Small FWMAV
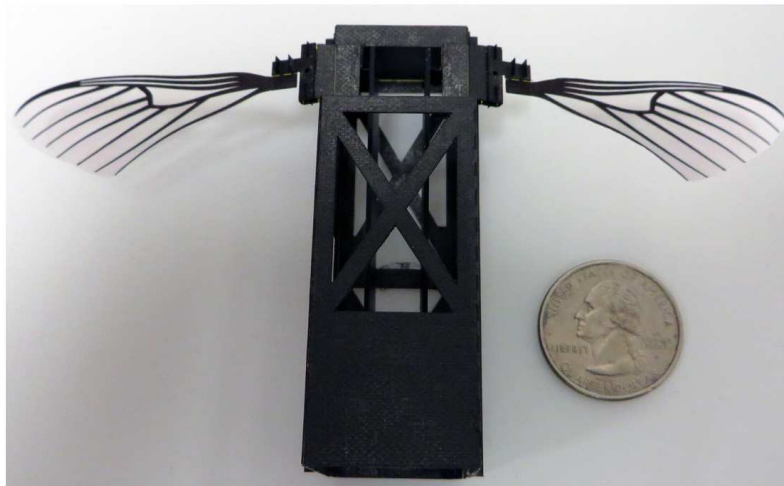
Biomimetic FWMAV

Figure 3.1: The three prototype configurations used in this research. Top left, single-wing flapper. Top right, small FWMAV. Bottom biomimetic *M. sexta* based FWMAV.

Sample of Piezo Drive Voltage and Current Measurements
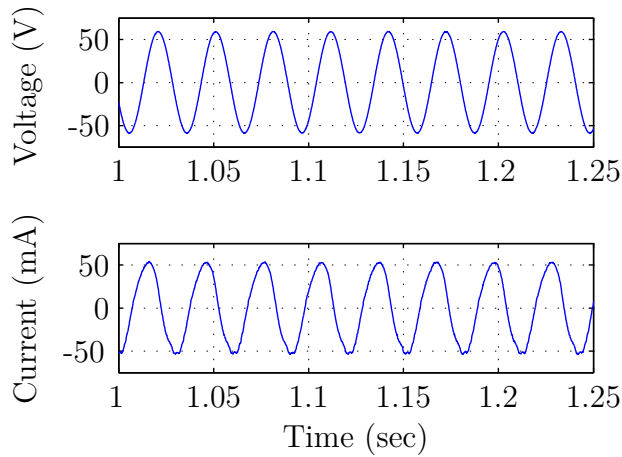
Figure 3.2: Sample measurements of the drive voltage and current for the bimorph-piezoelectric actuator measured at the drive amplifier.

3.2 Open-loop Testing Setup

A MATLAB script was used to generate the voltage profile which was then sent to the power amplifier through a National Instrument's USB-6229 BNC ADC/DAC box, which has a ±10 volt output range. Using this script, the flapper can be driven at any desired flapping frequency. A Trek PZD700 amplifier was used to amplify the drive signal x30 to drive the bimorph-piezoelectric actuator. The current was measured directly off the Trek amplifier and used with the voltage signal to calculate the power using Eq. (3.1), where V_{RMS} was the measured root mean square (RMS) voltage, I_{RMS} was the measured RMS current, and γ was the measured phase angle difference between the voltage and current. The phase angle, γ, between current and voltage was found by taking the fast Fourier transform (FFT) of both the voltage and current measurements windowed over a single flapping cycle and compared to find the phase of the voltage and current at the fundamental frequency, in this case the flapping frequency. This was repeated for the duration of each test and the mean of the power signal was recorded as the cycle-average power. Figure 3.2 shows a sample of drive voltage and current measurements taken off the amplifier for the piezoelectric actuator.

Figure 3.3 shows a diagram of the experiment setup. Cycle-averaged lift was measured using an ATI Industrial Automation Nano 17 Titanium 6 axis force balance, which has a force resolution of 1.4 mN resolution and up to a 14.1 N range. Previous work done by Sladek in [71] showed the Nano 17 to have a resolution of 0.2 mN even though the reported resolution was 2.8 mN. This provides confidence in the capability of the Nano 17 Titanium to accurately record the data in the range and resolutions reported later. The actuator tip displacement was measured using a MICRO-EPSILON optoNCDT 1800-20 laser displacement sensor, which has a 20 mm measuring range and 2 μm resolution for frequencies up to 5 kHz. Power efficiency, η_{PE}, is defined using the cycle-averaged power, $\overline{P}$, and cycle-averaged lift, $\overline{L}$, shown in Eq. (3.2).

$$P = V_{RMS}\, I_{RMS} \cos\gamma \tag{3.1}$$

$$\eta_{PE} = \frac{\overline{L}}{\overline{P}} \tag{3.2}$$

For each prototype under test, an FRF was found for the flapping mechanism by using a low amplitude swept sine signal as the input, and a laser displacement sensor focused on the tip of the actuator as the output. The FRF measures key values used in the controller in Eqs. (2.17) to (2.19), specifically M_{ω_n}, $M_{2\omega_n}$, and ϕ_{ω_n}, as well as the resonant frequencies of the first and second modes of the flapping mechanism.

With the controller parameters measured, data points were collected for a given experiment. Each test consisted of 100 cycles of flapping. Measurements were taken in the middle of the test period while the prototype was in a steady-state flapping motion. Each test was repeated 5 times to get mean and standard deviation data for the given design.

31
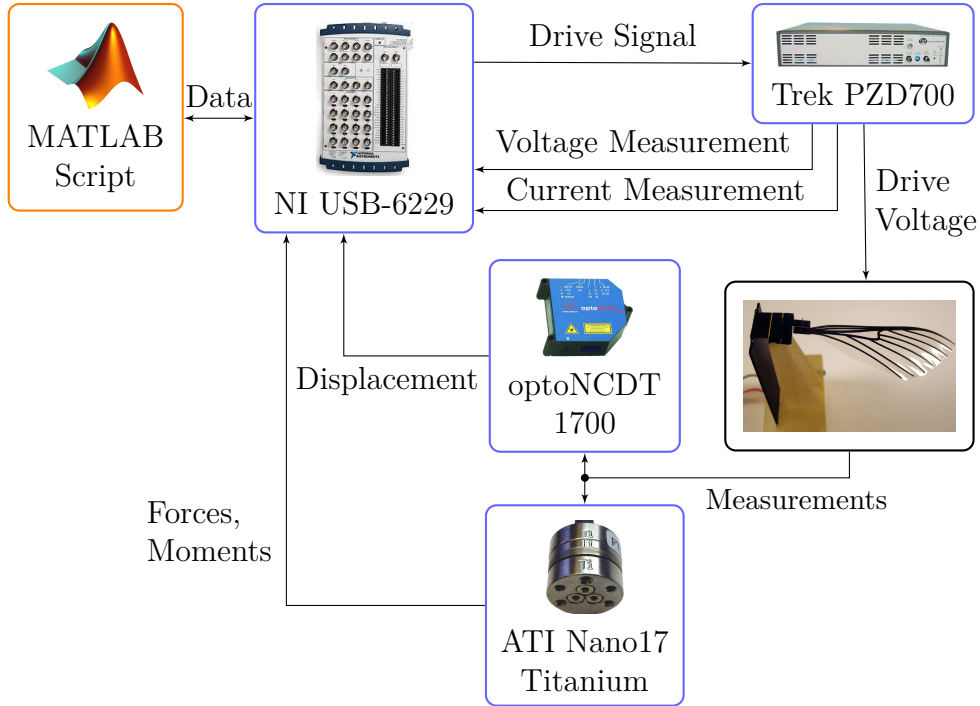
Figure 3.3: Diagram of equipment setup used for open-loop experiments.

3.3   Closed-loop Flapping Wing Micro Air Vehicle Setup

The goal of the closed-loop testing was to demonstrate control in a variety of constrained configurations. For each closed-loop constrained configuration, a DHPC-BABM based feedback controller was implemented in dSPACE, a hardware microcontroller target for Simulink based controllers, providing real-time analog and digital interfaces with the experimental hardware. Since these experiments are considered a buildup to free-flight with the desire to only demonstrate control on constrained DOF, models were not developed for controller design. Instead, proportional-integral (PI) and Proportional-integral-derivative (PID) controllers were used due to their simplicity. Simple controllers were desired due to future free-flight FWMAVs having a very limited power and weight budget. Demonstrating control utilizing basic controllers allows for potential savings in microcontroller power and weight requirements. The feedback controllers were used to vary the BABM control parameters in order to command the FWMAV to a desired setpoint. Starting with gains of zero, the proportional gain was increased in real-time until the control input overcame friction of the system.

This effectively found the lowest value for the gains. Further tuning was done by iteration until the desired performance was achieved. Gains were adjusted using the dSPACE software front end, Control Desk, which allows for adjustments in real time or in between tests.

FWMAV position information was measured using a Simulink Computer Vision based webcam tracker. The custom tracker is discussed in Chapter VI and is used to find the position and pose of the FWMAV which is used in the feedback loop. The tracker was accurate to within 2 mm of the FWMAV's position for the setup used in these tests. Once the tracker finds the position and pose of the FWMAV, it compares it to setpoints and then feeds back the errors to the PI/PID controllers within dSPACE through the National Instruments USB-6229 BNC ADC/DAC box. The overall closed-loop experiment setup is shown in Figure 3.4.
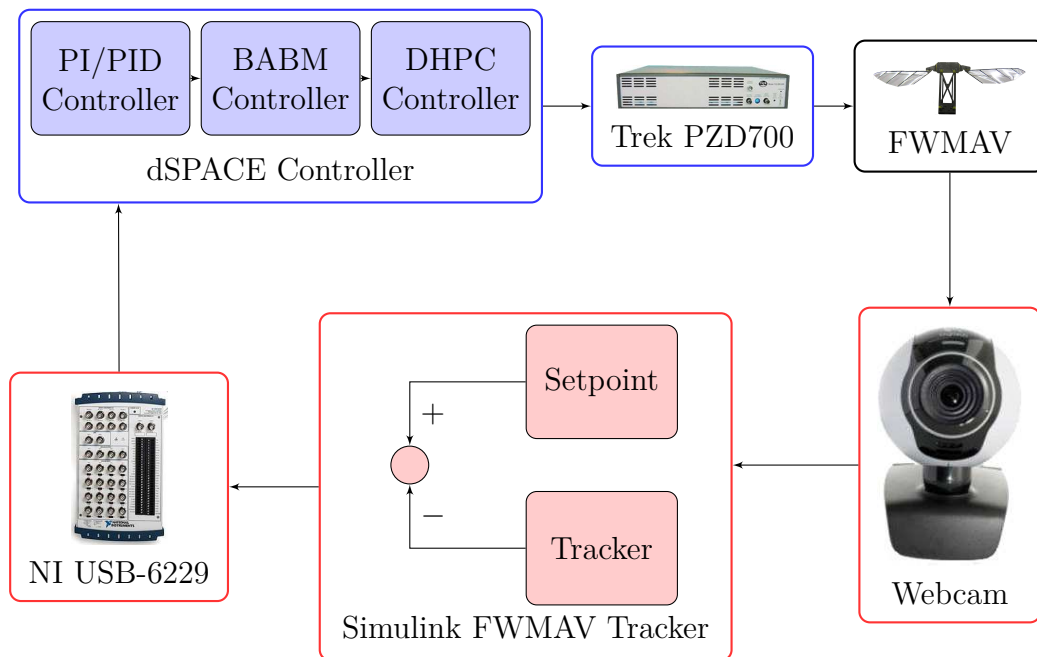
Figure 3.4: Diagram of equipment setup used for closed-loop experiments.

3.4 Summary

This concludes the two different experiment testing setups, one for open-loop static experiments, and one for closed-loop dynamic experiments. Each setup was

used in a variety of different experiments with different prototype hardware as will be shown in Chapters IV, V and VII. The diverse experiments and hardware used demonstrated the flexibility and robust nature of these setups. In the next chapter, the electrical power requirements of operating at different frequencies, or with different BABM control parameters, will be examined.

IV. Electrical Power Measurements of Piezoelectric Actuated Flapping Wing Micro Air Vehicle

This chapter describes experiments performed utilizing a single-actuator, single-wing flapper mechanism, rather than a multi-actuator and wing FWMAV. The single-wing flapper is dynamically identical to the full dual-wing FWMAV, but does not include the complexity required for lightweight flight models. This chapter presents the results of the electrical power requirement studies accomplished for a piezoelectric driven FWMAV. First, the power efficiency as the flapping frequency varies will be presented followed by the power requirements as the BABM control parameters are varied.

4.1 Performance at Variable Frequencies

A single-wing test flapper, as seen in Figure 4.1, was used during this phase of the experiment. It consists of the following components: wing, passive rotation joint, angle of attack stops, 4-bar linkage, piezoelectric actuator, carbon fiber frame, and rapid prototype base. The wing has a 50 mm span and was designed to mimic the structural dynamics of a *M. sexta* , as reported in [33, 34]. The 4-bar linkage is designed to amplify the 1.5 mm input from the actuator to create a $\pm 55°$ stroke angle to match the *M. Sexta*. The bimorph piezoelectric actuator used was an Omega Piezo Technologies Inc. OPT 60/20/0.6. The actuator can be driven at variable amplitude, waveform shapes, and flapping frequencies. The carbon fiber frame and rapid prototype base provide stiff boundary conditions for the actuator and linkage, and also provide a mounting point to a force balance. The experiment was setup as described in section 3.2.

Power and lift were measured as flapping frequency was varied from 10 Hz to 120 Hz, with the voltage the same for each test point. Each test point consisted of 100 cycles of flapping. Measurements were recorded from the middle 80 cycles of the test, while the flapper was in a steady-state flapping motion, and averaged to calculate the cycle-averaged values. Each test was repeated 5 times to calculate the mean and standard deviation of the cycle-averaged data for a given flapping frequency. These
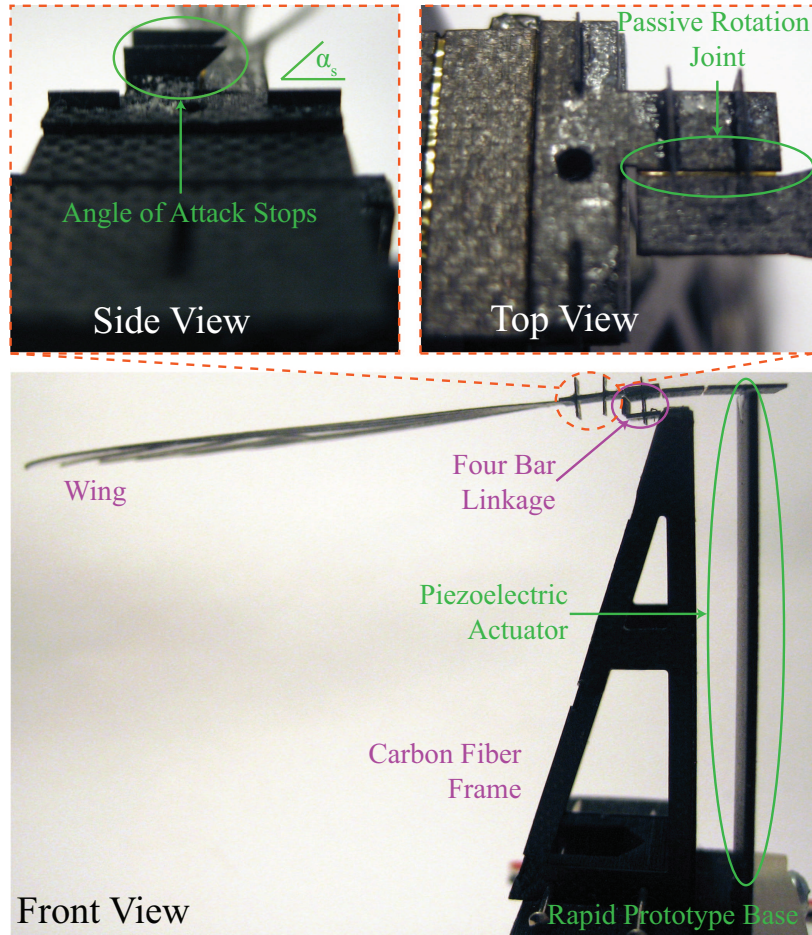
Figure 4.1: Side, top, and front view of single-wing flapper used in this study with individual components labeled.

results were used to find which flapping frequency would be most power efficient, as defined in Eq. (3.2) with respect to lift.

Cycle-averaged power and cycle-averaged lift were measured as flapping frequency was varied. This was done to find the most power efficient system flapping frequency with respect to the lift generated. System refers to the interconnected components of the FWMAV: actuator, linkage, passive rotation joint, and wing, as each component has a different frequency response and resonance when tested separately. Figure 4.2 shows the power efficiency as the flapping frequency was changed. At frequencies from 0 Hz up to 32 Hz, the power efficiency was small and increased as frequency increased. Then, as frequency increased further, power efficiency reached

a maximum in the range of 32-36 Hz. The power efficiency then falls drastically until it reaches near zero values, where no appreciable lift was measured, due to the maximum stroke angle decreasing as the flapping frequency was increased. The error bars represent the standard deviation of the cycle-averaged data for each test point. Larger spacing of tested frequencies was used at 55 Hz and 70 Hz to avoid higher-order system or component resonances that have potential damaging effects on the flapping mechanism. Figure 4.3 shows the lift and power data that made up the power efficiency data. This provides a sense of the magnitude of the quantities involved as well as gives a sense of the trends in the two different data sets. Again, the error bars represent the standard deviation of the cycle-averaged data for each test point.
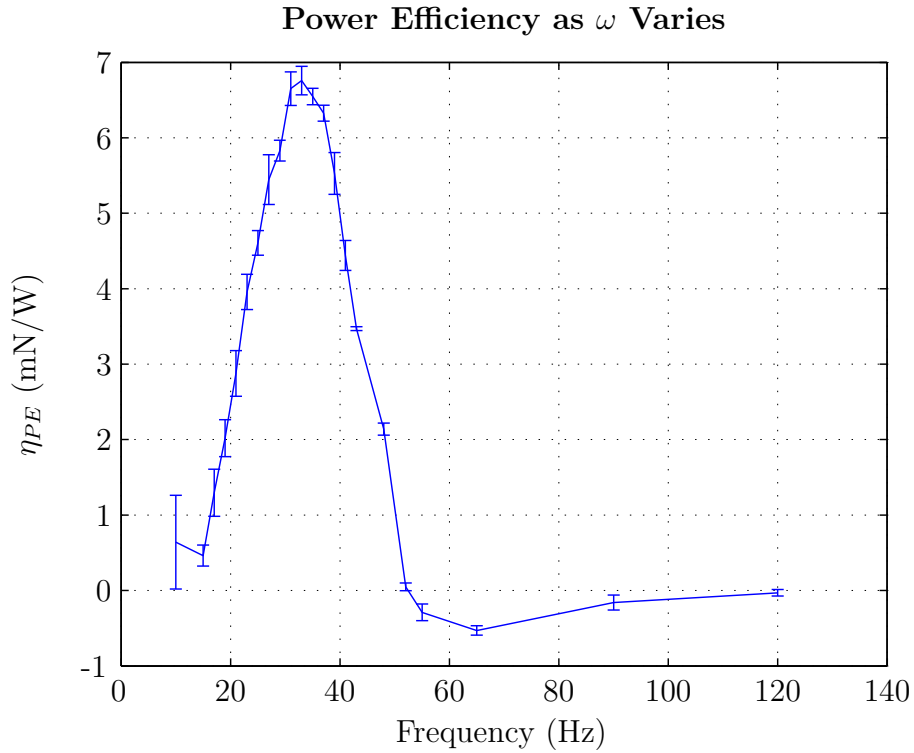
Figure 4.2: Power efficiency as flapping frequency is varied, error bars represent one σ of the cycle-averaged data.

Figure 4.4 shows the displacement as measured at the actuator tip for a complete flapping mechanism as the frequency was varied. The points represent measured data points and the trace represents a model fit to the data. The flapping mechanism's

37
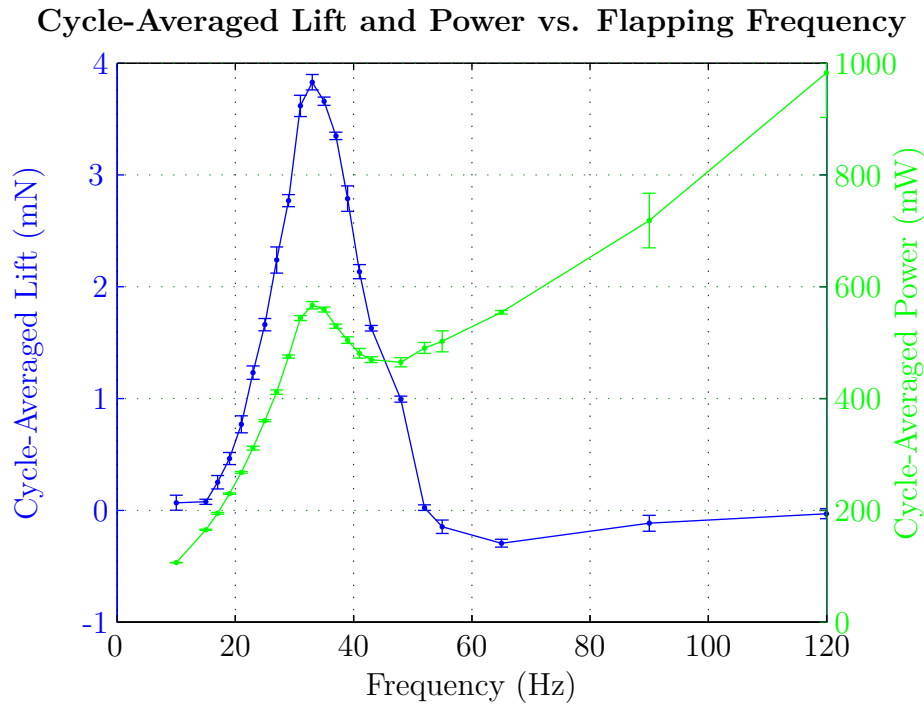
Figure 4.3: Cycle-averaged lift and power versus flapping frequency, error bars represent one σ of the cycle-averaged data.

measured system resonance was 32.5 Hz. It can be seen in Figure 4.2 that in the region at and near resonant frequency, the power efficiency was maximized. This result shows that flapping at the system's resonant frequency was most efficient from a lift to power perspective. It is also seen that the frequency response function shown in Figure 4.4 has a shallower peak than the data shown in Figure 4.2. This is as expected as the piezo tip displacement is proportional to the the flapping stroke amplitude, Figure 4.4, whereas lift is proportional to the wing velocity squared, and higher stroke amplitudes create greater wing velocity. Also note that the frequency response function displacement is shown in dB so the peak at resonance is actually double the displacement below and above resonance for a given input.

Clearly, it was shown that for a piezoelectric actuated FWMAV, it is most power efficient to flap at the system's resonant frequency, and that future testing of this class of FWMAV should focus primarily on schemes based around resonant flapping. The
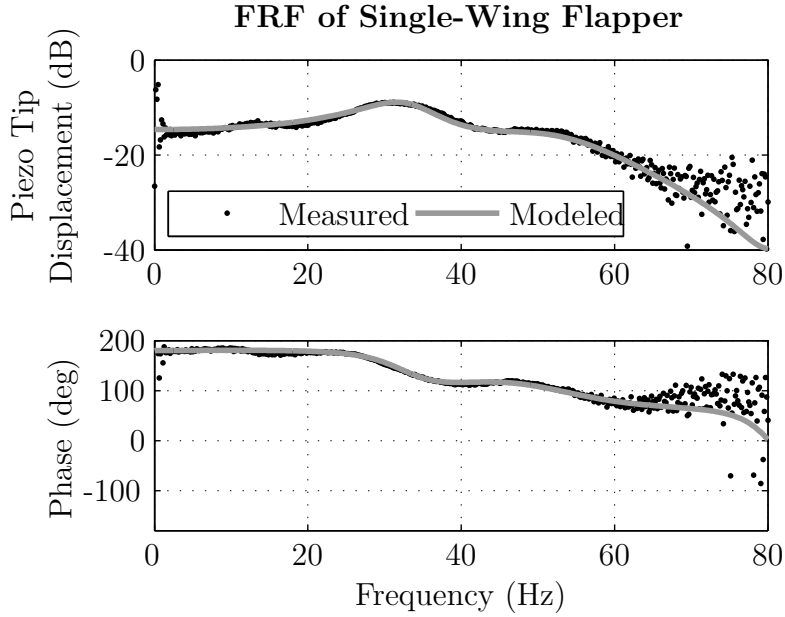
Figure 4.4: Frequency response function of single-wing flapper, system resonance is at 32.5 Hz.

flapping frequency, ω in Eq. (2.16), for other tests in this work was therefore fixed at the system resonance frequency, while the control parameters, A or τ, were varied.

4.2 Performance of Bi-harmonic Amplitude and Bias Modulation Parameters

Each test consisted of a half second of flapping. Measurements were taken near the end of the test while the flapper was in a steady-state flapping motion. Each test was repeated 20 times to get a mean and standard deviation for the given test parameters. The experiment was setup as described in section 3.2. The baseline used was 80% amplitude with zero bias and zero split-cycle parameter to represent a steady-state hovering flight condition, where 100% amplitude would correspond to the voltage required for maximum wing deflection. Then the following tests were performed off-nominal: -10% to +20% amplitude (A) in 5% increments, nominal amplitude with -0.2 to 0.2 split-cycle parameter (τ) in 0.05 increments, and finally nominal amplitude with -0.2 to 0.2 bias (η) in 0.05 increments. All testing was done

at resonant frequency as it was shown in section 4.1 that a FWMAV operating at resonant frequency will maximize aerodynamic and mechanical efficiency.

The collected data was then used to create a cycle-averaged power required model based on a function of the DHPC-BABM control parameters. This model can be used to predict power requirements for untethered flight, and also be used to develop a minimum power optimal controller for the FWMAV using the DHPC-BABM control method.

A total of 460 test samples were collected in characterizing the power required using DHPC-BABM control. Figure 4.5a shows how the power required changes as the amplitude is varied off the nominal value. The error bars represent the standard deviation of the measured cycle-averaged power at a given point. It can be seen that the cycle-averaged power required is proportional to the amplitude parameter.
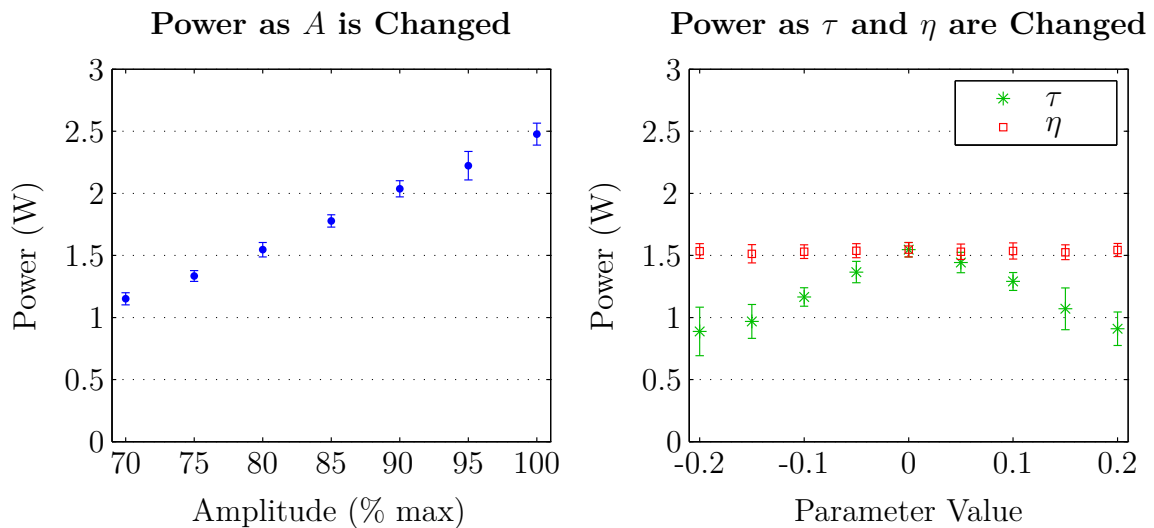
Figure 4.5: Cycle-averaged power versus A, τ, and η. Error bars represent one standard deviation.

Figure 4.5b shows how the cycle-averaged power required changed as the split-cycle or bias parameters were changed as the amplitude was held at a constant 80%. It can be seen that as the absolute value of τ is changed, the cycle-averaged power required is reduced. This may seem counter intuitive, but looking at the voltage, current, and displacement time histories in Figure 4.6, shows that RMS values for

voltage and current are lower than they would be for a pure sinusoidal waveform. The sinusoidal input is changed according to τ with a pure sine wave generated for a value of zero and increasingly less sinusoidally as the absolute value of τ is increased.
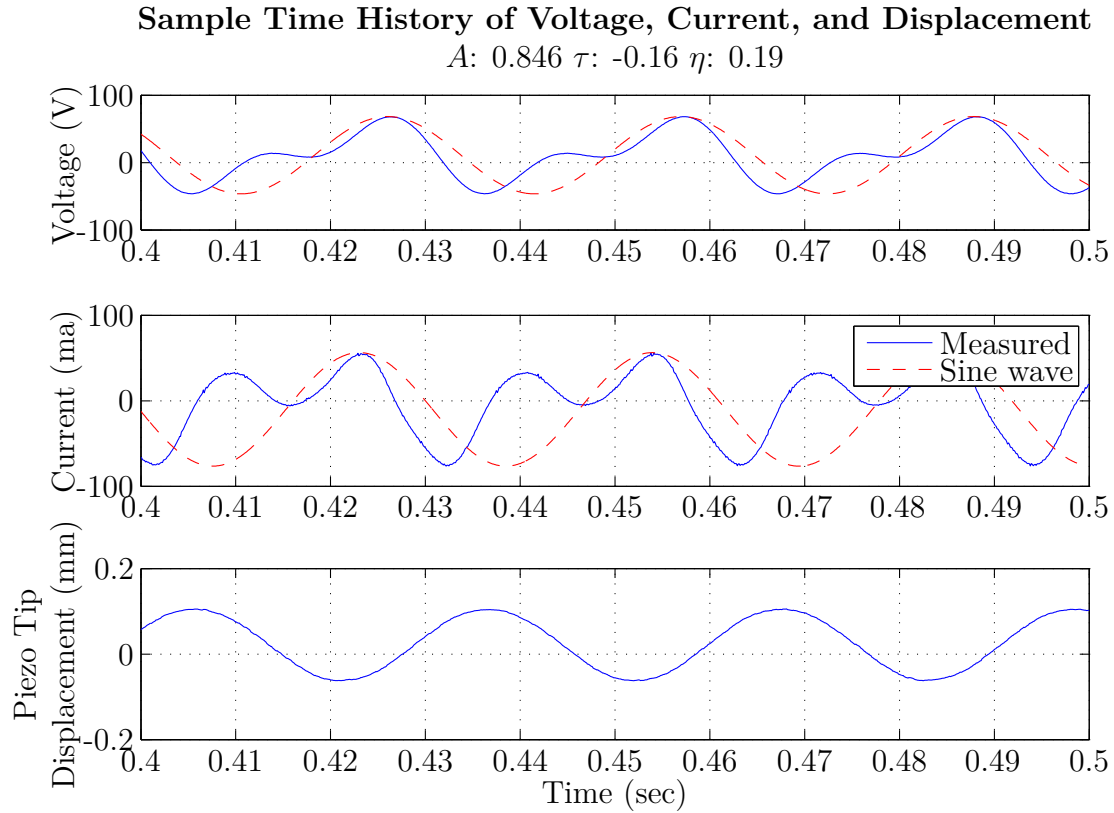
Figure 4.6: Example time history of voltage, current, and displacement for given test parameters.

Only A of Eq. (2.16) was held constant for these tests, not the value of lift, as a force balance was not available at the time of these tests. So in order to stay at a given altitude it is likely an increase in the parameter A will be needed when using increasingly larger values of τ. Future work will examine how these values trade off for a given amount of lift. It can also be seen that no meaningful change occurs in cycle-averaged power required as η is changed. This is as expected since the RMS values of voltage and current are not changed in steady-state. Finally, the standard deviation tends to be greater when measuring smaller values of cycle-averaged power. This is

expected as the values of current being measured are small and as they decrease it begins to approach the noise floor.

A least squares regression through the data in Figure 4.5 was done to find the coefficients for a cycle-averaged power required model shown in Eq. (4.1). The power is in units of watts.

$$P(A, \tau) = P_o + P_A A + P_\tau |\tau| \tag{4.1}$$

P is the total cycle-averaged power required, P_o is a bias term, P_A is the change of power required as amplitude is varied, and P_τ is the change of power required as the absolute value of the split-cycle parameter is varied. The values found for this test article are shown in Table 4.1.

Table 4.1: Value of power required model parameters for single-wing flapper.

Parameter	Value (W)
P_A	0.0046
P_τ	-0.0033
P_o	-0.0021

In order to test the model an additional ten test points were chosen varying all the parameters as shown in Table 4.2. Points were generated randomly in the range tested, and checked to make sure each test point would not exceed the voltage limits of the piezoelectric actuator, but still have reasonable flapping motion. The same method to collect data by running the test 20 times with the same parameters to get a mean and standard deviation was used. The collected data was then compared to the predictions made in Figure 4.7. As can be seen, the model does a fair job of predicting the power required for these various test cases. This shows that cycle-averaged power required can be modeled using this technique for a future flight weight FWMAV and fed into a cost function of an optimal minimum power DHPC-BABM based controller.

4.3 Summary

In this section it was shown that for a piezo-driven FWMAV, flapping at the system's first resonance is the most efficient in terms of lift per power. Also, power use for varying BABM control parameters was shown with the result that amplitude directly correlates to power requirements, whereas the split-cycle parameter lowers the power requirements, and bias has little impact on power requirements. This power use was modeled and is repeatable. The results can be used to influence future control laws with the goal to minimize the power consumed. In the next chapter the single-wing flapper used in this chapter will go through a design process with the goal of optimizing two components of the passive rotation joint for maximum lift and thrust generation.

Table 4.2: Model Testing Points.

Test	Amplitude (%)	Split-Cycle Parameter	Bias
1	81.9	0.06	-0.05
2	94.5	0.03	-0.05
3	97.5	0.01	-0.17
4	80.8	0.14	0.05
5	93.2	0.04	-0.01
6	86.3	-0.14	0.07
7	93.8	-0.05	0.02
8	84.6	-0.16	0.19
9	99.5	-0.10	-0.09
10	91.0	0.18	-0.01
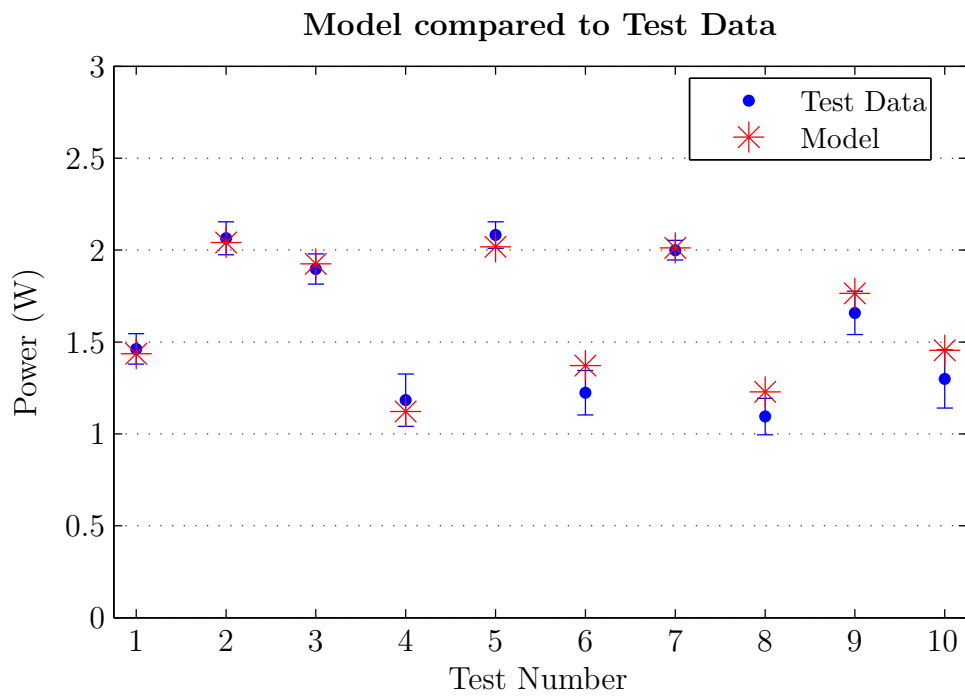
Figure 4.7: Model data compared to test data. Error bars represent one standard deviation.

V. Passive Rotation Joint Design

In this chapter the single-wing flapper was used again in two distinctly different test suites with the goal of optimizing the passive rotation joint of the single-wing flapper. The first suite of tests varied one component of the flapper, α_s, while leaving all the other design variables fixed. The second suite of tests were performed with a fixed α_s while varying the κ_h parameter. Finally the optimal design from both will be combined as a final design.

5.1 Passive Rotation Joint Design Elements

The single-wing flapper is shown in Figure 4.1. It consists of the following components: wing, passive rotation joint, angle of attack stops, 4-bar linkage, piezoelectric actuator, carbon fiber frame, and rapid prototype base. The wing was designed to mimic the structural dynamics of a *M. sexta*, as reported in [33, 34]. The 4-bar linkage is designed to create a $\pm 55°$ stroke angle to match the *M. sexta*. The bimorph piezoelectric actuator used was an Omega Piezo Technologies Inc. OPT 60/20/0.6 and provides an input deflection to the linkage and thus drives the wing. The actuator can be driven at variable amplitude, waveform shapes, and flapping frequencies. The carbon fiber frame and rapid prototype base provide stiff boundary conditions for the actuator and linkage, and also provide a mounting point for attachment to a force balance. In this study α_s and κ_h will be varied in order to capture their effect on lift and thrust force production.

5.1.1 Angle of Attack Stops.   The angle of attack stops were initially set at $45°$ using the same design used in previous studies [33]. Placement of the angle of attack stops on the single-wing flapper can be seen in Figure 4.1. Additional angle of attack stops were designed as seen in Figure 5.1. Angle of attack stops of $30°$, $40°$, $45°$, $50°$, and $60°$ were designed, produced, and tested. The angle of attack stops are required to prevent the wing from over rotation during flapping, but do not guarantee that this angle is held constant during each stroke half-cycle.
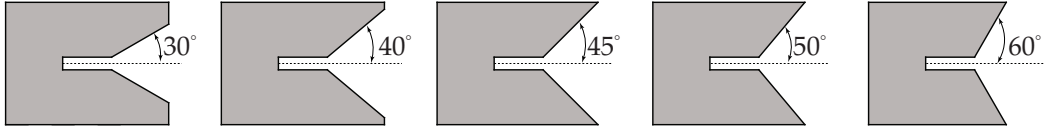
Figure 5.1: Side view of angle of attack stops.

5.1.2 Passive Rotation Joint Stiffness. In addition to the angle of attack stops, the stiffness of the passive rotation joint was varied, and its impact on the first and second resonant frequencies or modes were measured. The first resonant mode of the single-wing flapper is the wing stroke angle. The second resonant mode is the rotation of the wing around the passive rotation joint. It is assumed that by changing the stiffness of the passive rotation joint the frequency of the second resonant mode can be changed as desired. The motivation for this study was due to the original passive rotation joint design consistently resulting in the second resonant mode at twice the first resonant mode. This is not desirable as twice the first resonant mode is used in the second harmonic term in the DHPC control signal to generate the split-cycle waveform using $M_{2\omega_n}$ from Eqs. (2.16) and (2.18). Therefore, when the second resonant mode was twice the first resonant mode, the passive rotation joint was being over-excited giving an undesirable rotation of the wing, thus preventing the angle of attack from remaining relatively constant during the half-stroke cycle as was previously assumed. This over-excitation of the wing rotation also does not give the desired performance when using the split-cycle parameter.
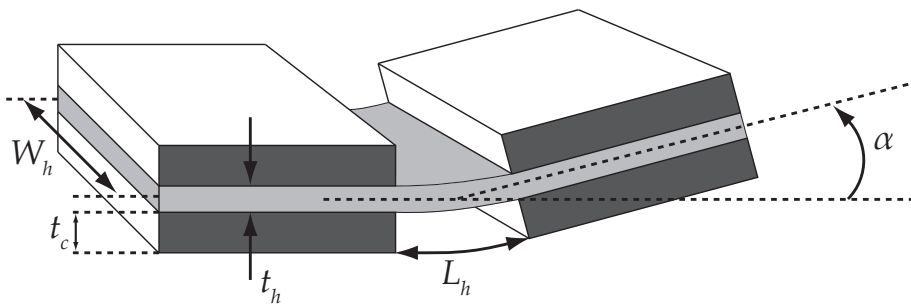
Figure 5.2: Geometry of the passive rotation joint design.

46

Lift and thrust production were also measured in order to see the passive rotation joint stiffness impact on force production. The hinge of the passive rotation joint can be changed either by adjusting the geometry, as seen in Figure 5.2, or by using different materials for the hinge. The passive rotation joint's rotational stiffness can be modeled as a linear elastic beam deforming under an external moment:

$$\kappa_h = \frac{E_h t_h^3 W_h}{12 L_h} \tag{5.1}$$

where, t_h, W_h, and L_h are the thickness, width, and length of the hinge layer, t_c, is the thickness of the carbon layer above or below the flexure layer, and E_h is the modulus of the hinge material [9]. Additionally, the predicted max deflection of the rotation joint can be computed:

$$\alpha_{mp} = \frac{\pi}{2} - \frac{L_h}{t_c} \tag{5.2}$$

where α_{mp} was the predicted maximum rotation angle. The angle of attack stops are used to prevent the rotation of the wing from exceeding the maximum rotation angle. In this study the material, the material thickness, and the width of the rotation joint are left fixed, and the length of the hinge was varied. The hinge material used was 25 micron Kapton and the designed hinge width was 4.78 mm. Table 5.1 shows the tested hinge stiffness, designed hinge length, and predicted maximum rotation angle. Designed hinge length differs from the actual hinge length due to the additional material removed in the laser micromachining process used to manufacture the flapping mechanism. The differing length of the designed versus manufactured hinges also impacts the actual maximum rotation angle versus the predicted maximum rotation angle.

5.2   *Passive Rotation Joint Design Results*

The experiment was setup as described in section 3.2. Data points were collected for each given design, using the following signal parameters: flapping frequency equal to the first mode, amplitude fixed, and split-cycle parameter varied for each test point.

47

Table 5.1: Tested design hinge stiffness, length, and maximum rotation angles.

Design	κ_h Predicted (n-m/rad)	α_m Predicted (deg)	Hinge Length (mm)
Original	6.22E-5	95.5	0.2500
x1.25	7.78E-5	76.1	0.1992
x1.5	9.36E-5	63.1	0.1651
x2.0	1.24E-4	47.7	0.1250
x2.5	1.56E-4	38.2	0.1000
x3.0	1.87E-4	31.8	0.0833

Each test consisted of 100 cycles of flapping. Measurements were taken in the middle of the test period while the flapper was in a steady-state flapping motion. Each test was repeated 5 times to get mean and standard deviation data for the given design.

In this section the results of varying α_s and κ_h will be presented. To help identify outliers and recognize trends in the measured data, an additional data set generated from a blade-element model presented in [25], using the model's parameters for the flapper and each test condition, were added.

5.2.1 Angle of Attack Stops. In Figure 5.3, lift versus angle of attack stop is shown, with each test performed at a fixed amplitude of 0.5. It is seen that the experimental results were consistently underpredicted by the blade-element model. This is expected from previous results [25]; however, the trend in the data follows the model, with the exception of the data in the 50-60 degree range. Here, the blade-element model shows increasing lift with increasing angle of attack, while the experimental data shows no increase in lift. This is likely due to the wing beginning to stall for this range of angle of attack, which the equation for lift coefficient in the blade-element model did not predict. From this data, in order to maximize lift, flapping mechanisms using this wing should use an angle of attack stop in the 50-60 degree range.

Next, data was measured for each α_s design as the split-cycle parameters -0.05, -0.025, 0, 0.025, and 0.05 were tested, while amplitude was held fixed at 0.4. The cycle-

Maximum Cycle-Averaged Lift vs. Angle of Attack Stop
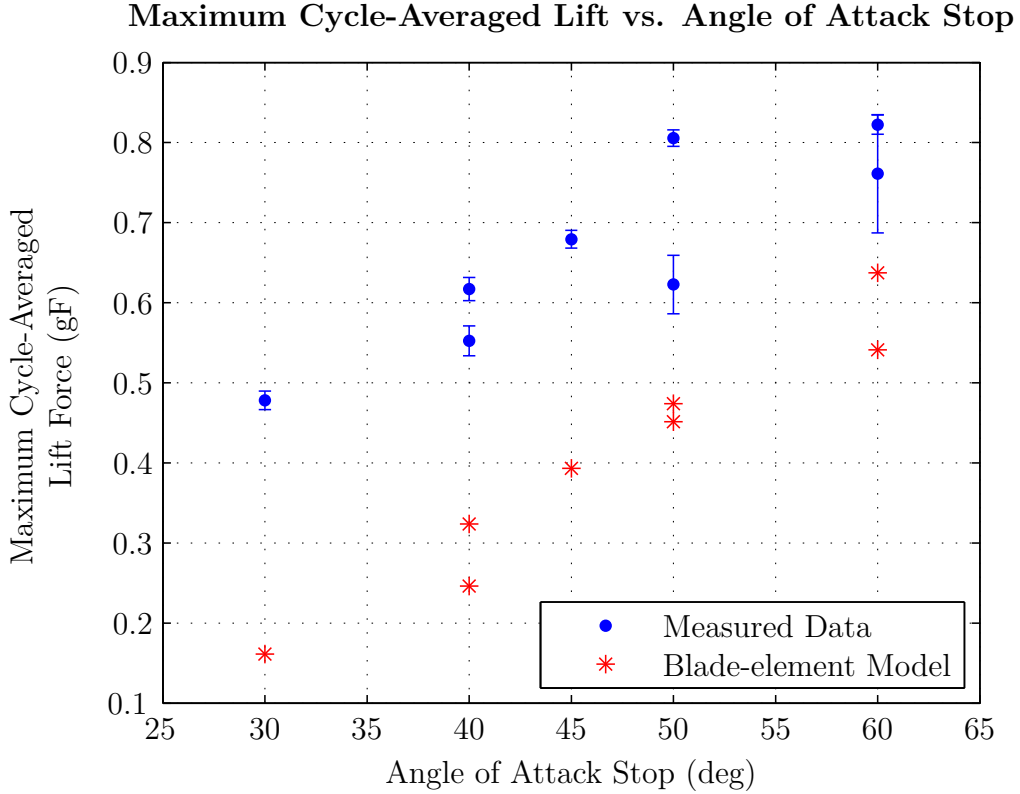
Figure 5.3: Lift versus angle of attack stop angle, repeat test points are for different test mechanisms operating at different flapping frequencies. Error bars represent one σ.

averaged thrust, T, was then plotted versus the split-cycle parameter, τ, for each α_s design. A linear fit was applied to each plot and the slope was recorded as $\partial T/\partial \tau$. The results for each α_s design are shown below in Figure 5.4. The data used in calculating $\partial T/\partial \tau$ can be found in Table D.1. A higher magnitude of $\partial T/\partial \tau$ is desirable as it represents more control authority while using the split-cycle waveform, and blade-element theory predicts the slope should be negative. As can be seen, with small α_s, there is a large magnitude but opposite sign of $\partial T/\partial \tau$ from what was expected based on blade-element theory. This is likely due to asymmetric inertial forces being larger than asymmetric aerodynamic forces when using the smaller amplitude angle of attack stops. Then, as the α_s is increased, $\partial T/\partial \tau$ returns to the expected negative values. Also it is seen that the magnitude increases as α_s increases.
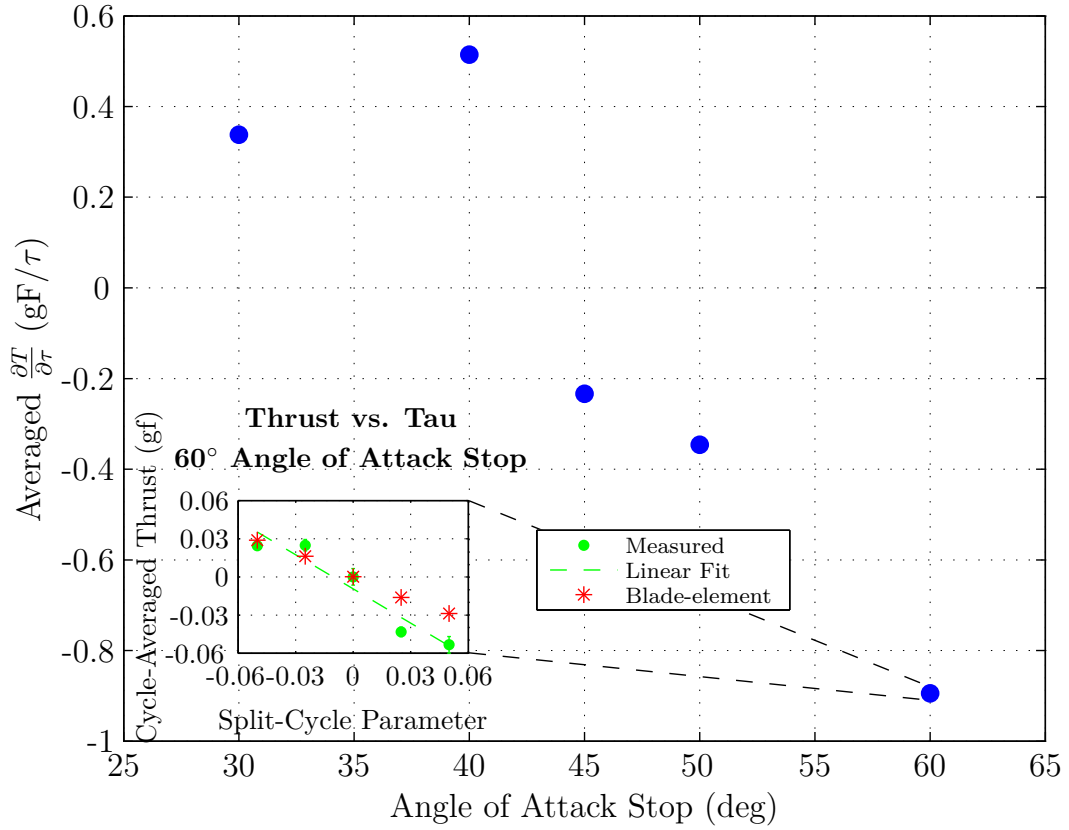
Figure 5.4: Main figure, thrust generation per split-cycle parameter as the angle of attack stops were varied. Inset figure, measured, linear fit, and blade-element data points used to calculate the thrust per split-cycle for 60 degree angle of attack stop.

Reviewing the previous lift and thrust results, the most desirable α_s design over the range tested appears to be 60 degrees, which agrees with results from [11]. This α_s demonstrated the maximum lift values, and also had the highest magnitude $\partial T/\partial \tau$ with the correct sign.

5.2.2 Passive Rotation Joint Stiffness. Multiple flappers for each design in Table 5.1 were built and the measured frequency response data were averaged to reduce the impact of manufacturing variation on the results. Figure 5.5 shows measured and modeled FRFs of two different κ_h designs. The dominant first and second resonant frequencies of each design can clearly be seen.

Frequency Response Function of Two Differently Designed Single-Wing Flappers
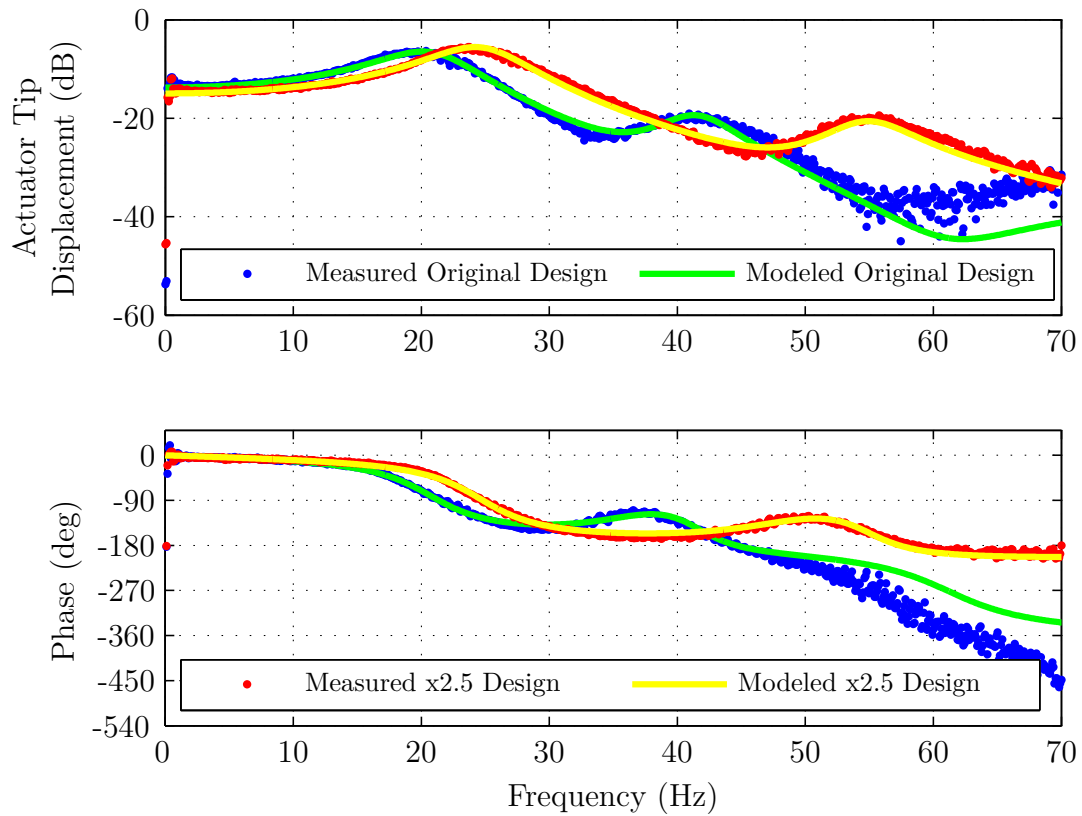
Figure 5.5: Example measured and modeled single-wing flapper frequency response function for the original and x2.5 passive rotation joint designs.

Table 5.2: Averaged first and second modal results due to changing passive rotation joint stiffness.

| Design | Mode 1 | | Mode 2 | | $\dfrac{\omega_{n2}}{\omega_{n1}}$ |
	ω_n (Hz)	ζ (%)	ω_n (Hz)	ζ (%)	
Original	21.12	18.35	41.55	7.35	1.97
x1.25	22.48	14.93	46.55	6.76	2.07
x1.5	22.78	15.49	46.73	8.25	2.05
x2	21.32	16.05	48.03	6.67	2.25
x2.5	25.29	15.10	56.56	6.92	2.24
x3	25.64	23.17	59.89	6.89	2.34

Table 5.2 shows the first and second resonant modal frequencies, damping ratios, and the ratio of the second resonant mode to the first resonant mode for each κ_h design. It can be seen that at and near the original stiffness, ω_{n2}/ω_{n1} is near 2. This behavior was previously explained to be detrimental for use with DHPC-BABM control scheme. As κ_h increases, an increase in this ratio is seen, which moves the second mode away from twice the first mode frequency. This demonstrates that κ_h is a useful tool in the FWMAV designer's toolbox for adjusting the ratio of these frequencies as desired.

It is also seen that in the x2.5 and x3 range that there is an increase in the first resonant flapping frequency, this correlates to the higher lifting forces seen in Figure 5.6, as lift is proportional to the square of the flapping frequency. However, in the case of the x3 design, it is seen that the damping ratio is much higher for the first mode when compared to all other designs. This may be a sign that the joint is too stiff in this case and may not allow the desired passive rotation of the wing (desired rotation is to rotate wing until it hits the angle stop) and correlates to the lower measured lift values seen in Figure 5.6.

Figure 5.6 shows the measured lift force as κ_h was changed. Unexpected behavior was noted as the maximum lift generated alternates high and low between designs. This effect is not well understood as multiple mechanisms were tested for each joint design and the results were repeatable. The cause of this phenomenon could be due to the angle of attack stops not being adequate enough to set a spe-

cific angle of attack along the span of the wing, as there is significant flexibility built into the wing. However, as expected from Table 5.2, the maximum lift was found for the higher flapping frequency x2.5 design and the x3 design maximum lift drops off dramatically. It seems clear that the passive rotation joint stiffness plays a role in maximum cycle-averaged lift, but there appears to be more complex interactions than the single varied parameter causing the alternating behavior as shown. Also, this alternating behavior limits the effectiveness of an independent two parameters optimization, as will become evident in the combined test in section 5.2.3.

Maximum Cycle-Averaged Lift vs. Passive Rotation Joint Stiffness
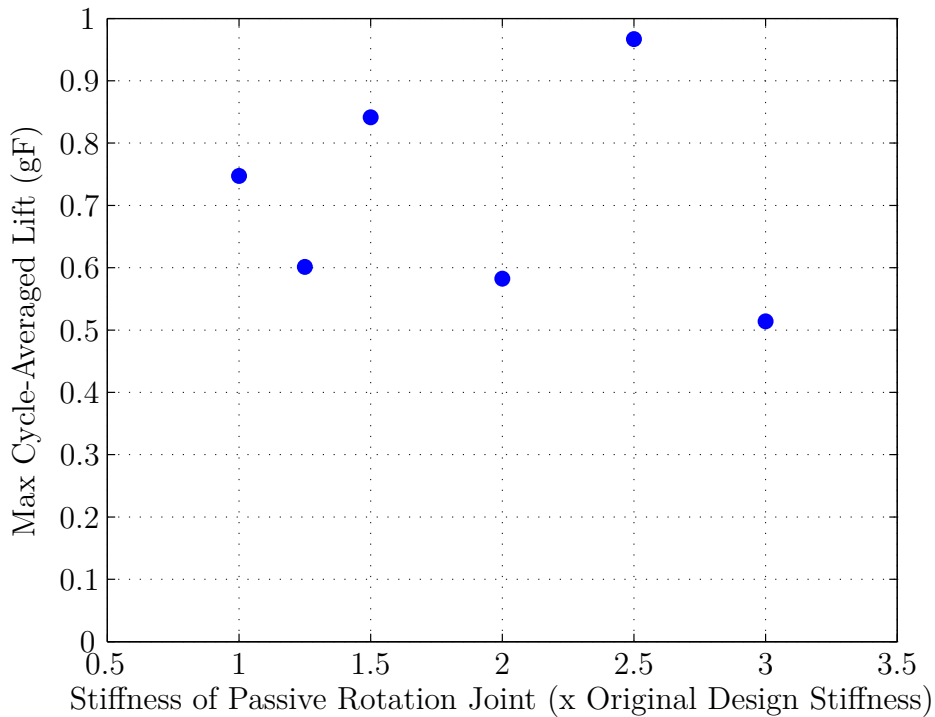
Figure 5.6: Maximum measured cycle-averaged lift for varying passive rotation joint stiffness.

Data was measured for each κ_h design as the split-cycle parameters were varied using the same input parameters that were used for the varying angle of attack stop tests. The cycle-averaged thrust was plotted versus the split-cycle parameter for each passive rotation joint design. A linear curve fit was applied to each plot and the slope was recorded as $\partial T / \partial \tau$. The results for each passive rotation joint design are shown

in Figure 5.7. The data used in calculating $\partial T/\partial \tau$ can be found in Table D.2. As already mentioned, a higher magnitude of $\partial T/\partial \tau$ is desirable as it represents more control authority when using the split-cycle waveform. As can be seen, there is a trend that as the passive rotation joint is made stiffer, $\partial T/\partial \tau$ increases in magnitude up until the x2.5 design then the trend reverses with the stiffest design. The initial trend was expected from the modal frequencies, examined earlier, showing less excitation of the second rotational mode as the stiffness was increased. However, the reversal of this trend was not predicted and is likely caused by the rotation of the wing being either too slow or too late in the stroke cycle. Reviewing the results of the modal

Average Thrust due to Split-Cycle Parameter vs. Passive Rotation Joint Stiffness
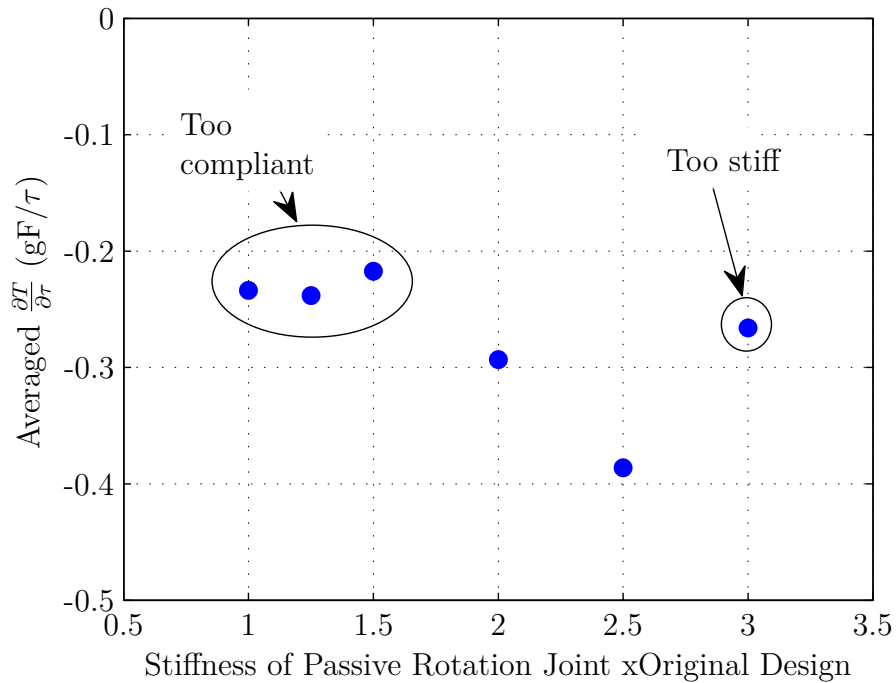
Figure 5.7: Thrust generation per split-cycle parameter as the passive rotation joint stiffness were varied.

analysis, lift force, and thrust force, the most desirable passive rotation joint stiffness is the x2.5 design. This joint stiffness corresponded to the maximum lift, maximum $\partial T/\partial \tau$, and moved the ratio of the second mode to the first mode frequencies away from the original value of 2.

Table 5.3: Experimental results of optimal α_s, κ_h and combined designs for lift and thrust production and ω_{n2}/ω_{n1}.

$\alpha_{\mathbf{s}}$ **Design**	**60°**	**45°**	**60°**
$\kappa_{\mathbf{h}}$ **Design**	**Original**	**x2.5**	**x2.5**
Lift (gF)	0.79	0.97	0.63
$\partial T/\partial \tau$	−0.89	−0.39	−0.20
ω_{n2}/ω_{n1}	1.9	2.2	2.4

5.2.3 Combined Test. The optimal results from the two separate parameter design studies, 60° α_s and the x2.5 κ_h design, were then combined in a single mechanism. This single-wing flapper produced an average of 0.63 gF of lift, -0.20 $\partial T/\partial \tau$ and the ratio of the first resonant mode to the second resonant mode was 2.4.

Table 5.3 compares the results of the independent parameter designs with the combined results and demonstrates that the optimization of these hinge parameters separately and then combining the results into a unified design did not produce an optimized hinge design for a given wing. As a follow on research effort, an optimization process should be used that varies the two parameters together, while still minimizing the total number of prototypes and testing that need to be accomplished.

5.3 Summary

In this chapter a design study was conducted on the two components of the passive rotation joint with the goal of maximizing lift and thrust generation. It was found that the angle of attack stops, when varied independently, were ideally 60 degrees to maximize both lift and thrust. Next, when performing an independent optimization of the passive rotation joint stiffness a design x2.5 times stiffer than used previously was found to clearly maximize thrust and at least influence the lift generation. Also, it was shown that the stiffness of the joint directly influenced the flapper's second system resonance. When the results of the two independent optimizations were combined performance did not improve over the independent optimizations as expected, and it did not produce an optimal design. A multiple dimension optimization technique

should be used in the future when optimizing these components. The 60 degree angle of attack stops were used for the rest of the work with the *M. sexta* based designs; however, the stiffness of the joint was kept at the original design. This was done as the angle of attack stop design gave a more clear result on lift generation and that was the primary need for the additional work. In the next chapter, the development of optical trackers for use in the closed-loop control experiments discussed in Chapter VII will be covered. These trackers were key as without their development there would have been no feedback signals to use in order to close the loop in the control experiments.

VI.   Optical Tracking of Flapping Wing Micro Air Vehicle

In order to perform experiments as described in Chapter VII, some sort of feedback data was required to close the loop. Since current prototypes have no on-board accelerometers or gyrometers, a system was developed using off the shelf web cameras to provide position and angle information. The system was developed in a build-up approach, adding complexity as additional DOF were desired. To this point, only single DOF tests have been preformed, so the initial tracker has been adequate. However, in anticipation of multiple DOF tests, the initial tracker has been improved upon with the final version being capable of estimating 3 DOF position and 3 DOF angle information by using a multi-calibrated camera approach. The webcam tracker will be detailed next following the same build-up approach used in the development.

6.1   Two Degree of Freedom Tracker

Initially, the requirement of the webcam tracker was to provide position feedback information using a single off the shelf webcam. The tracker was developed using MATLAB and Simulink to speed its development compared to a traditional compiled language such as C++. The basic technique used in this tracker was first background estimation, followed by thresholding.

Background estimation is the technique of removing the non-essential information in a frame while leaving the foreground information for future processing. Background estimation has the challenge of dealing with a changing background due to illumination changes, motion of the camera or foreground, and changes to the background. The techniques used in this webcam tracker are based on the Simulink demo "Tracking Cars Using Background Estimation" [72]. There are three different techniques of estimating the background implemented. Each technique has different computational requirements, as well as different sensitivities to the background estimation problems. The first technique is estimating the median over time. Using this technique the current frame is subtracted from the previous frame to get an estimate of the foreground pixels. The remaining pixels are the background pixels. At each

time step this is repeated and the mean and standard deviation is calculated of the background pixels. If the standard deviation of the the background pixels remains small, the mean value is used for the background. However, if the standard deviation ramps up, a change in the background is detected and the estimator will decay older values of the background until the standard deviation ramps down providing a new estimate of the background. This process continues until the test is complete. The benefit of this technique is that it is very robust to changing backgrounds and moving objects. The disadvantage is the memory and computation requirements. It was found in testing that this technique is too computationally intensive to keep up with real-time tracking requirements, hence was not used in the testing in section 7.2.

The next tracker implemented was very similar to the previous except the estimation only takes place over the first 30 frames, after which the background is fixed. The benefit of this technique was a drastic reduction in memory and computation requirement once the 30 frames were completed. The disadvantage is the technique is not robust against changing lighting condition or changing background. However, in our use of the tracker with short test time, non-changing background, and an artificially lit room, these problems were avoided. Thus, this technique was chosen and used in section 7.2. To use the technique, the object to be tracked was out of the camera sight for the first 30 frames, once the background was estimated the object was moved into frame where it was then tracked. The testing was at most two minutes long, hence there was no change to the background, and the technique worked well.

The final technique used a moving object detection to estimate foreground objects, leaving the remaining objects as background. This technique was not used, as the initialization of the background is done best with moving objects. In our test we wished to start with a static object. Because of this, the tracker would not be accurate until after a test started. This technique was also slightly more computationally expensive than the previous technique.
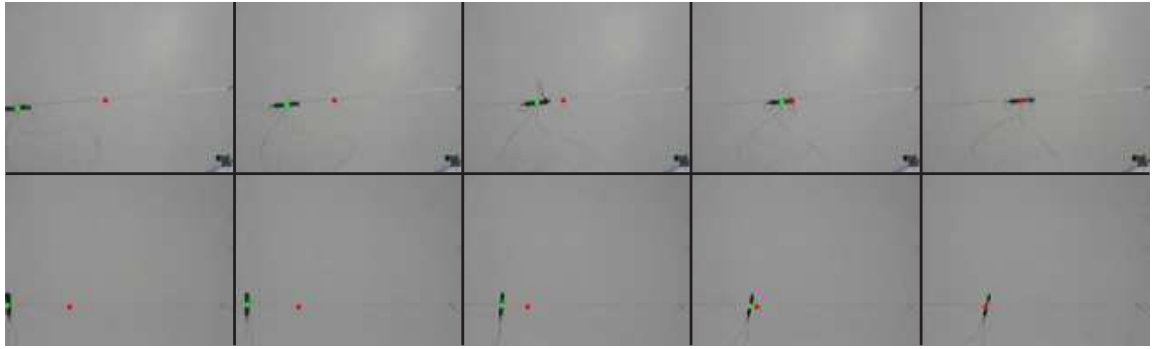
Figure 6.1: Sequence of frames from webcam tracker, red point represents the setpoint and green point represents estimated centroid position of the FWMAV. Sequence in top row shows FWMAV translating in X^B axis using symmetric amplitude control parameter. Sequence in bottom row shows FWMAV translating in Z^B axis using symmetric split-cycle parameter.

Following the background estimation, the estimated background was removed from the current frame and an "auto-thresholding" block was combined with a "closing" block to find objects in the frame. Detected objects in the frame that are smaller than a threshold value are removed leaving just the FWMAV detected. The threshold value needs to be tuned for the size of FWMAV and distance the camera is from the FWMAV. Last, the centroid of the detected FWMAV is found giving the location of the FWMAV in X-Y pixels. This location is then compared to a setpoint and the error is the feedback parameter sent to the closed-loop controller. A sequence of frames from the tracker can be seen in Figure 6.1. The red point represents the setpoint and the green point represents the estimated centroid position of the FWMAV.

6.2   Three Degrees of Freedom Tracker

The next tracker was developed with the anticipated need to provide not just two DOF position information, but to also provide a single DOF angle information. As used in section 6.1, a single camera was used for this tracker. This tracker works with the following techniques, background estimation and colored marker detection. The background estimation technique used was to save the first frame and use the first frame as the background. This technique is very simplistic and has next to zero

59

computation costs, but it is critical that the object to be tracked is off camera for the initial frame, otherwise the background estimation will not be good. This technique has the smallest computation requirements and also works well in the highly controlled environment of the lab.

Following background estimation, the foreground pixels are split into individual color channels: red, green, and blue. Two colored markers, one red and one blue, made out of adhesive backed colored paper are attached to the object to be tracked. Thresholding is then used on the individual color channels to detect the respective colored markers. This gives the X-Y pixel location of the colored markers. The centroid of the markers was then found and used as the centroid of the detected object, and the angle the two markers make with the horizontal was also calculated providing a measurable angle. The parameters of object centroid and angle with the horizontal are the 3 DOF this tracker can compare to setpoints to send back error signals to a closed-loop controller.

Another way this tracker could have been implemented would be to use the first tracker approach and find the semi-major and minor axis of the detected object. Either of these axis could be used to provide an angle with the horizontal or vertical for use as a feedback parameter. However, as will be seen in the 6 DOF tracker, it was desired to develop a colored marker detector. Hence, this tracker used colored marker detection as a buildup to the final tracker.

6.3 Six Degrees of Freedom Tracker

In preparation for eventual flight it is desired to have 6 DOF position and angle information for use in a closed-loop controller. Classically this has been done with Vicon-like systems using infrared light and reflective markers. However, systems based on this approach need to have multiple markers spaced unique distances apart from each other [73–75]. Also, each marker is a significant size and weight when compared to a prototype FWMAV's fuselage. This limits the number of markers, and more importantly limits the placement of markers with unique distances away from

each other. To overcome this problem, the colored marker tracking technique was developed and then combined with stereo triangulation and unit quaternion absolute orientation estimation to give the 6 DOF information as desired. This approach was developed with an emphasis placed on computational speed over absolute accuracy. It is expected that if the final 6 DOF information is too noisy, then a state observer can be developed to filter out the noise in the system and provide adequate feedback information.

6.3.0.1 Colored Marker Tracking. The key to multi-camera position and pose solutions is to have the same features identified in multiple cameras. In this tracker, features are differentiated by using different colors. Specifically three markers are used with the colors red, blue, and either green or yellow. Green was used originally but yellow was found to be an easier color to threshold and separate from blue. The colored marker tracking technique is the same as described in section 6.2. These markers then provide three point correspondences between a minimum of two cameras for use in the stereo triangulation procedure.

6.3.0.2 Camera Calibration and 3D Stereo Triangulation. The tracker requirements are to minimize computational difficulty and add the least amount of weight to the FWMAV, while still providing adequate position and pose information. Therefore, only three different colored markers were used. In order to perform stereo triangulation the cameras must first be calibrated.

Camera calibration is the process in which the cameras intrinsic parameters (focal length, principal point, skew coefficient, and lens distortions) and extrinsic parameters (translation and rotation with respect to a world coordinate frame) are estimated. The calibration technique used was derived from [76] and uses an intrinsic camera model like the one used in [77]. The procedure and model will be reviewed here for completeness.

The intrinsic parameters are defined as follows, first let P be a point in space of coordinate vector $XX_C = [X_C; Y_C; Z_C]$ in the camera reference frame. Next, we project this point onto the image plane of the camera taking into account the intrinsic parameters. Let x_n be the normalized image projection.

$$x_n = \begin{bmatrix} X_C/Z_C \\ Y_C/Z_C \end{bmatrix} = \begin{bmatrix} x \\ y \end{bmatrix} \tag{6.1}$$

Now letting $r^2 = x^2 + y^2$, the normalized pixel coordinate x_d after the lens distortion model is applied is:

$$x_d = \begin{bmatrix} x_d(1) \\ x_d(2) \end{bmatrix} = \left(1 + kc(1)r^2 + kc(2)r^4 + kc(5)r^6\right) x_n + dx \tag{6.2}$$

where dx is the tangential distortion vector:

$$dx = \begin{bmatrix} 2kc(3)xy + kc(4)\left(r^2 + 2x^2\right) \\ kx(3)\left(r^2 + 2y^2\right) + 2kc(4)xy \end{bmatrix} \tag{6.3}$$

Therefore the vector kc contains 5 terms; terms 1, 2, and 5 make up the radial distortion parameters and terms 3 and 4 make up the tangential distortion parameters. Once the distortion is applied, the final pixel coordinates $x_p = [x_p; y_p]$ of the projection P on the image plane is:

$$\begin{aligned} x_p &= fc(1)\left(x_d(1) + \alpha_c x_d(2)\right) + cc(1) \\ y_p &= fc(2)x_d(2) + cc(2) \end{aligned} \tag{6.4}$$

where the vectors fc and cc are the focal length and principal points for the camera and α_c is the skew coefficient defining the angle between the x and y pixel axis. The

pixel coordinates can be written as normalized coordinates as follows:

$$
\begin{bmatrix} x_p \\ y_p \\ 1 \end{bmatrix} = KK \begin{bmatrix} x_d(1) \\ x_d(2) \\ 1 \end{bmatrix}
\tag{6.5}
$$

where KK is the camera matrix defined as:

$$
KK = \begin{bmatrix} fc(1) & \alpha_c fc(1) & cc(1) \\ 0 & fc(2) & cc(2) \\ 0 & 0 & 1 \end{bmatrix}
\tag{6.6}
$$

The camera matrix is fixed and unique for each camera and must be estimated through a calibration procedure. Not every camera will require all the terms of the lens distortion model, and often times the skew coefficient will be zero for cameras with square pixels.

The extrinsic parameters are typically found for a camera after the camera matrix is found. The extrinsic parameters are specific to a camera position, orientation, and the definition of a world coordinate frame. There are two components to the extrinsic parameters; a rotation and translation. If you let P be a point space coordinate vector $XX = [X; Y; Z]$ in the world coordinate frame and let $XX_C = [X_C; Y_C; Z_C]$ be the coordinate vector of P in the camera reference frame, the two vectors are related by the following equation:

$$
XX_C = R_c XX + T_c
\tag{6.7}
$$

where R_c and T_c are the 3x3 rotation matrix and translation vector respectively.

The procedure to calibrate a camera consists of the following. First, the camera must be mounted to a location and several images are taken of a planar checkerboard pattern of known physical size at a variety of orientations relative to the camera. Next, the corresponding intersection of the squares within the checkerboard are found for each image. Next, a least squares approach is used to fit the lens distortion model and

63

camera matrix to the images. Following the model fit, the intersections are found again taking the distortion into effect. The model is then refit with the new intersection positions, this is repeated until the best fit model is found. Finally the checkerboard is placed to define the world coordinate frame and the extrinsic parameters are found using the lens distortion model and camera matrix. This process is repeated for each camera used in the tracker and the extrinsic parameters are recomputed anytime the cameras move or the world coordinate frame is redefined. The toolbox from [76] makes this procedure relatively fast and intuitive.

Following individual camera calibration, there is an additional calibration performed that relates each camera's position and pose with another camera. This calibration is performed for each pair of cameras and consists of sets of pictures where the checkerboard can be seen by both cameras. From the images a rotation matrix and translation vector relating one of the cameras to the other in the pair is found. This is the stereo calibration. Now with the described calibrations performed, if a colored marker is seen by least two cameras the position of the marker can be found in the world coordinate frame, as opposed to the camera coordinate frame as was done in sections 6.1 and 6.2.

The procedure for finding the world coordinate position of the marker from the two camera images of the marker starts first with applying the intrinsic parameters of each model to the centroid of the marker in pixels. This gives a corrected and normalized pixel position of the marker for the two cameras which we will call X_L and X_R. Now, assuming the stereo calibration was done such that the stereo rotation matrix, R, and translation vector, T, were found for the right camera with respect to the left camera. To solve for the 3D position of a point with respect to the left camera the following procedure is done.

Let $U = RX_L$, $D_{XL} = X_L \cdot X_L$, and $D_{XR} = X_R \cdot X_R$ then DD can be found using:

$$DD = D_{XL}D_{XR} - (U \cdot X_R)^2 \tag{6.8}$$

64

In addition NN_1 and NN_2 are defined as:

$$
\begin{aligned}
N_1 &= (U \cdot X_R)(X_R \cdot T) - D_{XR}(U \cdot T) \\
N_2 &= D_{XL}(X_R \cdot T) - (U \cdot T)(U \cdot X_R)
\end{aligned}
\tag{6.9}
$$

This allows $Z_1 = N_1/DD$ and $Z_2 = N_2/DD$. Next, X_1 and X_2 are found using:

$$
\begin{aligned}
X_1 &= X_L * [Z_1; Z_1; Z_1] \\
X_2 &= R^T (X_R * [Z_2; Z_2; Z_2] - T)
\end{aligned}
\tag{6.10}
$$

where $*$ indicates element-wise multiplication. Finally, the 3D coordinates of the point with respect to the left and right cameras can be found using the following equations:

$$
\begin{aligned}
X_L^L &= 1/2(X_1 + X_2) \\
X_R^R &= RX_L^L + T
\end{aligned}
\tag{6.11}
$$

where the superscript denotes the reference frame of the points. More often than not however, the location and pose of the left camera is not the desired world coordinate frame, so to convert the location from respect to the left camera to the world the extrinsic parameters of the left camera are used in the following equation:

$$
X_L^W = R_C^{-1}\left(X_L^L - T_C\right)
\tag{6.12}
$$

We now have a 3D position of a marker with respect to the world coordinate frame. This procedure is repeated for the other 2 markers providing the 3D positions with respect to the world coordinate frame of 3 markers for use in the next section. This entire algorithm, with the exception of the calibration, has been implemented in Simulink for use as a subsystem within a real-time 6 DOF tracker.

6.3.0.3 Absolute Orientation using Unit Quaternions.   The final step in the 6 DOF tracker is to take the three sets of 3D points with respect to the world coordinate frame and find the rotation and location of the FWMAV, also known as

65

the position and pose problem. Four different algorithms to perform this calculation were reviewed in [78] and are listed in Table 6.1.

Table 6.1: Summary of four position and pose algorithms.

Symbol	Solution	Point configuration compatibility				Reference
	Technique	3D	2D	1D	0D	
SVD	use svd of derived matrix	yes	special case	no	no	Arun et al. [79]
OM	use eigensystem of derived matrix	yes	special case	no	no	Horn et al. [80]
UQ	use largest eigenvector of derived matrix	yes	yes	no	no	Horn et al. [81]
DQ	use largest eigenvector of derived matrix	yes	yes	no	no	Walker et al. [82]

The 6 DOF tracker must perform well with 2D point configurations, since the points used on the FWMAV were limited to 3 coplanar points. The 6 DOF tracker also must have fast computational time and perform well in the presence of noise. The four algorithms' performance in these criteria are summarized in Table 6.2, the data was used from [78] to generate the table.

Table 6.2: Qualitative comparison of algorithm performance (1 = best, 4 = worst). The different noise parameters used are: i represents isotropic noise and a represents anisotropic noise. Execution times are only compared for small data sets.

Method	2-D stability			Execution Time
	ideal	i-noise	a-noise	
SVD	1	1	1	2
OM	4	4	4	1
UQ	2	1	1	2
DQ	3	1	1	4

Upon examining Table 6.2, the two algorithms that seem to perform best for the tracker's needs are the singular value decomposition (SVD) and unit quaternion (UQ) algorithms, which perform better than the orthonormal matrix (OM) and dual quaternion (DQ) algorithms. After examining these two algorithms in detail, and

knowing the algorithm would eventually be used in a real-time environment, the UQ algorithm was chosen. The UQ algorithm has the advantage that, in the case of coplanar points, it has a closed-form solution that consists of very simple functions containing only a handful of trigonometric function calls and does not need to solve for either eigenstructure or singular value decomposition. The SVD solution on the other hand does, as expected, require the computation of the singular value decomposition. The solution to the singular value decomposition makes the SVD algorithm slower when compared to the UQ algorithm. The UQ algorithm is described in detail in [81] and consists of four sets of calculations; centroid locations, scale factor, rotation matrix or vector, and translation vector. For this, or any of the algorithms, to work a set of markers defining a rigid body in a world coordinate frame must be created prior to solving for the position and pose information. The final position and pose information will be with respect to the rigid body defined in the world coordinate frame.

Let the points be defined in either the "right" coordinate frame as 3D points found using the tracker, as described in the previous section, as R_R, or points in the "left" coordinate frame as rigid body points defined in the world coordinate frame as R_L. First, the centroids of each set of points is found:

$$
\begin{aligned}
\overline{R}_R &= \tfrac{1}{3} \sum_{i=1}^{3} R_{Ri} \\
R'_R &= R_R - \overline{R}_R
\end{aligned}
\tag{6.13}
$$

The same procedure is done for the points in the left coordinate frame. Next, the scale factor, s, is found using the following equation:

$$
s = \left(\frac{\sum_{i=1}^{3} R'_{Li} \cdot R'_{Li}}{\sum_{i=1}^{3} R'_{Ri} \cdot R'_{Ri}} \right)^{1/2}
\tag{6.14}
$$

Next, the rotation vector is found; note the rotation vector is represented by a 4 element quaternion vector and quaternions will be denoted by using symbols with circles above them. To start the procedure for finding the rotation, first, two normal vectors, n_R and n_L, are found to the two sets of coplanar points using the following equation.

$$
\begin{aligned}
n_R &= R'_{R2} \times R'_{R1} \\
n_L &= R'_{L2} \times R'_{L1}
\end{aligned}
\tag{6.15}
$$

Where the subscripted 1 and 2 represent the first and second points respectively of the sets of 3 points making up R'_R and R'_L. The unit normals of n_R and n_L are found by dividing by their magnitudes.

$$
\begin{aligned}
\hat{n}_R &= \frac{n_R}{\|n_R\|} \\
\hat{n}_L &= \frac{n_L}{\|n_L\|}
\end{aligned}
\tag{6.16}
$$

The line of intersection of the two planes lies in both planes, so it is perpendicular to both normals. It is thus parallel to the cross product of the two normals found previously. Let

$$
a = n_L \times n_R
\tag{6.17}
$$

and the unit vector of a is found by dividing it by its magnitude.

$$
\hat{a} = \frac{a}{\|a\|}
\tag{6.18}
$$

The angle between the two planes ϕ is found from:

$$
\phi = \arccos\left(\hat{n}_L \cdot \hat{n}_R\right)
\tag{6.19}
$$

We now rotate the left points into the plane containing the right points. Let R''_L be the rotated version of R'_L. The rotation can be done using the unit quaternion, $\mathring{q}_a$, defined below:

$$
\mathring{q}_a = \cos\frac{\phi}{2} + \sin\frac{\phi}{2}\left(ia_x + ja_y + ka_z\right)
\tag{6.20}
$$

where a_x, a_y, and a_z are components of the unit vector $\hat{a}$. Let C and S be as defined below:

$$C = \sum_{i=1}^{3} (R'_{Ri} \cdot R''_{Li}) \tag{6.21}$$

$$S = \left(\sum_{i=1}^{3} R'_{Ri} \times R''_{Li} \right) \cdot \hat{n}_R \tag{6.22}$$

Next, the remaining rotation θ is found but represented as trigonometric functions. This is done to keep the algorithm using the most basic functions as possible and limits calls to trigonometric functions.

$$
\begin{aligned}
\sin\theta &= \pm \frac{S}{\sqrt{S^2 + C^2}} \\
\cos\theta &= \pm \frac{C}{\sqrt{S^2 + C^2}}
\end{aligned}
\tag{6.23}
$$

Since the quaternion representing this rotation uses half angles of θ, we use some trigonometric identities to represent the half angles of θ

$$
\begin{aligned}
\sin\frac{\theta}{2} &= \sqrt{\frac{1 + \cos\theta}{2}} \\
\cos\frac{\theta}{2} &= \frac{\sin\theta}{\sqrt{2(1 + \cos\theta)}}
\end{aligned}
\tag{6.24}
$$

The quaternion $\mathring{q}_p$ can now be found without actually evaluating the trigonometric functions:

$$\mathring{q}_p = \cos\frac{\theta}{2} + \sin\frac{\theta}{2} (in_x + jn_y + kn_z) \tag{6.25}$$

where n_x, n_y, and n_z represent the elements of $\hat{n}_R$. The final rotation is found by the quaternion multiplication of $\mathring{q}_a$ with $\mathring{q}_p$

$$\mathring{q} = \mathring{q}_a \mathring{q}_p \tag{6.26}$$

This rotation can then be expressed as a quaternion, rotation matrix, or rotation vector, as desired.

The last step, to complete the position and pose estimation, is finding the translation vector. It is a straightforward calculation given the information that has

69

been calculated thus far:

$$R_0 = \overline{R}_R - s\,\mathring{q}(\overline{R}_L) \qquad (6.27)$$

where $\mathring{q}\left(\overline{R}_L\right)$ represents $\overline{R}_L$ being rotated by $\mathring{q}$. This completes the position and pose estimation with R_0 being the position of the centroid of the tracked object relative to the world coordinate frame and the quaternion $\mathring{q}$ represents the angular orientation of the tracked object. This procedure is implemented in Simulink and used real-time to solve for the final outputs of the 6 DOF tracker. Simulated data was created to test the position and pose algorithm by creating a triangle within MATLAB that was moved and rotated. The points of the triangle represented the locations of colored markers and were passed to the position and pose algorithm. Figure 6.2 shows the performance of this algorithm with the 3 coplanar points compared to the known truth data. The algorithm performs very well with the translation vector. The algorithm struggles with some orientations, specifically when the pitch angle, θ, begins to get high while heading angle, ϕ, is also high. When used with an actual FWMAV, as opposed to example data, care will be needed when choosing the orientation of the FWMAV defined in the world coordinate frame to prevent these known performance issues. With a greater number of markers, accuracy could be increased, but only at the expense of computational time. Further, tuning the color marker tracker for more than three colors becomes challenging, since colors are a blend of three component colors either red, green, and blue or cyan, magenta, and yellow.

Each step in the 6 DOF tracker, colored marker tracking, stereo triangulation using calibrated cameras, and absolute orientation estimation, have been tested independently using recorded and real-time inputs. The algorithm has not yet been used with live recordings. This was not done as the experiments presented in Chapter VII only required the two and three DOF trackers. Future work will likely need full 6 DOF information feedback. It is expected that a single modern computer will be able to run all the steps of the algorithm for 6 DOF tracking in real-time for a 3-4 camera setup using low resolutions and 30 frames per second data collection rate. The final
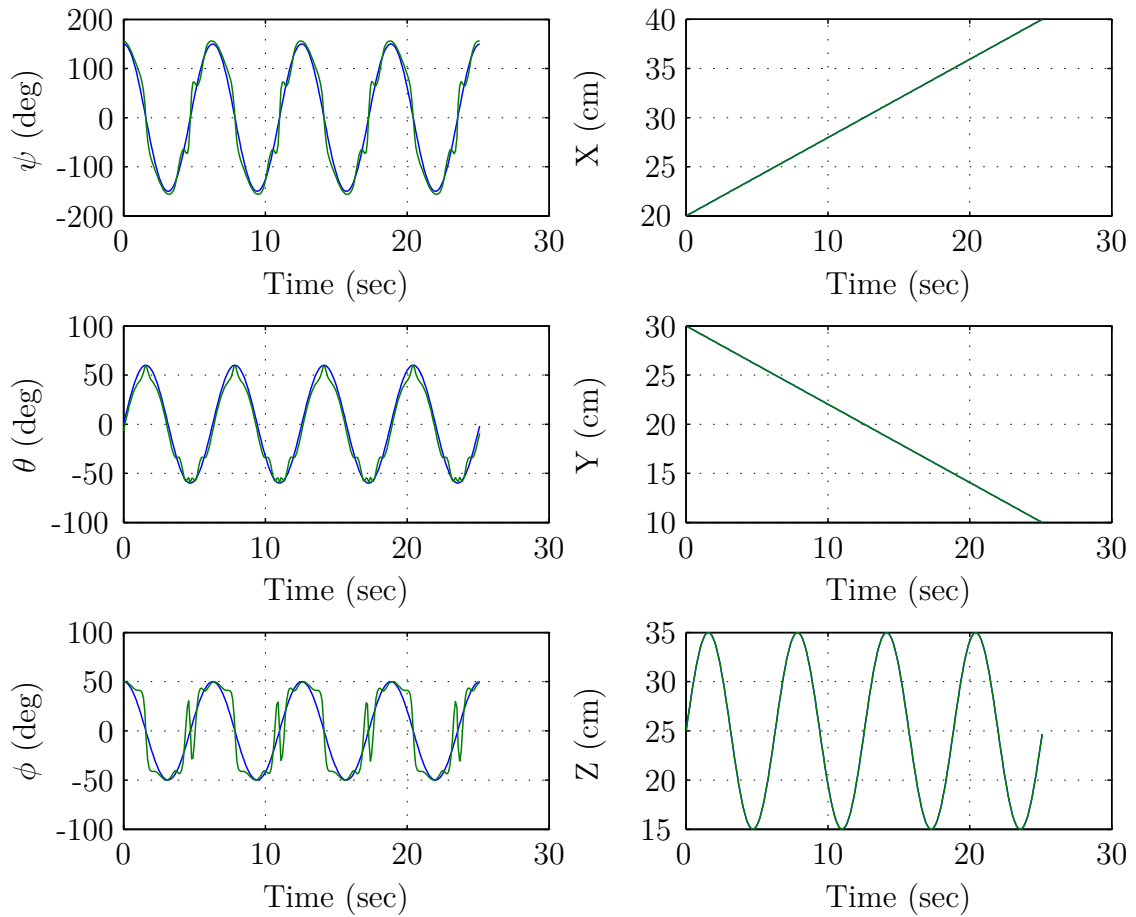
Figure 6.2: Position and pose estimation and truth data, blue trace represents truth and green trace represents estimated data.

estimated position and pose will then be sent to a controller for use in a feedback loop.

6.4 Summary

In this section three different optical trackers were developed of increasing capability and complexity. Basic background estimation and thresholding was used initially to provide simple two DOF information. Then a colored marker detection allowed for the addition of a third DOF, heading. Last, a full six DOF tracker using multiple cameras and the colored marker tracking technique combined with stereo triangulation was developed. This system provides similar capabilities to a commercial Vicon system, without the huge cost or the requirement for the markers to be unique distances from one another. In the next chapter these trackers will be used to provide feedback data in closed-loop control experiments.

VII. Hardware in the Loop, Closed-Loop Control Demonstration

In this chapter closed-loop control of a resonant flapping wing FWMAVs using BABM based controllers were demonstrated in a variety of constrained configurations. Controllers were successfully developed and demonstrated for the configuration/control parameters listed in Table 7.1.

7.1 Single Degree of Freedom Demonstration

7.1.1 Experiment Setup. The FWMAV under test can be seen in the top right of Figure 3.1. Currently this FWMAV has a lift-to-weight ratio of less than one and thus is currently incapable of free-flight. In order to better understand and prepare for eventual power-tethered free-flight of a FWMAV, two constrained configurations were tested. Figure 7.1 shows graphically, the tested constrained DOF configurations. In this work, 1-DOF configurations of X-Translation and Z-Translation were studied. These configurations limit any potential coupling between the FWMAV DOF and allow for the demonstration of the control parameters on the isolated DOF.

For each configuration, a DHPC-BABM-based feedback controller was implemented in dSPACE. Since these experiments are considered a buildup to free-flight with the desire to only demonstrate control on constrained DOF, models were not developed for controller design. Instead, PI controllers were used due to their simplicity. The feedback controllers were used to vary the BABM control parameters in order to command the FWMAV to a desired setpoint. Gains on the PI controllers were

Table 7.1: Demonstrated constrained closed-loop control configurations and control parameters.

Configuration	Control Parameter
Horizontal translation	Symmetric amplitude
Near-horizontal translation	Symmetric amplitude
Horizontal translation	Symmetric split-cycle
Heading rotation	Asymmetric amplitude
Spherical pendulum with heading	Symmetric and asymmetric amplitude
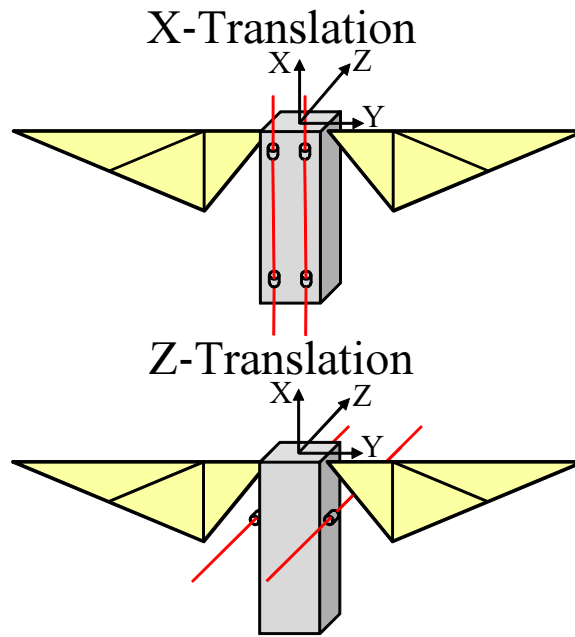
Figure 7.1: Tested constrained degree of freedom rigging configurations.
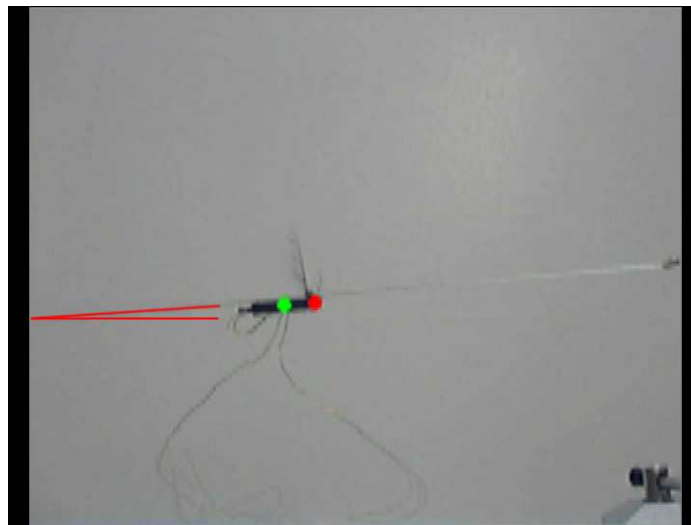
Figure 7.2: Single DOF rigging example, from the perspective of the web camera tracker. The green dot represents the FWMAV's current position and the red dot represents the set-point. The red line traces the constraint wire and the horizontal giving a clearer view of the angle of the constraint wire.

found iteratively using a dSPACE front-end, Control Desk, and manually adjusting the gains in real-time between tests. FWMAV position information was measured using a Simulink Computer Vision Toolbox based webcam tracker. The custom tracker algorithm is described in Chapter VI. The overall closed-loop experiment setup is shown and described in Figure 3.4 and section 3.3 respectfully.

During testing, a wide range of gains were tested in each configuration. A limited subset will be presented. The gains presented in each configuration are listed in Table 7.2. In the tests where the symmetric amplitude control parameter was used, a zero-error control level of 1.0 was used to represent a control signal required to maintain hover. In tests using symmetric split-cycle as the control parameter, no zero-error control level was used, again related to the signal required for hover.

Table 7.2: Closed-Loop PI controller gains used in section 7.1.

DOF	Configuration	Control Parameter	K_p	K_i
X^B	Horizontal	Symmetric Amplitude	1.4	0.0
X^B	Horizontal	Symmetric Amplitude	1.0	0.1
X^B	Near-Horizontal	Symmetric Amplitude	1.0	0.2
X^B	Near-Horizontal	Symmetric Amplitude	1.0	0.4
Z^B	Horizontal	Symmetric Split-Cycle	0.5	0
Z^B	Horizontal	Symmetric Split-Cycle	1.0	0

7.1.2 Symmetric Amplitude Results. Figure 7.3 shows the closed-loop response of the control and error signal for a horizontal test using the symmetric amplitude control parameter to translate the FWMAV in the X^B axis. The color of each trace corresponds to the same colored axis. The symmetric amplitude control parameter is a uni-directional force in the direction of the guide wire. This test used a large proportional gain of 1.4 and zero integral gain. The large proportional gain should create a small steady-state error. As seen in Figure 7.3, the error starts near 100 millimeters and is driven to near zero steady-state error, with only a small overshoot. This overshoot cannot be corrected as there is no restoring force in the horizontal configuration. In the next test, the proportional gain was reduced and a small integral

75

control was added with the hope of avoiding overshoot and driving the steady-state error to zero.
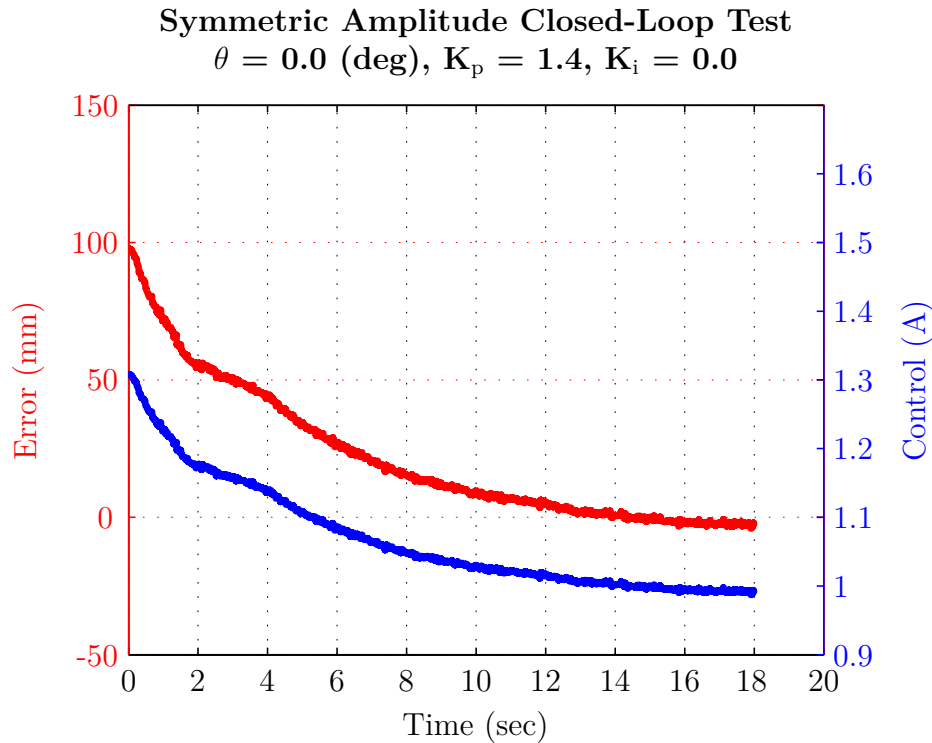
Figure 7.3: Horizontal closed-loop response using symmetrical amplitude as the control parameter, large proportional and zero integral gains.

Figure 7.4 shows the same signals as was seen in Figure 7.3; the test configuration was also the same. In this particular test, a proportional gain of 1.0 was used along with a small integral gain of 0.1. This was done in an attempt to prevent overshoot and drive the steady-state error to zero. There was, again, no restoring force in this horizontal test case as the symmetric amplitude control parameter is uni-directional. As seen in Figure 7.4, the test started with an 90 millimeter error and the controller drove the FWMAV past the desired setpoint. The integral action then wound down, eventually causing the control signal to become small, at which point the FWMAV stopped moving. This points towards using the symmetric amplitude control parameter as the primary control parameter in a DOF that has a naturally occurring restoring force to correct for these overshoots. An altitude command controller in an eventual free-flight FWMAV would be an example of using the

76

symmetric amplitude parameter in the same DOF as a natural restoring force. In the next test, we will see that the addition of gravity as a restoring force results in very small steady-state errors.
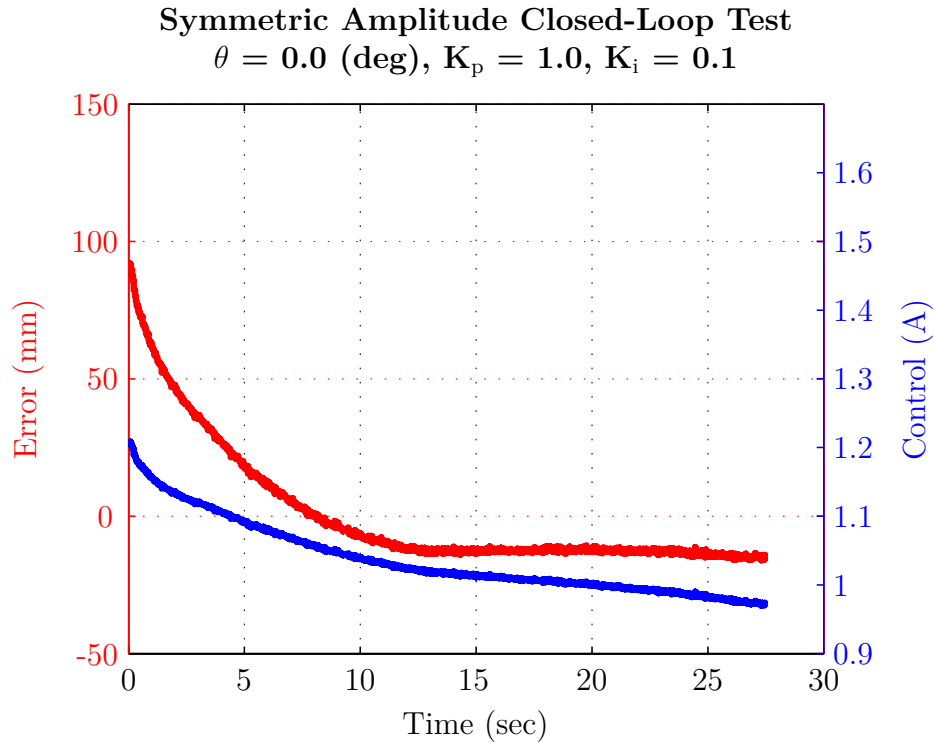
Figure 7.4: Horizontal closed-loop response using symmetrical amplitude as the control parameter, small proportional and small integral gains.

Figure 7.5 shows the response for a test done with a guide-wire rigged at a 4.6 degree incline. The incline provides a restoring force, so in the event of an overshoot, the restoring force will correct the overshoot. This allowed the use of higher gains resulting in zero steady-state error. In this case we see the FWMAV initially overshoots the setpoint; then, over time, the control signal was reduced by the integral action finally driving the FWMAV to a zero steady-state error. We also see that the steady-state control required to maintain position on the 4.6 degree incline was just below 1.2, 20% above the nominal gain of 1.0. In the next case, we will increase the integral gain and see if the zero steady-state error can be achieved faster.

Figure 7.6 shows the same response as the previous test, except in this case, the incline is slightly lower at 3.8 degrees. The same proportional gain of 1.0 was

Symmetric Amplitude Closed-Loop Test
$\theta = 4.6$ (deg), $K_p = 1.0$, $K_i = 0.2$
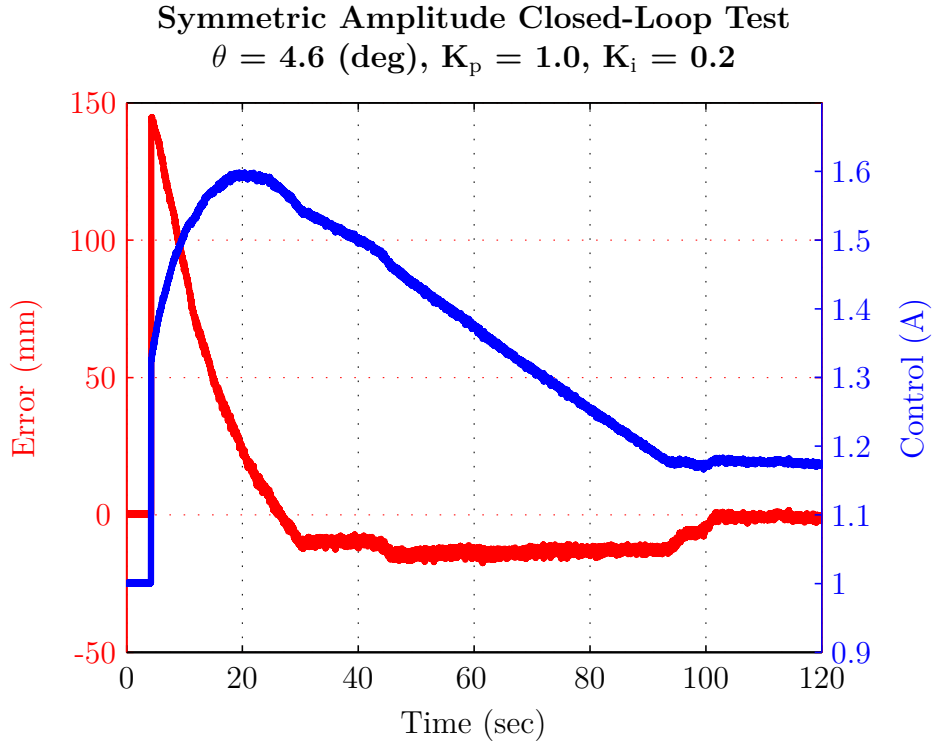
Figure 7.5: 4.6 degree incline closed-loop response using symmetrical amplitude as the control parameter.

used with double the integral gain, now 0.4. As seen in Figure 7.6, the additional integral gain winds up the control signal rapidly along with a quick reduction in the error signal, but has significant overshoot. The integral action then winds down more quickly than in the previous test and the control eventually settles on the same steady-state control value of 1.2, 40 seconds faster than in the previous test case.

7.1.3 Symmetric Split-Cycle Results. Figures 7.7 and 7.8 show the error as before, but now the control parameter is the symmetric split-cycle parameter, τ from Eq. (2.16). The symmetric split-cycle parameter is bi-directional. In this set of experiments, the FWMAV was guided by a horizontal wire allowing the FWMAV to translate in the Z^B axis. In Figure 7.7 a small proportional gain of 0.5 was used. We see the error start at 110 millimeters and the FWMAV quickly responds and drives the error to zero. In the next test, the proportional gain is increased with hopes of demonstrating a faster response time.

78
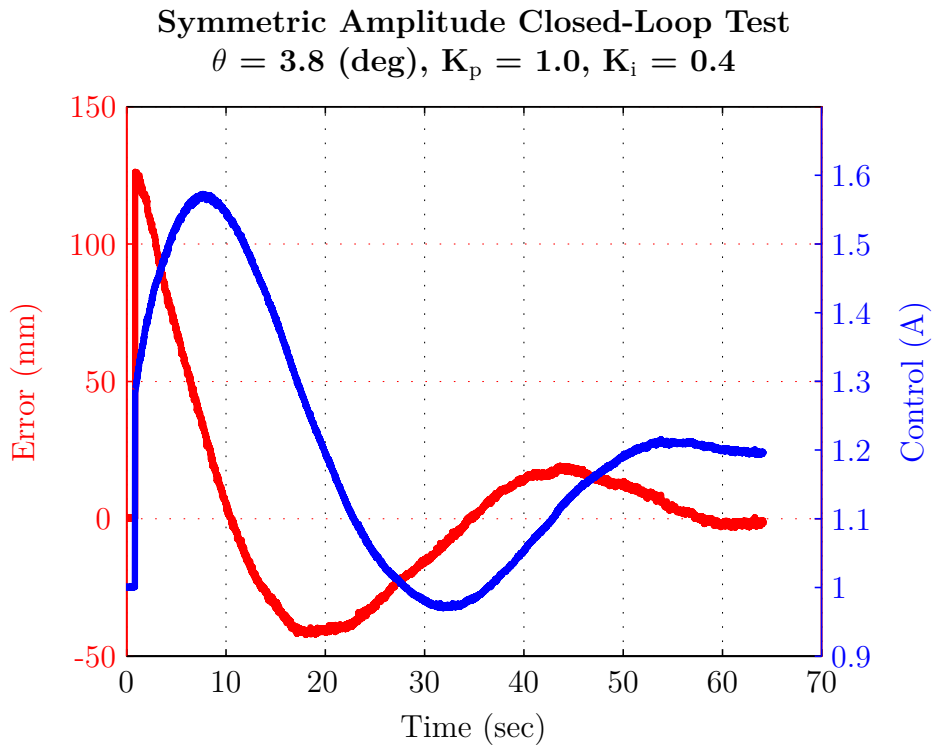
Figure 7.6: 3.8 degree incline closed-loop response using symmetrical amplitude as the control parameter.
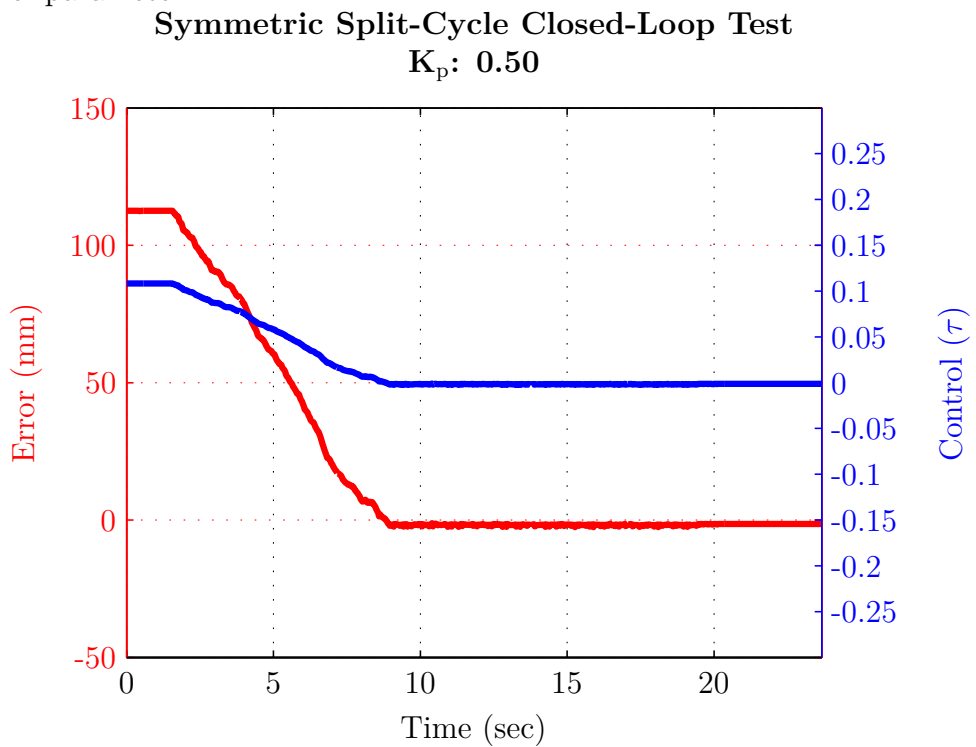
Figure 7.7: Closed-loop response using symmetric split-cycle control parameter with small proportional gain.

Figure 7.8 shows the same response and has the same configuration as the previous test. In this test the proportional gain was increased to 1.0, to produce a faster response compared to the previous test. The system responded quickly with the error rapidly dropping from 110 millimeters to a little below zero, in approximately the same time as the previous test. Thus the faster response was not seen as expected. This was most likely due to occasional stiction along the guide-wire seen in Figure 7.8 as a non-smooth response when compared to Figure 7.7. We also see a small overshoot that was not corrected by the split-cycle parameter, even though the symmetric split-cycle parameter is bi-directional. This was due to the steady-state error in this configuration being too small to generate a control signal that would overcome the stiction of the guide-wire. Future tests will add an integral gain in an attempt to overcome and drive the error signal to zero. It is expected that with adequate integral action, the symmetric split-cycle parameter can be used to enable the FWMAV to track a moving setpoint on a horizontal guide-wire. This would demonstrate the symmetric split-cycle parameter as a potential horizontal position, horizontal velocity, or pitch control parameter in eventual free-flight FWMAVs.
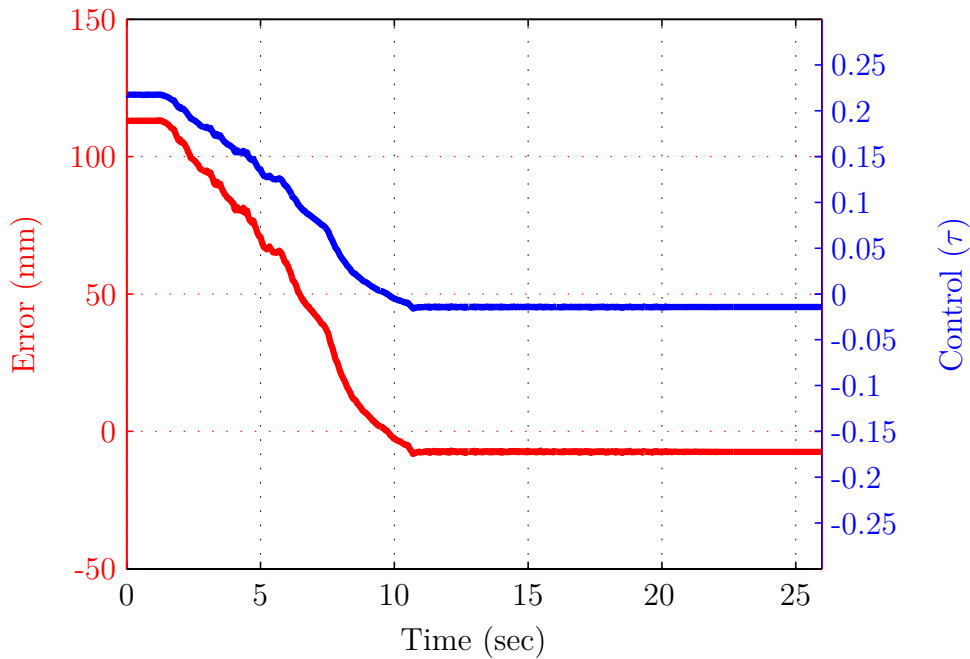
Figure 7.8: Closed-loop response using symmetric split-cycle control parameter with large proportional gain.

7.2 Spherical Pendulum Control Demonstration

In this section the FWMAV used was larger and based on biomimetic *M. sexta* wings. It can be seen at the bottom of Figure 3.1. Currently this FWMAV has a lift-to-weight ratio of less than one, thus incapable of free-flight. As in section 7.1, in order to better understand and prepare for eventual power-tethered free-flight of a FWMAV, the FWMAV was suspended in a pendulum configuration. This allows the FWMAV to move in three DOFs, X^P, Y^P, and rotate about the X^B axis. Figure 7.9 shows schematically, the tested configuration and coordinate convention, θ is the angle from Z to L and ϕ is the angle from the X to the line from the origin to (X^P, Y^P). The superscript P denotes the pendulum coordinate system. Figure 7.10 shows the same pendulum system from the camera's perspective. The cylindrical coordinate system used by the camera is clearly seen in terms of R and ϕ along with the additional heading term, ψ. Figure 7.11 shows two annotated pictures of the experiment rig. As

is seen only a single camera is used directly above the FWMAV in the 4' by 4' by 4' test chamber.
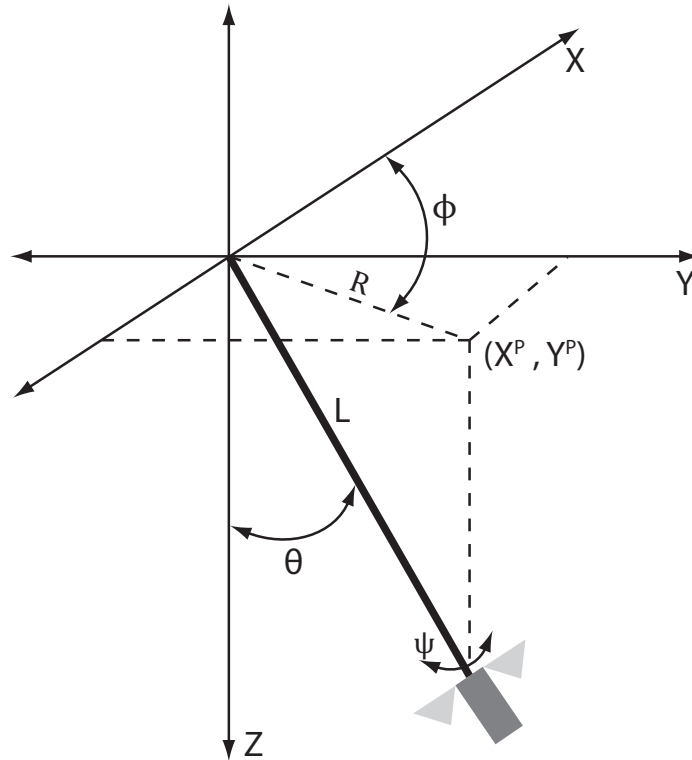
Figure 7.9: FWMAV suspended in pendulum configuration.

In anticipation for hardware testing and controller design a simulation of this configuration was developed to help understand the best method to approach the tuning of gains. The simulation did not use actual measured values for aerodynamics and mass properties, instead it was used to develop the layout of the eventual hardware controller. Real-time tuning of gains, as used previously, was used with the hardware tests, tuning the gains in the order that was found to work best in the simulation.

7.2.1 Simulation and Controller Development.   To simulate the system we will start with the equations of motion for a spherical pendulum system, and then append equations for the rotation about the X^B axis. The equations of motion for a spherical pendulum are well understood. A clear derivation is presented in [83]. This derivation is presented here for completeness and to show how the heading angle, ψ,
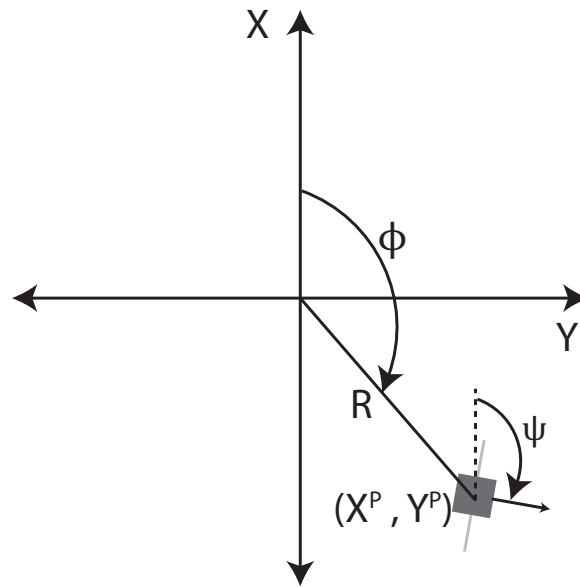
Figure 7.10: Spherical pendulum system as seen from the camera's perspective.
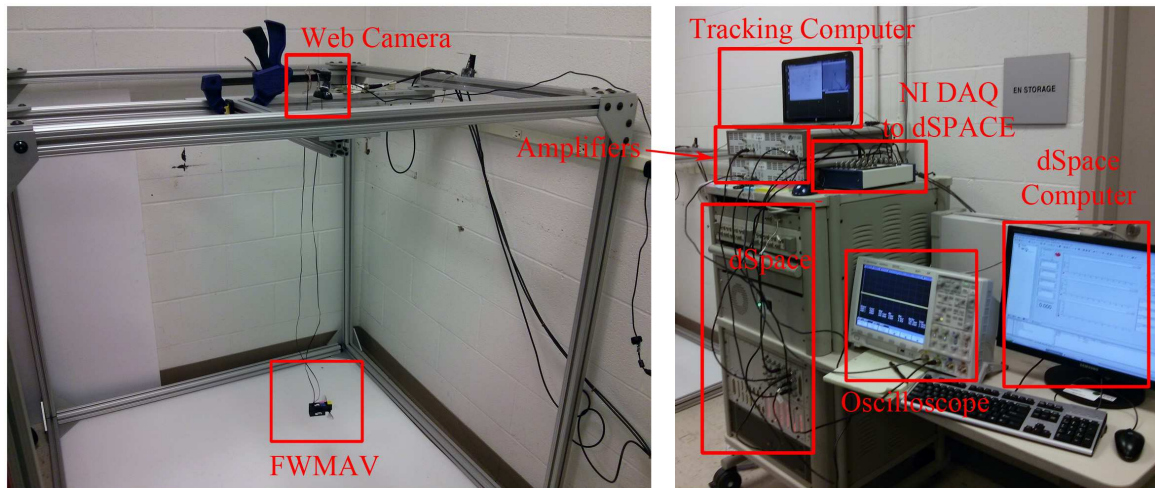
Figure 7.11: Equipment setup used in the spherical pendulum experiments. A similar setup with a different constraint configuration was used for the single DOF experiments. Test chamber measures 4'x4'x4' in size.

and aerodynamic forces were added to the equations of motion. By using a spherical coordinate transform we will convert the Lagrangian of the system from Cartesian to spherical coordinate system, which will simplify the equations of motion significantly for the spherical pendulum system:

$$X = L \sin \theta \cos \phi$$
$$Y = L \sin \theta \sin \phi \tag{7.1}$$
$$Z = L \cos \theta$$

The Lagrangian of the system:

$$\mathcal{L} = T_{KE} - U \tag{7.2}$$

where the kinetic and potential energys for the system are:

$$T_{KE} = \frac{m}{2} \left(\dot{x}^2 + \dot{y}^2 + \dot{z}^2 \right)$$
$$U = -mgz \tag{7.3}$$

where m is the mass of the FWMAV, and g is the acceleration due to gravity. By taking the first derivative of Eq. (7.1) and substituting into the kinetic energy equation we get:

$$\dot{x} = L\dot{\theta} \cos \theta \cos \phi - L\dot{\phi} \sin \theta \sin \phi$$
$$\dot{y} = L\dot{\theta} \cos \theta \sin \phi + L\dot{\phi} \sin \theta \cos \phi \tag{7.4}$$
$$\dot{z} = -L\dot{\theta} \sin \theta$$

$$T_{KE} = \frac{m}{2} \begin{pmatrix} L^2\dot{\theta}^2\cos^2\theta\cos^2\phi - 2L^2\dot{\theta}\dot{\phi}\sin\theta\cos\theta\sin\phi\cos\phi + L^2\dot{\phi}^2\sin^2\theta\sin^2\phi + \\ L^2\dot{\theta}^2\cos^2\theta\sin^2\phi + 2L^2\dot{\theta}\dot{\phi}\sin\theta\cos\theta\sin\phi\cos\phi + L^2\dot{\phi}^2\sin^2\theta\cos^2\phi + \\ L^2\dot{\theta}^2\sin^2\theta \end{pmatrix}$$

$$(7.5)$$

After simplifying the kinetic energy equation:

$$T_{KE} = \frac{m}{2}\left(L^2\dot{\theta}^2 + L^2\dot{\phi}^2\sin^2\theta\right) \tag{7.6}$$

and the potential energy equation can be written:

$$U = -mgz = -mgL\cos\theta \tag{7.7}$$

making the simplified Lagrangian:

$$\mathcal{L} = \frac{m}{2}\left(L^2\dot{\theta}^2 + L^2\dot{\phi}^2\sin^2\theta\right) + mgL\cos\theta \tag{7.8}$$

First we solve for $\ddot{\theta}$ by:

$$\frac{d}{dt}\left(\frac{\partial\mathcal{L}}{\partial\dot{\theta}}\right) - \frac{\partial\mathcal{L}}{\partial\theta} = 0 \tag{7.9}$$

where

$$\frac{\partial\mathcal{L}}{\partial\theta} = \dot{\phi}^2 mL^2\sin\theta\cos\theta - mgL\sin\theta$$
$$\frac{d}{dt}\left(\frac{\partial\mathcal{L}}{\partial\dot{\theta}}\right) = mL^2\ddot{\theta} \tag{7.10}$$

After substituting into Eq. (7.9) and rearranging we get the equation for $\ddot{\theta}$.

$$\ddot{\theta} = \frac{L\dot{\phi}^2\sin\theta\cos\theta - g\sin\theta}{L} \tag{7.11}$$

Similarly to find an equation for $\ddot{\phi}$:

$$\frac{d}{dt}\left(\frac{\partial \mathcal{L}}{\partial \dot{\phi}}\right) - \frac{\partial \mathcal{L}}{\partial \phi} = 0 \tag{7.12}$$

where

$$\begin{aligned}
\frac{\partial \mathcal{L}}{\partial \phi} &= 0 \\
\frac{d}{dt}\left(\frac{\partial \mathcal{L}}{\partial \dot{\phi}}\right) &= \ddot{\phi}mL^2\sin^2\theta + 2\dot{\phi}mL^2\dot{\theta}\sin\theta\cos\theta
\end{aligned} \tag{7.13}$$

After substituting into Eq. (7.12) and rearranging we get the equation for $\ddot{\phi}$.

$$\ddot{\phi} = \frac{-2\dot{\phi}\dot{\theta}\cos\theta}{\sin\theta} \tag{7.14}$$

The next step in deriving the nonlinear equations of motion is to add an aerodynamic thrust term to Eqs. (7.11) and (7.14). The assumption that θ would remain small in this experiment was used to simplify the thrust terms. It was assumed thrust would act in the X-Y plane only. Also, friction/stiction was neglected in the development of the simulation. This makes the thrust terms:

$$\begin{aligned}
T_\theta &= \frac{\cos(\psi - \phi)}{m}\frac{\partial T}{\partial SA}SA \\
T_\phi &= \frac{\sin(\psi - \phi)}{m}\frac{\partial T}{\partial SA}SA
\end{aligned} \tag{7.15}$$

where T_θ is the thrust in the radial direction, T_ϕ is the thrust in the tangential direction, $\frac{\partial T}{\partial SA}$ is the linearized thrust generated in the X body axis due to symmetric amplitude, and SA is the symmetric amplitude control parameter. By adding Eq. (7.15) to Eqs. (7.11) and (7.14) we are left with the first two equations of motion for the system:
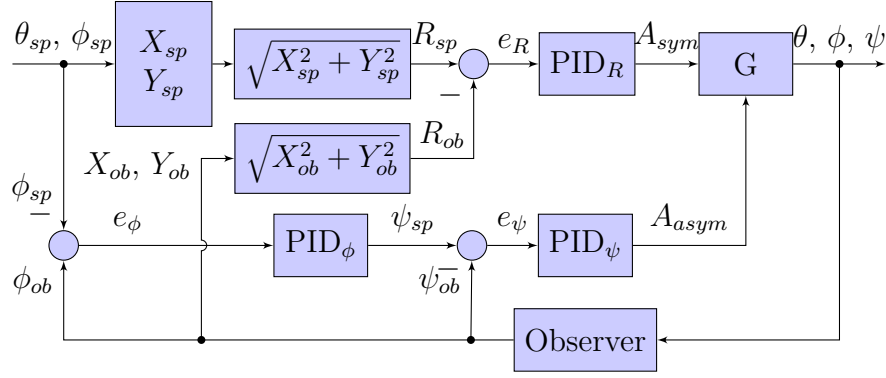
Figure 7.12: Schematic of control block diagram used to stabilize and control the simulated spherical pendulum configuration, where subscript *sp* represent setpoint, subscript *ob* represents observed values, and *e* is the error in individual parameters.

$$\ddot{\theta} = \frac{L\dot{\phi}^2 \sin\theta \cos\theta - g\sin\theta}{L} + \frac{\cos(\psi - \phi)}{m}\frac{\partial T}{\partial SA}SA$$
$$\ddot{\phi} = \frac{-2\dot{\phi}\dot{\theta}\cos\theta}{\sin\theta} + \frac{\sin(\psi - \phi)}{m}\frac{\partial T}{\partial SA}SA \tag{7.16}$$

Now given the equations of motion for the spherical pendulum we will add an equation for the third degree of freedom in this system, rotation about the X body axis. The equation of motion for the rotation about the X body axis is straight forward giving:

$$\ddot{\psi} = \frac{\frac{\partial M}{\partial AA}AA}{I_{X^B}} \tag{7.17}$$

where $\frac{\partial M}{\partial AA}$ is the linearized moment generated about the X body axis due to asymmetric amplitude, AA is the asymmetric amplitude control parameter, and I_{X^B} is the moment of inertia about the X body axis. These equations of motion were then implemented into a Simulink simulation along with a simulated camera observer and used to find a suitable closed-loop controller design.

The controller that was found to work best at stabilizing and controlling the system is shown schematically in Figure 7.12.

It was found that a PID controller to generate the symmetric amplitude parameter would control the distance from the origin R which corresponded to a setpoint θ_{sp}. Next, a PID controller was used to generate a heading command based on the error in ϕ. Last, a PID controller generated the asymmetric control parameter to control the heading. This allowed the simulated FWMAV to be controlled to set θ and ϕ. Tuning the gains was found to be best done by a succesive loop closure technique, first finding gains for the heading PID controller in a reduced ψ only simulation. Next, finding the gains for the R PID controller was found by commanding no change in ψ, thus leaving only R to be commanded. Finally, the last control was found for generating a heading command when changes in ϕ_{sp} were used. Developing the control layout and order of tuning gains was the primary goal of the simulation effort.

Simulated performance is shown in Figure 7.13. The simulated maneuver began at the origin with a zero degree heading. Then, the FWMAV was commanded to a 0.25 R value while ϕ was ramped at 1 degree per second. This traces out a circle in the X-Y plane. For this maneuver, it is seen in Figure 7.14 that R is rapidly driven to near zero steady-state error. The heading, ψ, converges to the commanded value quickly and tracks it as position ϕ continues to change. The angle ϕ responds about as fast as ψ, however we see that there is steady-state error as the commanded value is changed. The oscillation seen in R and ψ have frequency of 66 Hz and are due to the controller. Different gains could be used to change the response if these oscillations were undesirable. This demonstrated good control and understanding of the simulated system so hardware closed-loop control experiments were the next step.

Command, Error, and Response of Simulated Spherical Pendulum Experiment
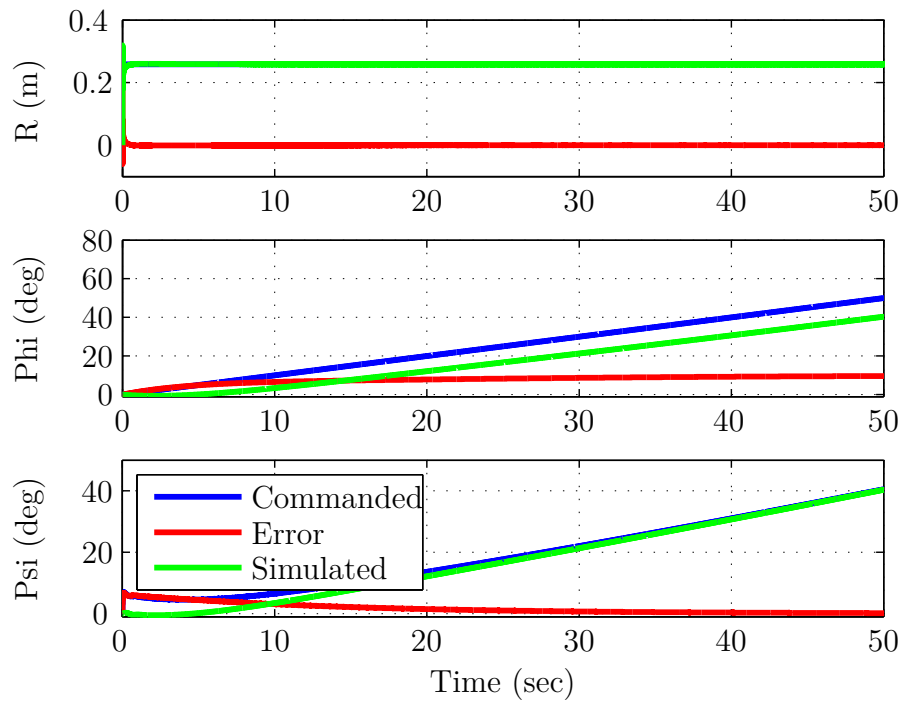
Figure 7.13: Simulated results of the spherical pendulum experiment. In the top sub-figure the simulated green trace is overlapping with the commanded blue trace.

Command, Error, and Response of Simulated Spherical Pendulum Experiment, Zoomed In
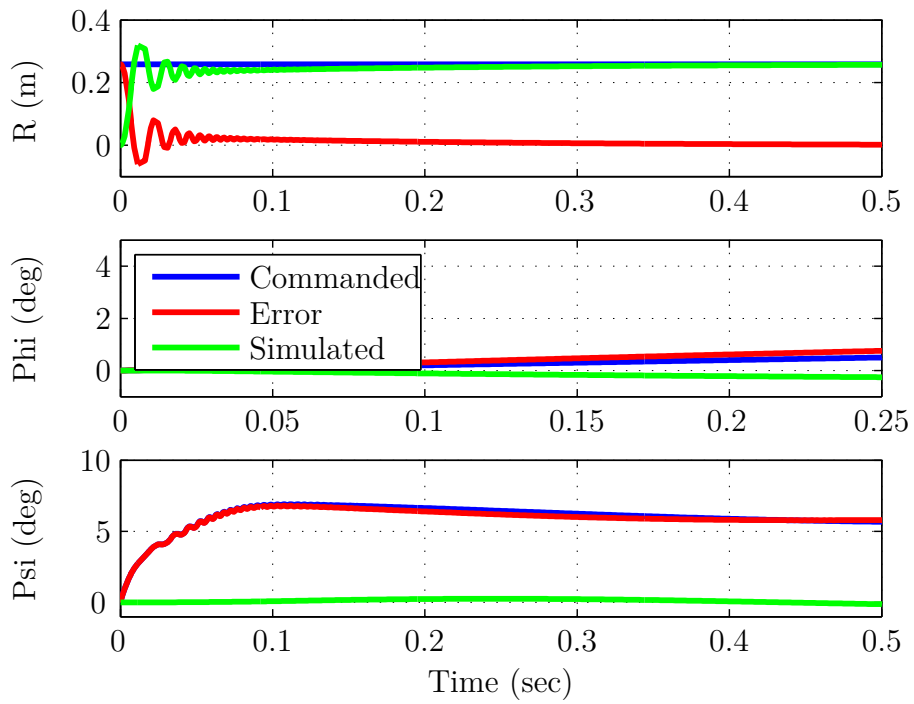
Figure 7.14: Simulated results of the spherical pendulum experiment, zoomed in on the initial response of the system.
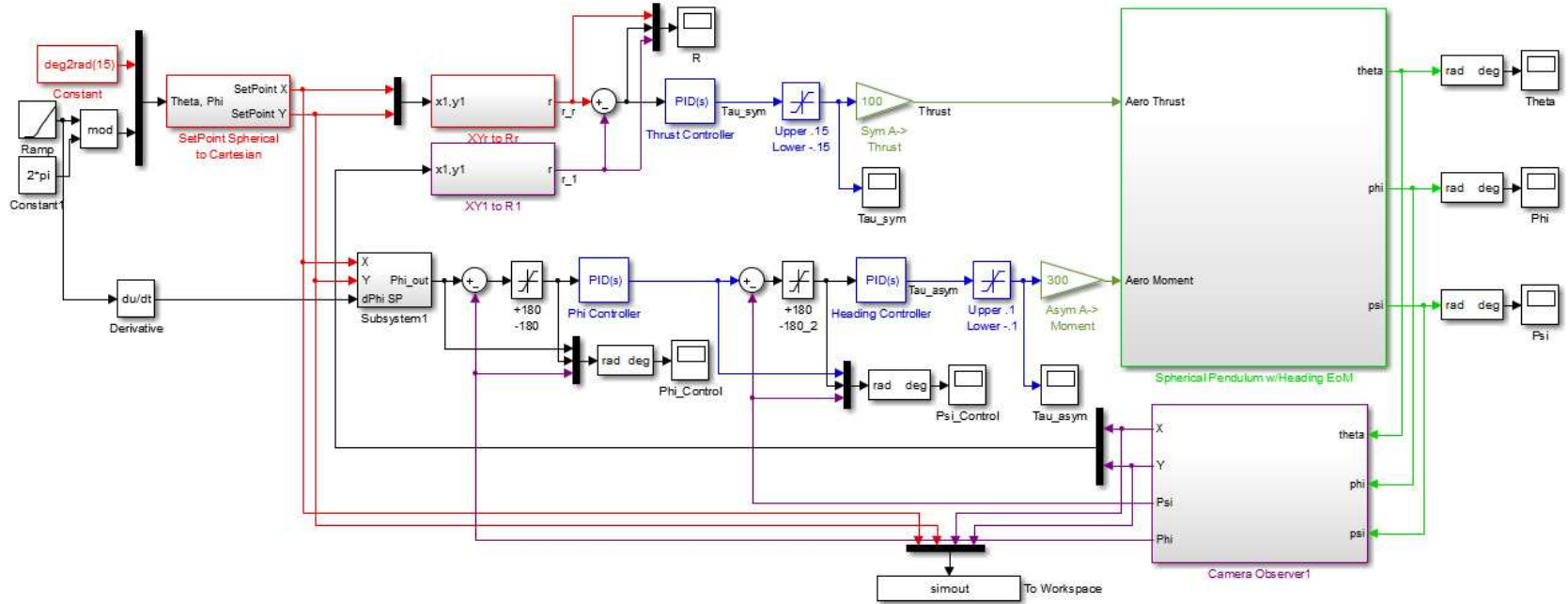
Figure 7.15: Simulink model used to create the simulation of the spherical pendulum experiment.

7.2.2 Symmetric and Asymmetric Amplitude Control Parameter Results.
Implementing the rigging shown in Figure 7.9 proved to be challenging. Multiple different equipment configurations were tried including bearings, and spherical bearings of different size. There were two issues in finding an adequate equipment configuration. First, friction in the bearings tested was too large. Second, spring-like resistance caused by the wires providing the drive signal limited the motion of the FWMAV. Increasing voltage would be one option of overcoming the friction in the system; however, it was desirable to maintain relatively low voltages (less than 40% of max rated) in order to preserve the FWMAV service life. A configuration using monofilament line was found to minimize friction leaving only the spring resistance of the drive wires as seen in the left image of Figure 7.11.

Schematically the experiment was setup as shown in Figure 3.4. Tests were first done to tune a PID controller for heading control using the asymmetric control parameter. This was done in real-time as used in previous tests. Proportional gains, K_{P_ψ}, of 0.004 and integral gains, K_{I_ψ}, of 0.006 were found to give good performance. An example test run with an initial heading of 90 degrees and a 200 degree setpoint is shown in Figure 7.16.

As seen the heading change is much slower than the simulated results. This is due to the spring resistance caused by the drive wires. Due to this resistance it was anticipated that the two PID controller setup would not be needed to control position ϕ; instead, just the single PID controller on ψ was used with an additional PID controller on R using the symmetric amplitude parameter. Figure 7.17 shows an example of performance when using both controllers.

The initial position was 0 pixels and -50 deg heading while the setpoint was 25 pixels and 25 degree heading. The gains for the heading controller remained the same as before with the addition of a derivative gain, K_{D_ψ} of 0.0001. The gains for the position controller were: proportional K_{P_R} 0.0004, integral K_{I_R} 0.0001, and derivative K_{D_R} 0.0002. The resulting performance is seen Figure 7.17. As is seen,
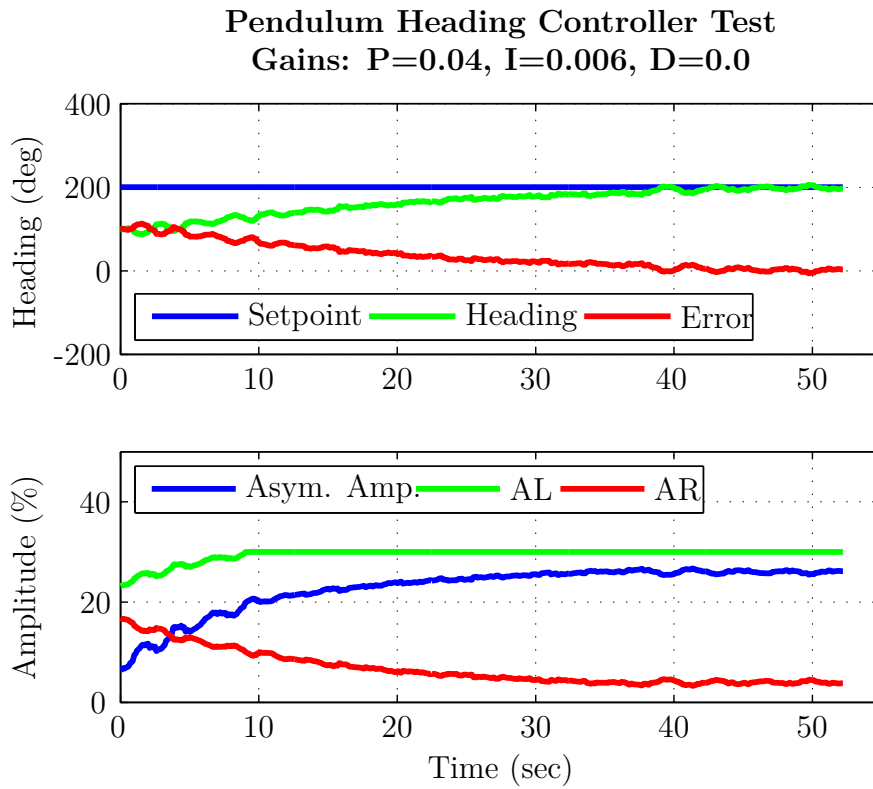
Figure 7.16: Pendulum configuration, closed-loop response of heading only controller using asymmetrical amplitude as the control parameter. Amplitude was limited to 30% of max voltage.

93

Pendulum Heading and Position Controller Test
Heading Gains: P=0.04, I=0.006, D=0.0001
Position Gains: P=0.0004, I=0.0001, D=0.0002
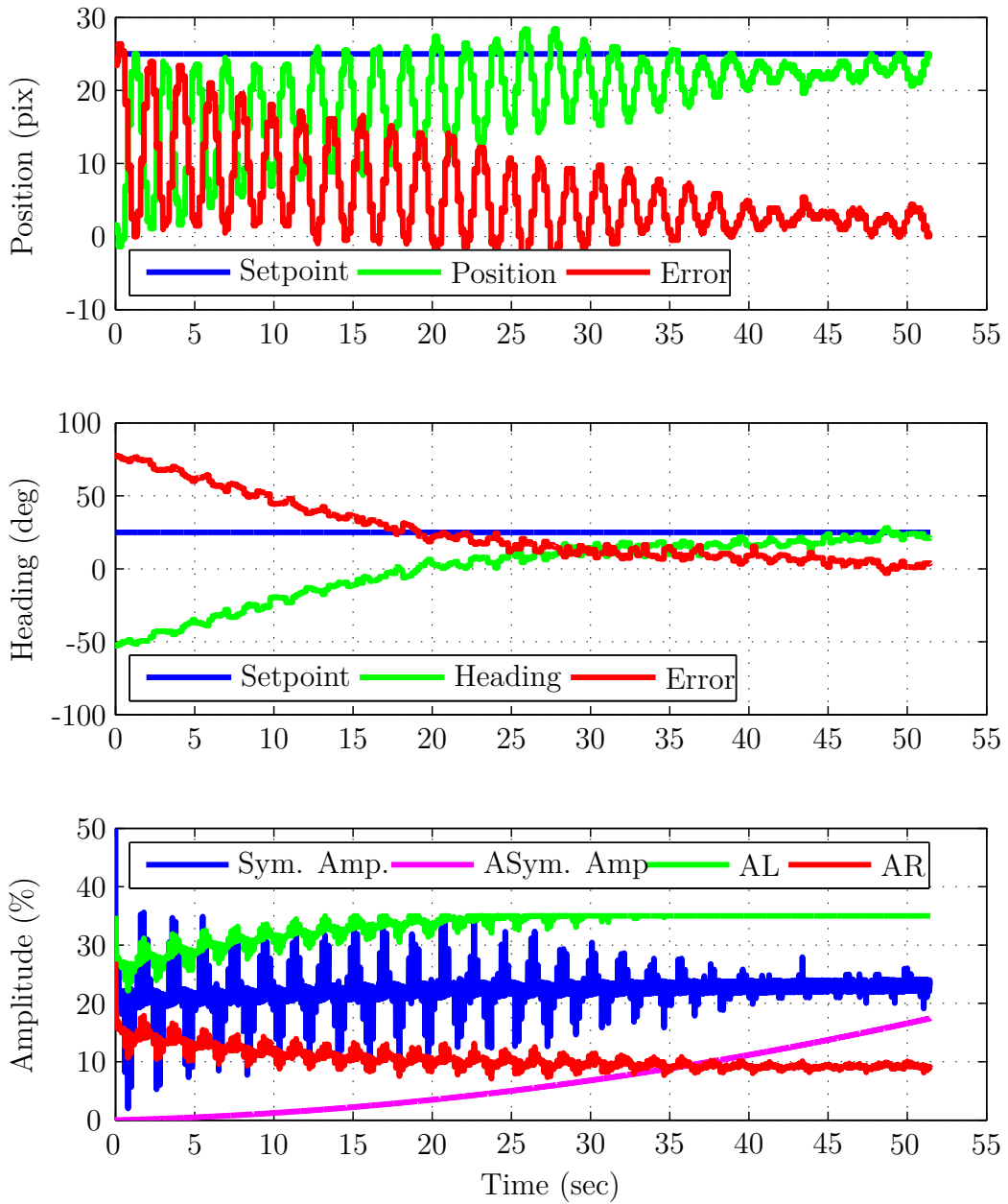
Figure 7.17: Pendulum configuration, closed-loop response of heading and position controller using asymmetrical and symmetrical amplitude as the control parameters. Amplitude was limited to 35% of max voltage.

94

the heading makes a quick and stable convergence on the setpoint with zero steady error. In contrast, the position shows a lot of oscillation before finally reaching its setpoint and maintaining relatively zero error. The frequency of the oscillations is 0.6 Hz, significantly slower than the flapping frequency of 25 Hz. The oscillations are most likely caused by a combination of the natural frequency of the pendulum, the two controllers competing, and the spring effect of the drive wires. Looking in the third subplot we see the trace in green, AL, amplitude parameter for left wing was being saturated. This demonstrates that the low voltage limitations were limiting the performance of this configuration. However, even though the response had many oscillations it does remain controlled and reaches its desired setpoint, thus demonstrating control of the configuration.

7.3   Summary

In this section various constrained closed-loop configurations and control parameters were demonstrated and simulated utilizing the dual actuator BABM control methodology. Closed-loop controllers used were simple, with the most complex used being a PID controller. This is highly desirable as a potential tether-free FWMAV will seek as simple a controller as possible to minimize power and weight required for the on-board microcontroller. The DHPC-BABM control methodology has now been demonstrated in closed-loop control utilizing these simple controllers in a variety of constrained environments.

In the next section the conclusions of this work, along with significant contributions and recommendations for future work will be presented.

VIII. Conclusions

The work described in this document represents a significant research contribution in the field of the control of FWMAVs. In the process of this research many significant contributions have been made advancing the field. The stated goal was to evaluate the thesis statement:

> *Open-loop wing control combined with closed-loop control about FWMAV position and pose is sufficient to stabilize a minimally actuated, power-tethered FWMAV in constrained configurations.*

Many different aspects of research were required in order to evaluate this thesis statement. First, a thorough review was made of previous work. Many have attempted simulation, and a few successes have been demonstrated in hardware. However, these have been with either larger or smaller scale FWMAV, and have utilized DC rotary mechanisms or more actuators and sensors than the results presented here. None of these efforts have been accomplished previously using minimally actuated biomimetic FWMAV and the DHPC-BABM control scheme.

After review of previous work, it was observed that there were no measurements given on the power consumed by the piezoelectric actuated FWMAVs. This missing piece of data prevents designers and planners from formulating design sizing and mission planning capabilities. Also, the generation of forces was known to be greatest while a piezo-driven FWMAV was flapped at resonance but, the electrical power data was again missing. This missing piece of data was collected and confirmed that power efficiency for a piezoelectric actuated FWMAV is greatest at the system's first resonance frequency.

There was a desire to improve upon previous AFIT students' FWMAV designs in order to increase the forces generated by prototype hardware. These additional forces were desired as to allow for greater influence in controlling the FWMAV in the planned closed-loop control test. The design improvements were focused on the passive rotation joint design. Two aspects of the passive rotation joint were examined, the angle of attack stops and the passive rotation joint stiffness. Both clearly impacted

lift and thrust generation, and the original design was not optimal. However, it was found that optimizing these two parameters individually was not a valid attempt. In addition, the passive rotation joint stiffness has a direct impact on the FWMAV's system second resonance. This impacts the thrust generated when using the split-cycle parameter from the DHPC-BABM control scheme and was evident in the thrust data for varying passive rotation joint stiffness.

Next, there was a known lack of on-board sensors to provide feedback data for use in closed-loop control experiments. An off-board camera based approach was an obvious choice but commercial offerings available are intended for larger vehicles and motion. They also require infrared markers to be placed on the FWMAV at unique distances in order to solve for position and pose information. A new commercial system was not a tractable solution due to the expense of such a small custom system, so a low-cost webcam based approach was developed. The development of these optical trackers was completed in phases adding additional tracked DOF as the system became more complicated. The unique addition of colored markers instead of infrared markers allows for a minimum number of markers and therefore weight added to the FWMAV. Also, these markers do not have to have unique distances from each other since the color of the marker differentiates them from each other. These trackers were then used with good performance in the final phase of this research, constrained closed-loop control experiments.

A variety of constrained hardware based closed-loop control experiments were performed utilizing multiple BABM control parameters and controlling different DOF of the FWMAV. Single DOF, and multiple DOF constrained configurations were utilized. In total, three of the five total BABM control parameters were demonstrated controlling a constrained DOF of a FWMAV: symmetric split-cycle, symmetric amplitude, and asymmetric amplitude. This leaves only asymmetric split-cycle and bias to be untested in control demonstrations. The controllers used in the demonstrations were all PID based controllers. This is ideal as it demonstrates that the complex FWMAV system can have its wings driven in an open-loop fashion and that the av-

erage forces and moments generated combined with simple closed-loop controllers to stabilize the vehicle is a viable method to fly the FWMAV. It was desirable to use the simplest possible controllers, as any future flight capable FWMAV will wish to minimize weight and power for a microcontroller, something a more complex control algorithm would require. Finally, these demonstrations show that the piezo-driven, minimally actuated, biomimetic FWMAV is a viable concept.

8.1 Research Conclusions

The tasks described above were performed to answer specific questions about FWMAV control. Additional insights were gained in areas other than control while performing this research. All these questions and insights will be described below in detail.

1. What is the optimal flapping frequency for a piezoelectric actuated FWMAV?

   Section 4.1 presented the results which answer this question. As anticipated from previous results limited to force generation, flapping at the FWMAV's first system resonance is the most power efficient in terms of lift per power consumed. Specifically Figures 4.2 to 4.4 clearly prove this point.

2. What is the optimal passive rotation joint geometry for a biomimetic *M. sexta* wing?

   There are many parameters which make up the passive rotation joint geometry. In this work two were studied: the angle of attack stops and the passive rotation joint stiffness. Chapter V went into detail on the design and experiments leading to the conclusion that an angle of attack stop of 60 degrees is optimal for lift and thrust generation over the range of tested designs. Independently, a passive rotation joint stiffness of 2.5 times the original design was clearly optimal for thrust generation, however the lift generation was less clear. There exhibited fluctuations in lift generated as the passive rotation joint designs became stiffer. The conclusion is the stiffness plays a role in lift force generation but is currently

less clear. In contrast, the increased thrust from stiffer passive rotation joints can be attributed to the movement of the system's second resonance.

3. What approach to passive rotation joint geometry should be used for design?

   Combining the two independent design study approach shown in Chapter V when combined did not create an optimal rotation joint geometry. It was shown that these parameters influence each other and should not be optimized independently in future work developing passive rotation joint geometries. The different parameters of the passive rotation joint should be optimized using a multi-dimensional approach, such as design of experiments, as opposed to independently optimized and then combined.

4. How can a FWMAV design influence the system's second resonant frequency?

   The passive rotation joint stiffness was demonstrated to have a direct influence on the system's second resonant frequency. This is very useful to the potential FWMAV designer as the DHPC-BABM control scheme depends on using a two harmonic waveform to drive the wings. Previous designs placed the second resonant frequency on the second harmonic of the DHPC-BABM waveform and was being over excited violating assumptions behind the DHPC-BABM control scheme.

5. Is the DHPC-BABM control scheme sufficient to stabilize and control FWMAV in constrained configurations?

   Chapter VII details the closed-loop control demonstrations performed proving that the DHPC-BABM control scheme is capable of stabilizing and controlling a FWMAV in a variety of constrained configurations. Three of the five BABM control parameters have been demonstrated to date. Experiments have been performed and stabilizing and controlling both single DOF and multi DOF constrained systems using different combinations of BABM control parameters. One of the major challenges to these constrained demonstrations was due to interference caused by forces generated by the power-tether wires acting like

springs. This could be avoided in the future by running the dynamics in a simulation while using the static setup to provide the aerodynamic data, or ideally implementing a small microcontroller, battery, and amplifier into the FWMAV frame.

6. Can a low-cost camera be used along with optical tracking software to provide feedback signals for testing a FWMAV in a lab environment?

   The trackers developed in Chapter VI were used with success in Chapter VII to provide the feedback signals allowing for the control loop to be closed. This demonstrates that inexpensive web cameras are sufficient when used with adequate software to provide feedback signals for FWMAV closed-loop control work. The six DOF tracker was never required for experimental and use thus remains unproven. However the techniques were demonstrated in simulation and depend on the colored marker tracking used in the experimentally tested three DOF tracker. The only limitation on using the six DOF tracker in real-time may be the computational power of the computer. However, this can be easily resolved by having a computer for each camera all sending their individual data to a central computer which performs the position and pose calculations.

7. What limitations can be identified in the BABM control scheme?

   With current designs the primary limitation to the BABM control scheme is under performing the predicted forces and moments. Specifically, forces generated using the split-cycle parameter seem to be lower than predicted. The cause of this was seen in high-speed video where the assumption of a steady angle of attack was being violated. Stiffer passive rotation joints seem to help with this issue as seen in section 5.2.

   Depending on a given wing, passive rotation joint, and linkage design the measured system FRF values can saturate the BABM waveform second harmonic. This limits the effective range the split-cycle can be used before maximizing the actuator's voltage.

Split-cycle parameter effective range was much smaller than originally proposed. Originally a range of ± 0.25 was proposed as the range for τ, after which the BABM waveform is no longer generating a split-cycle waveform. However, it was found experimentally that thrust values dropped with values used beyond $\pm 0.05\ \tau$. This corresponded with a decrease in stroke amplitude which could be compensated for by adding additional amplitude to the BABM waveform, but that quickly saturates the voltage that the actuator can handle. This issue may be design specific as only a limited number of wings or linkages were examined.

8. What limitations can be identified in the biomimetic *M. sexta* wing?

The only limitation discovered in the biomimetic *M. sexta* wing has to do with the torque it generates and places on the passive rotation joint. It could be also said that this is a limitation of the passive rotation joint, but as the two are linked the issue will be described here. At large flapping amplitudes the service life of the wing/passive rotation joint is limited, as the passive rotation joint has a tendency to shear off from the larger forces being produced by the wing. This result was limited somewhat by using two angle of attack stops per wing, attempting to limit these torques across the joints. This helped, as the wing service life was increased, but the primary failure mechanism eventually was still the passive rotation joint shearing off. This is the same conclusion mentioned by DeLuca in [11].

9. What are the hurdles to a power-tethered AFIT FWMAV free-flight?

One critical hurdle to flight currently is unnecessary weight in the commercial piezoelectric actuators. The biomimetic *M. sexta* wings are providing lift forces that are on par with nature. There is room for improvement on force generation by optimizing the passive rotation joint further, and perhaps some gains to be made by optimizing the 4-bar linkage. The improvements possible in force generation are small when compared to the reduction in weight that could be achieved if the actuators were optimized for weight [84]. Previous efforts have

shown custom actuator production to be challenging. An analysis of the require-
ments should be performed in order to design optimal actuators for the *M. sexta*
wing. The optimized actuator design could be manufactured by a commercial
source with the ability to use carbon fiber as the inner layer, instead of the the
stainless steel that is currently being used. This could cut the weight of each
actuator significantly and would bring AFIT much closer to a power-tethered
flight capable FWMAV.

8.2 *Significant Contributions*

In the course of this work, several contributions have been made to the field of
FWMAVs, which are significant:

1. Proved that flapping at the FWMAV's first system resonance is most efficient.

   Previous work has shown that flapping at the first system resonance generated
   the most lift. The addition of measuring the power used, in addition to the
   forces generated, discussed in section 4.1 proves that flapping at the system's
   first resonance is most efficient flapping frequency from a lift generated per
   power used.

2. Provided power measurements for piezoelectric actuated FWMAV using BABM
   control scheme.

   These measurements are important in the development of minimum power con-
   trol laws using the BABM control scheme and also creating minimal power
   guidance trajectories. It also gives FWMAV designers an idea of the amount of
   electrical power being used by the FWMAV. This data can be used in the sizing
   of batteries for future operational FWMAVs.

3. Identified the impact of passive rotation joint stiffness to the system's second
   resonance and thrust production.

   Previous work has demonstrated the importance of the stiffness of the passive
   rotation joint to the lift generation. In this work, the stiffness of the passive

rotation joint was shown to directly influence the system's second resonance for the first time. This directly impacted the thrust generated when using the DHPC-BABM control scheme, thus identifying the passive rotation joint stiffness as an important element of FWMAV design.

4. Optimized the angle of attack stop for the current biomimetic wing and passive rotation design over the range of tested designs.

Section 5.2 showed that an angle of attack stop of 60 degrees, while using the current passive rotation joint stiffness, maximized both lift and thrust generation. This agrees with previous results in [11].

5. Developed optical trackers to provide FWMAV position and pose data.

As discussed in section 8.1 web cameras were used along with computer vision algorithms to track the FWMAVs position and pose. A novel approach was developed utilizing colored markers as opposed to infrared reflectors, commonly used in commercial systems. This optical tracking system provides a low cost multi DOF optical tracking system for use with FWMAV control research.

6. Demonstrated for the first time single and multiple DOF constrained closed-loop control utilizing the DHPC-BABM control scheme.

Previously, the DHPC-BABM control scheme had been evaluated in static experiments, measuring the control derivatives showing promise for use as an open-loop wing trajectory controller. Constrained experiments were also performed demonstrating that BABM could influence certain DOF with the control parameters. The experiments presented in Chapter VII demonstrate for the first time a FWMAV of this size and actuator configuration being controlled in a variety of constrained environments. Three of the five BABM control parameters were used in these demonstrations. Simple PID controllers were sufficient to stabilize and control the FWMAV in these experiments as opposed to more complex control schemes, this minimizes the weight and power requirements of an eventual on-board microcontroller for a future operational FWMAV.

7. Created a software framework for use in FWMAV static and dynamic testing.

   The software and experiment setup described in Chapter IV and Appendix C was designed to be well documented, reusable, and extensible by future students. To date, in addition to the work presented here, the work for three different masters degree students reused the same software and hardware configuration. The closed-loop setup described in Chapter IV also presents a solution to closing the loop for future FWMAV researchers at AFIT.

8.3   Recommendations for Future Work

The work performed here developed the ability to: measure and predict electrical power requirements for a FWMAV, track a FWMAV in a constrained environment, optimize passive rotation joint parameters over the range tested, and perform constrained closed-loop control experiments. The eventual goal of an operational FWMAV requires further work to be performed in a variety of fields.

First and foremost, extending the service life of the wing passive rotation joint mechanism while allowing the use of large amplitude stroke angles. Currently, when using larger stroke amplitudes, the wing shears off at the passive rotation joint within minutes of test time. This is a major barrier to progress on FWMAV research as each prototype takes an investment of many hours to produce and assemble. Future work should investigate a shear resistant or rip-stop membrane for use in the passive rotation joint. This will enable researchers to spend less time on prototype manufacturing and more time testing different theories and techniques with the prototypes.

Next, the current limiting factor in power-tethered FWMAV flight using the biomimetic *M. sexta* wings is the weight of the actuators. Currently, commercial actuators are used that have an inner steel layer that is far heavier than actuators made with a carbon-fiber inner layer. The current actuators are also larger than required as the desired stroke angle can be achieved without using the maximum allowable voltage. Last, the current commercial actuator's shape has not been optimized for

104

weight. Either in-house or commercial custom actuator specifications should be developed and manufactured with the desire to minimize the weight and operate at or near the maximum voltage. This should drastically reduce the weight of the current FWMAV prototypes and enable a lift to weight ratio of greater than one. This will allow for unconstrained closed-loop FWMAV control research.

Further work in developing the DHPC-BABM control scheme should focus on preparation for flight capable prototypes. The Nano17 Titanium actuator could be integrated into the dSPACE closed-loop environment leaving the FWMAV stationary, but the forces and moments measured could be used to simulate the motion of a flight capable FWMAV. The advantages of this approach are: the simulated mass of the FWMAV can be limited to a predicted value based on custom actuators, no trackers are required for feedback data simplifying the experiment setup, power-tether wires will not influence the experiment, and free-flight based control laws could be researched and developed using the BABM control scheme.

Investigations on the influence of the passive rotation joint stiffness on lift generation should be accomplished to explain the alternating results shown in section 5.2. A 3D PIV approach could be used to capture the flow field and also get a clear idea of the rotational kinematics as the rotation joint stiffness is changed. This investigation could be combined with a multi-dimensional optimization of the angle of attack stops and passive rotation joint stiffness with the goal of maximizing lift and thrust generation without adding any additional mass to the FWMAV. A design of experiments approach to this multi-dimensional optimization is an appropriate next step. This optimization will help with the eventual goal of enabling a power-tethered flight capable FWMAV prototype.

Finally, work needs to be started on developing a lightweight microcontroller, amplifier, and power source for eventual tether-free flight of FWMAVs. The power-tethers have consistently limited the ability to perform highly dynamic maneuvers and moving the power source, amplifier, and controller on-board will eliminate this

limitation. Any circuit boards used can be integrated and used as fuselage components in the FWMAV to minimize weight. Lastly, miniaturized inertial measurement units will need to be developed to provide feedback for vehicle stability and control.

Appendix A. Software Design Process for AFIT FWMAV

Previously, there was a variety of different software processes used to design an individual component or complete FWMAV for the AFIT FWMAV program. MATLAB or Corel Draw has been the starting point for previous designs. Presented in this appendix is the current design process used, which allows traditional computer aided design (CAD) software, in this case SolidWorks, to be used as opposed to vector drawing software or MATLAB. The reason the other software approaches were used in the past is that eventually the tools used for micro-machining the FWMAV are tools traditionally used by engineers to prototype circuit boards. The outline of the the design process presented is shown below:

1. Design parts within CAD software (SolidWorks)

2. Assemble parts in CAD environment to create final assembly, use this model to check fitting and design guides for eventual assembly

3. Assemble a "flat" version of the assembly for use to export into vector drawing software

4. Create engineering drawing of flat version at 1:1 scale and export to DXF format

5. Import the DXF file into vector drawing software (CorelDraw) and use this as the "Master"

6. Use the vector drawing software to create the step 1a, step 1b, step 2, and Kapton drawings

7. Export the drawings from the previous step to DXF format

8. Import the DXF file into Circuit CAM software

9. Close paths in Circuit CAM

10. Move paths to appropriate layers

11. Prepare for laser scanning software

When the above process is complete the end products are files ready to be imported into the LPKF laser Circuit MASTER software, which actually runs the laser. This process will be covered as part of Appendix B. The following sections will go through the process listed above to create the files to produce the fuselage for the FWMAV shown at the bottom of Figure 3.1. This is a rather complex final piece. This shows every part of the process. Other less complex pieces, for example angle of attack stops, have fewer steps.

A.1 Design parts within CAD sofware

Screen-shots shown in this section were from SolidWorks 2011x64 version. Step one of creating the FWMAV part is making the individual parts. Since these parts will eventually use the SCM fabrication and assembly process each part created should be flat. Typical thicknesses for parts that are going to be part of a larger assembly is 0.25 mm, as that is the thickness of two layers of 0-90-0 carbon fiber and a layer of Kapton. If the part won't be folded (for example the angle of attack stops) a smaller thickness can be used, however it is not important for a non-folding assembly. Figure A.1 shows a completed design of the "front" part of the FWMAV. More complex parts are feasible and tools, such as "fillet," can be used if desired to round off the hard corners in the internal cutouts. When making parts within SolidWorks, typically only the flexures in the linkage need to be created. The other flexures that are eventually glued into place do not need to be created.
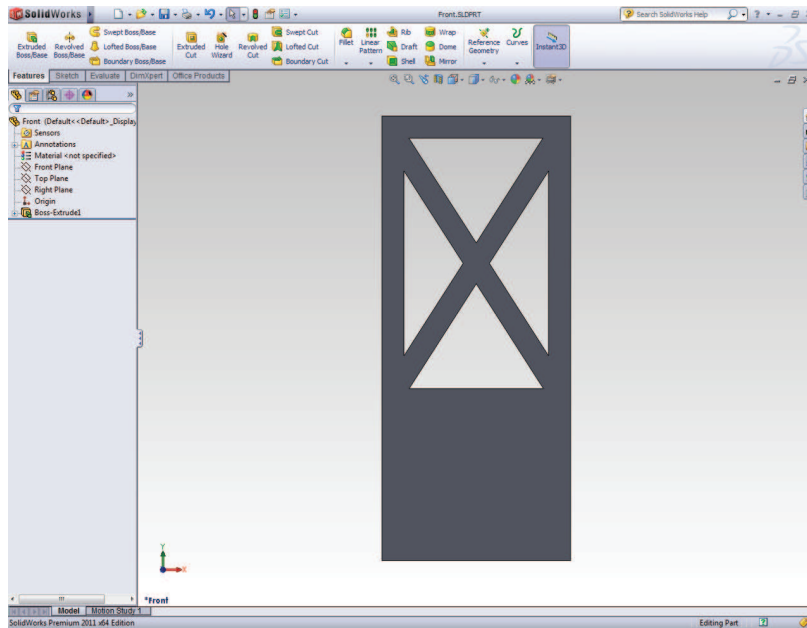
Figure A.1: The front part of a FWMAV design.

A.2 Assemble parts in CAD environment to create final assembly

Once every individual part has been created, the next step is to assemble the parts into sub-assemblies and assemblies. Creating assemblies is done as is typically done with CAD software; bring in individual parts, and then mate the parts to other parts to form the assembly. Care must be taken to account for flexures used in the assembly process. This is done by mating components edge to edge. The entire FWMAV assembly is shown in Figure A.2. Included in this assembly is also simple parts for the piezoelectric actuators. This gives dimensions for the actuator placement that can be used in the actual assembly of the FWMAV. For example the actuators for this design are 3 mm above the base of the FWMAV, so a shim 3 mm thick was made to help hold the actuators in proper position while they were glued into place. Figure A.3 shows a zoomed in section of the assembly showing how the mates of the components are done edge to edge to account for the flexures that will be used in construction.

109
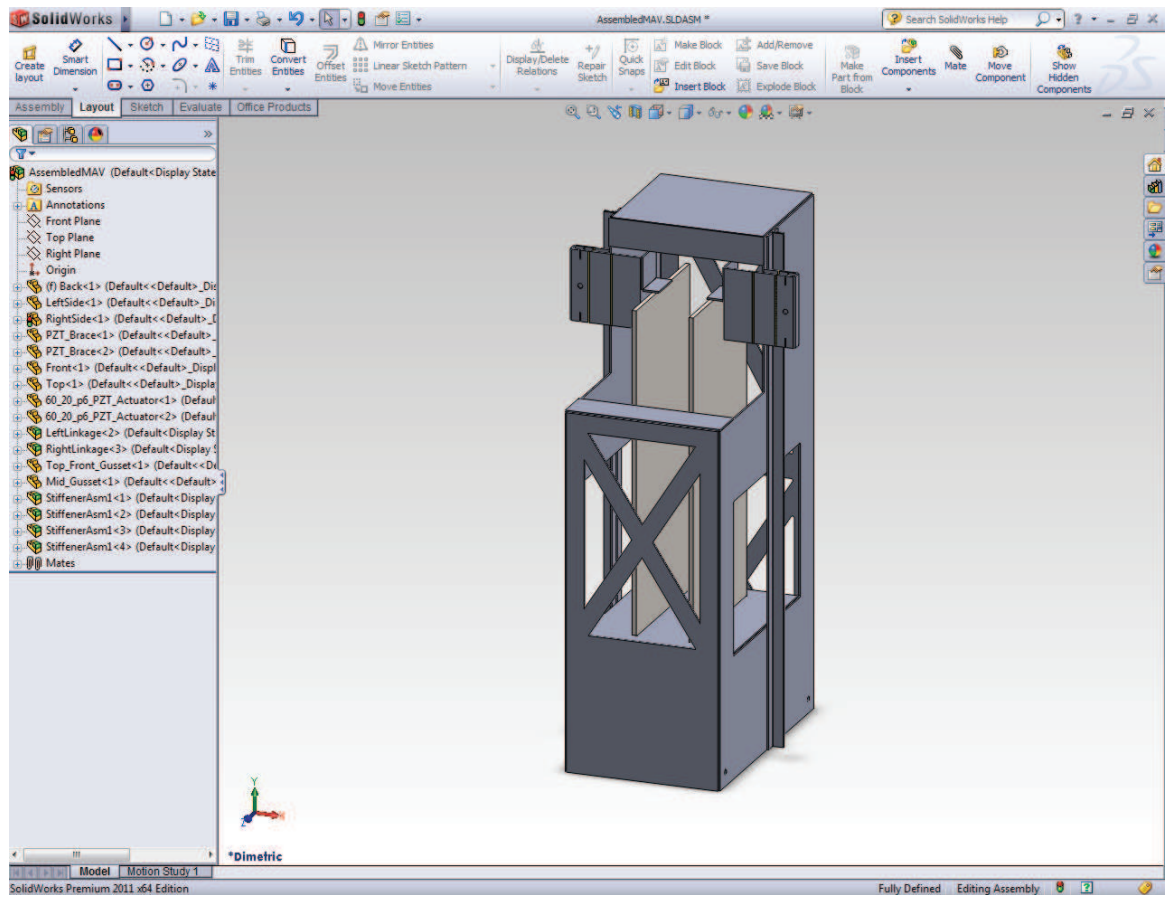
Figure A.2: A completed FWMAV fuselage with actuators assembled in CAD software.
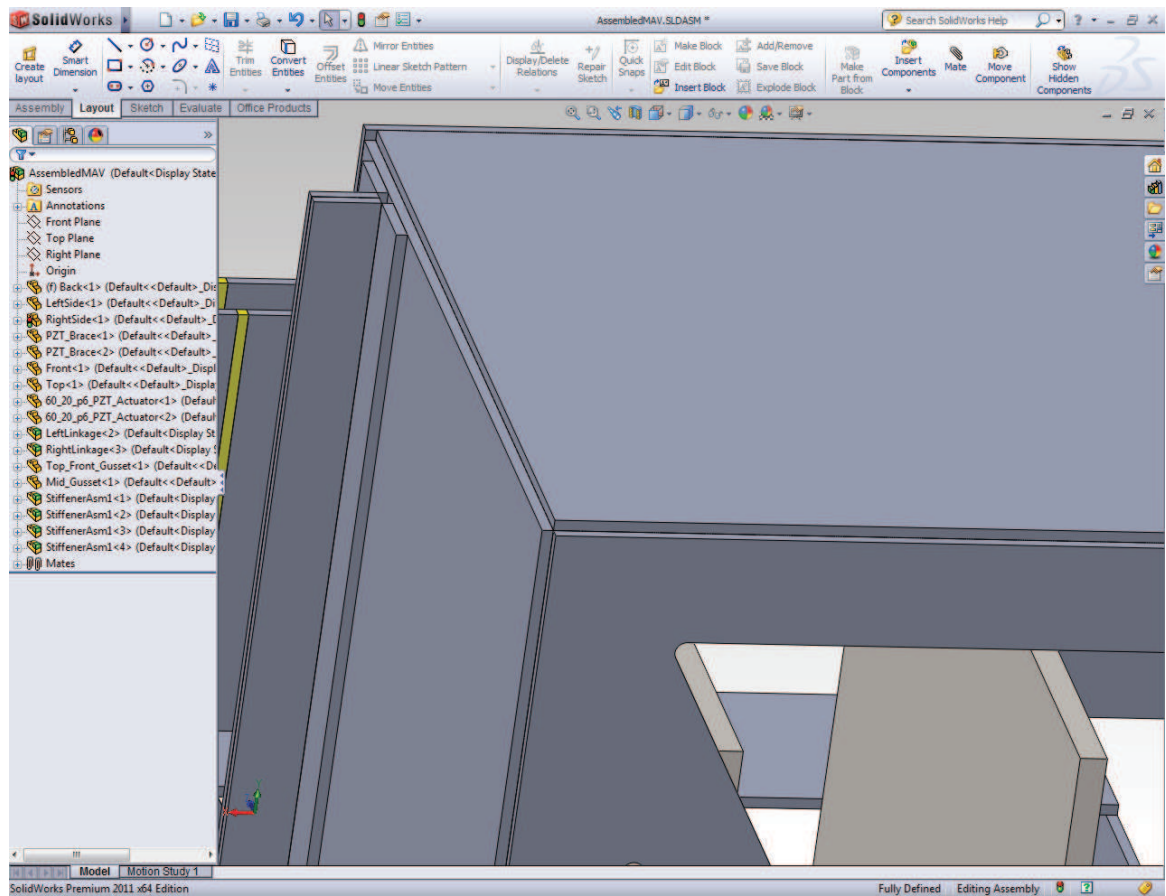
Figure A.3: Zoomed in view showing parts mated to the edges of other parts, allowing space for the flexures.

A.3 Assemble a "flat" version of the assembly

Next, a second assembly is created now that the assembled version has hopefully eliminated any clearance and alignment issues in the design. This second assembly is a flattened non-folded version of the previous assembly. It also only includes the parts that can be created in one piece, so items like actuators, wings, stiffeners, angle of attack stops, and e-clips are not included in this flat assembly as they are produced using their own flat assembly. Each flat assembly will eventually be a monolithic part cut out of carbon fiber and for folding parts carbon fiber and Kapton. When assembling the flat version, for parts that will be folded leave a 0.25 mm gap between parts while mating them together, this can be done in SolidWorks using the "Distance" mating option. For linkage parts there may be different gaps desired according to design requirements. Figure A.4 shows the monolithic flattened assembly. This part is eventually folded and makes: both linkages, the front, back, top, and sides of the fuselage, holding elements for the piezoelectric actuators, and stiffening gussets on the top and middle of the fuselage.
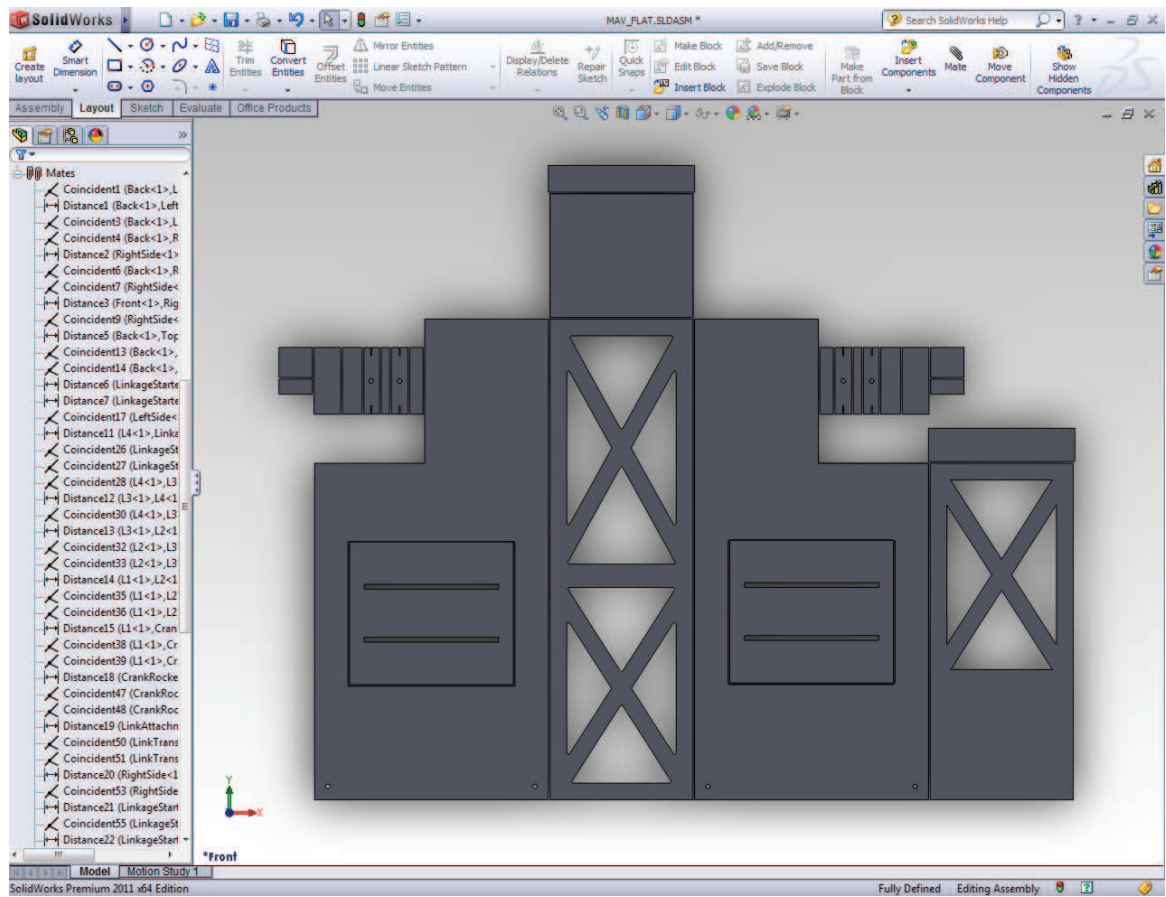
Figure A.4: The fuselage flattened assembly.

A.4 Create engineering drawing of flat version

After the flattened assembly has been created, an engineering drawing of the assembly needs to be created. This is done using the CAD package as is typical. However, since this part is flat and the thickness does not impact any remaining steps only one view is needed in the engineering drawing. The key aspect of creating the drawing is to be sure the scale of the drawing is done in 1:1. Also any additional form or drawing information can be removed from the drawing. A separate engineering drawing can be created with all the dimensions annotated on if desired for archival and design distribution purposes, but for manufacturing these annotations should be avoided. Figure A.5 shows the drawing created from the flattened part from the previous section. Once the drawing is created, export the drawing into DXF format. This will then be the file that is imported into the vector drawing software, CorelDraw X5 in this case.
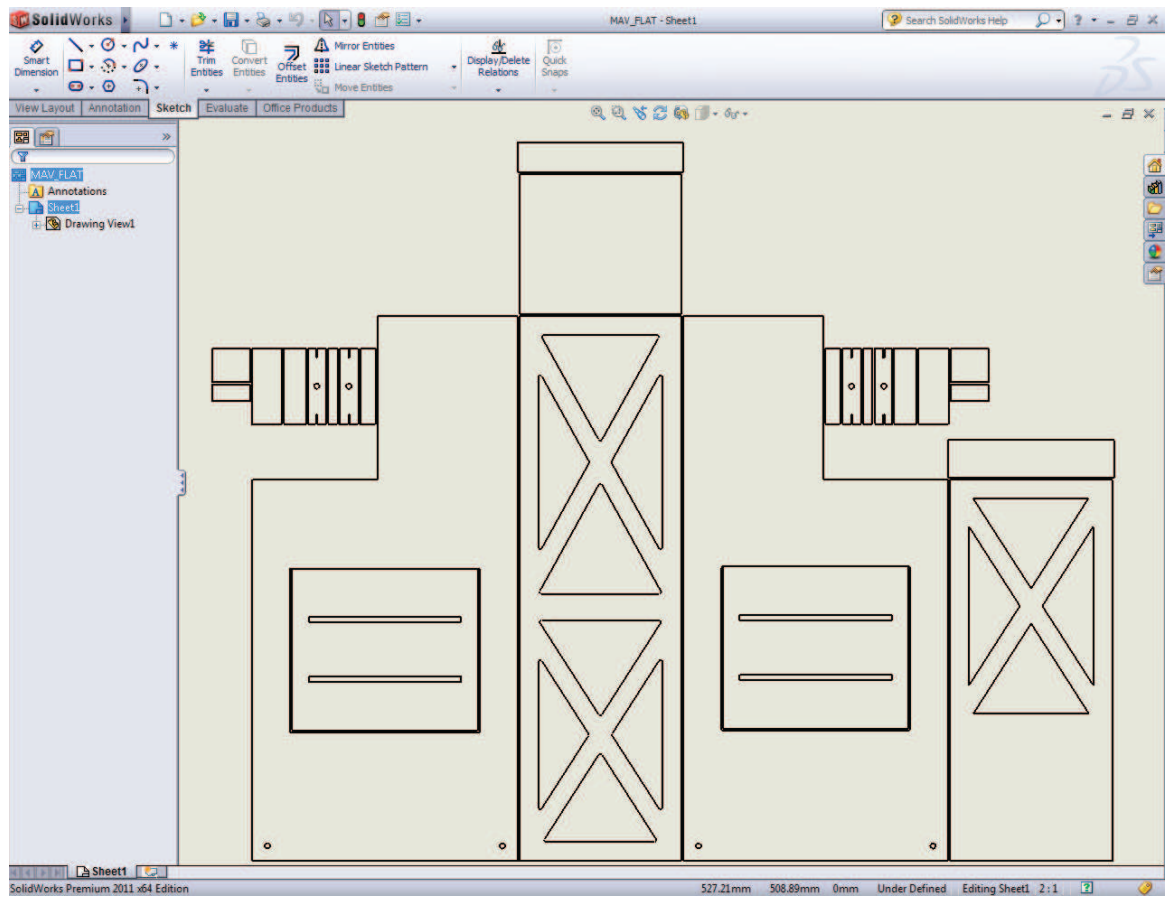
Figure A.5: Engineer drawing example used in the construction of a FWMAV.

A.5   Import the DXF file into vector drawing software

Now that a drawing has been made in 1:1 scale and been exported to DXF, open up a vector drawing software package, like Corel Draw, and import the DXF file. In Corel Draw the lines that are imported are not the thinnest possible, so select the imported lines and change the line properties to hairline thickness. This give the most precise cuts with the laser during manufacturing. If desired the different components' lines (front, top, left, etc.) can be moved into different groups which helps in organization later. Now, draw a box around the entire assembly, this will be the size of carbon fiber and Kapton that is cutout. Next, at this stage add circles for the pins used in the manufacturing process. These alignment pin circles have a 1.62 mm radius and are 50.91 mm apart diagonally. Next, add four fiducial circles. These need to be 0.5 mm in radius and should be spaced out around the part. Finally, add the text "top" someplace in between the outside box and part itself. This label makes it easier in determining which side of the part is the top side later in the manufacturing process. This makes up the entire master layer, be sure all the elements are in one layer. Now make three copies of the master layer and paste them into different layers labeling them step 1a, step 2, and Kapton. Figure A.6 shows a completed master layer created in this step.
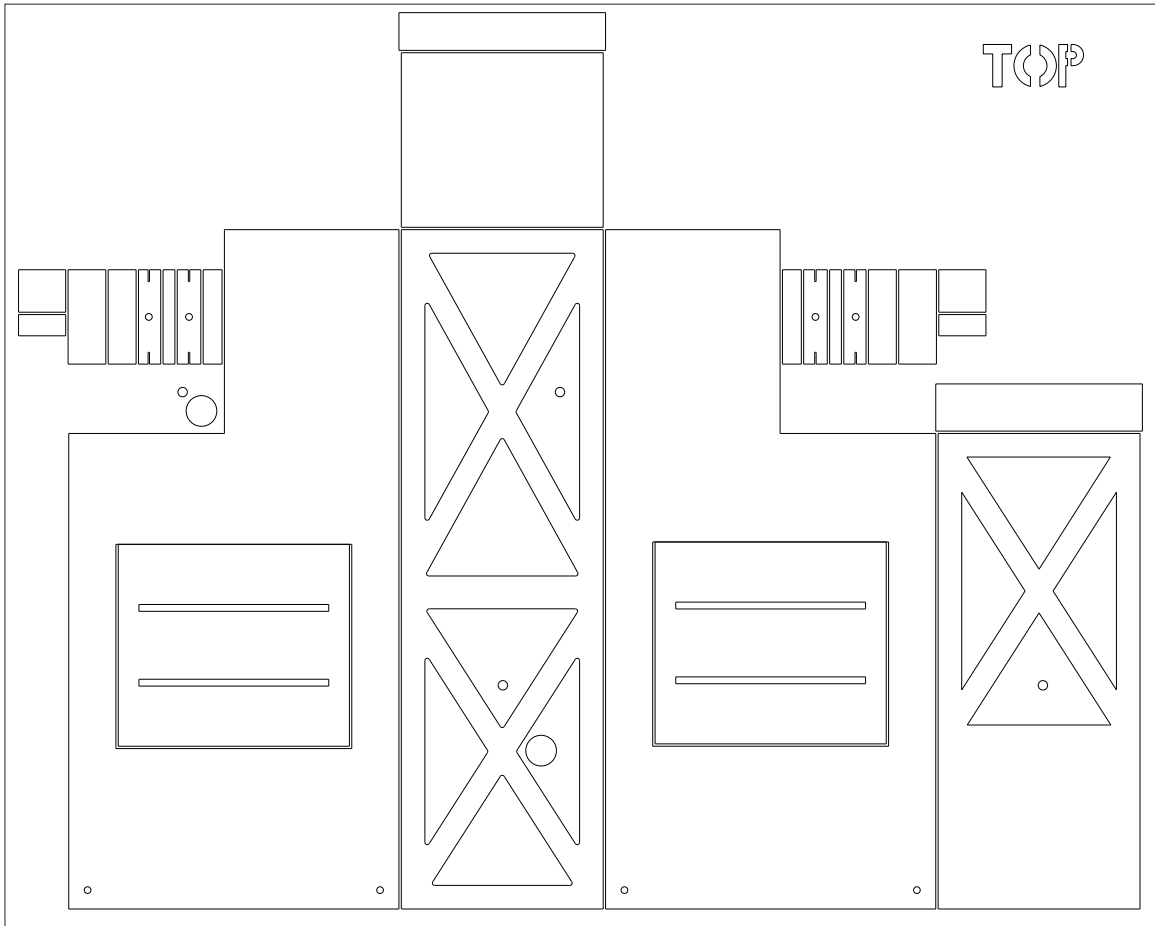
Figure A.6: The master layer created from the DXF file and used in the vector drawing software. Notice the addition of the alignment pin holes, fiducial holes, outer box, and top label.

A.6   Create the different required drawings

In this section a major departure is taken from the traditional machining of parts. The reason is the need to extensively modify the drawings made above to make them work with the SCM process. First, look at the step 1a and step 1b drawings. They are shown in the top row of Figure A.7. To create these parts, start from the step 1a layer containing a copy of the master layer. Delete all the features that are not adjacent to flexures in the final part except the alignment holes, fiducial holes, outside box, and top label. After these lines are deleted, close the holes for the flexures by drawing straight lines across the gaps to form pockets for the flexures to be created. This completes the step 1a drawing. To create the step 1b drawing copy the step 1a drawing to a new layer labeled step 1b and mirror the layer horizontally. This completes the step 1a and 1b drawings.

Next, for the step two drawing shown in the lower left corner of Figure A.7. In this drawing, all the lines are deleted that are adjacent to the flexures. This step represents the final cutout of the part from the outer box, so it is imperative that the flexures are not cut. Once the lines adjacent to the flexures are removed lines need to be drawn to complete the outline of all the features. This is typically short straight lines across the top and bottom of each flexure. Also, in this drawing alternating square-wave like edges can be created on the outlines where carbon fiber will eventually be folded up and attached to carbon. This makes for easier to assemble components and helps keeping alignment perfect during manufacturing. These square-wave structures are made to 0.25 mm by 2 mm alternating between the two edges to be joined. They can be seen in the top piece and the front and left sides of the part shown in Figure A.7.

Last, a drawing needs to be made for the Kapton layer. This is done by removing all lines from the master copy except for the alignment circles, fiducial circles, outer box, and top label. This completes the preparation of the four different required drawings.
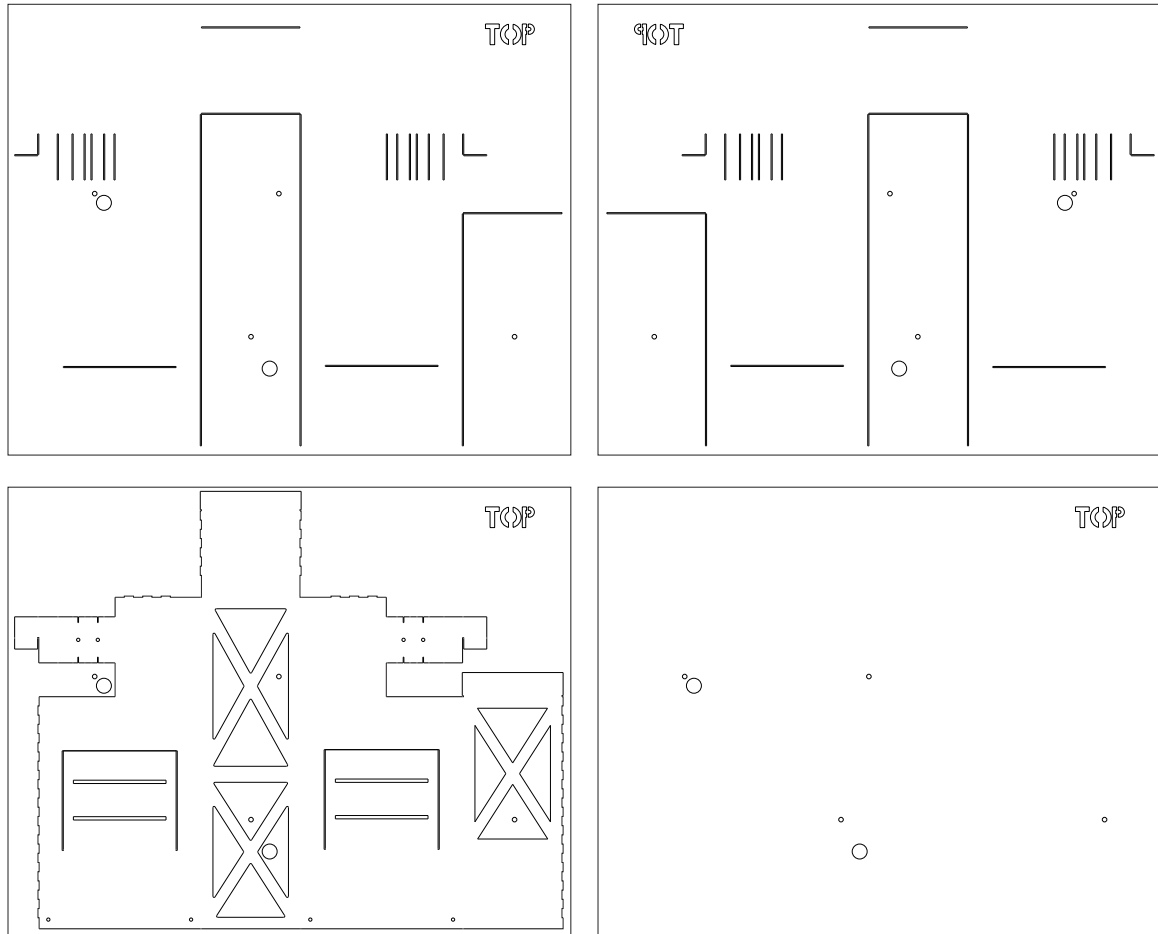
Figure A.7: Drawings prepared for import into Circuit CAM software. Top row step 1a and step 1b drawings, bottom row step 2 and Kapton drawings.

A.7   Export the drawings from the previous step to DXF format

Now, each individual drawing created in the previous step needs to be exported
to DXF format. To do this, select the layer and drawing within Corel Draw, and go
to "File" → "export." Pick a location and name for the part and click "Export." In
the next pop-up dialog make sure the units are millimeters and click "OK." Do this
for each of the four drawings created previously. Naming the files with some sort of
convention, for example "FWMAV_Fuselage_step1a.dxf," will help in the future steps.

A.8   Import the DXF file into Circuit CAM software

Next, open up the Circuit CAM software. Import the DXF file by going to
"File" → "Import." A pop-up should appear showing the content being imported, as
shown in Figure A.8. Make sure the imported file looks appropriate and click "OK."
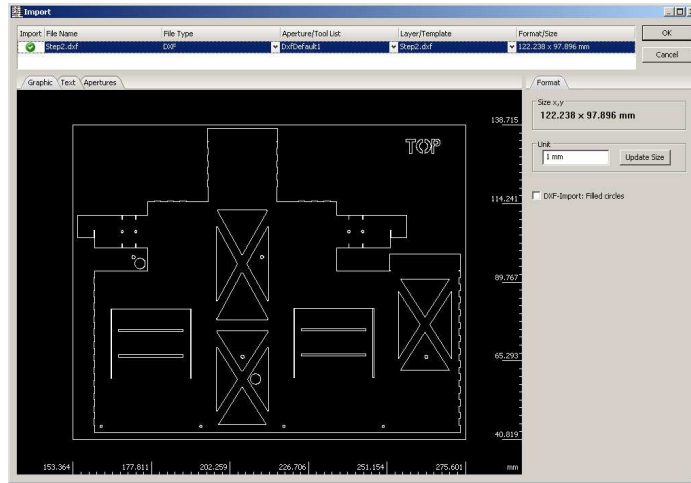
Figure A.8: The Circuit CAM import dialog popup box.

A.9   Close paths in Circuit CAM

The lines imported into Circuit CAM are considered "Open Paths" and the software only works with "Closed Paths." To close the paths, select each line and press "Shift+W." When performing this procedure be careful to close the paths of objects that contain paths. The outside path needs to be closed separately from all the internal paths. If closing all the paths at the same time is attempted, the internal paths will vanish.

A.10   Move paths to appropriate layers

Now that the paths are closed, the paths need to be moved to the appropriate layers. During step 1a, step 1b, and Kapton layer construction all the paths can be moved to the "ProtoLaserTop Contour" layer. Moving the paths to different layers allows the next piece of software (Circuit MASTER) to see the paths and assign different cutting settings on the paths. For step 2 parts, move the outside box, fiducial circles, alignment circles, and top label to the "ProtoLaserTop Hatch" layer. Move the actual cuts that are going to be made to the "Top Contour" layer. Finally, using the circle drawing tool, draw four 1 mm diameter circles on the fiducial layer, placing them directly on the fiducial circles. Additionally, for parts with different materials

121
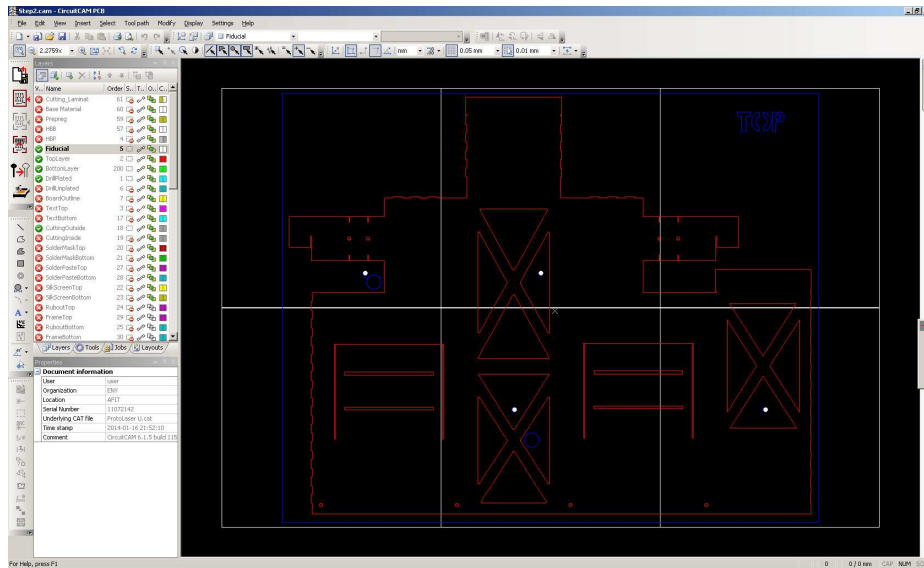
Figure A.9: An example of a step 2 file properly prepared in Circuit CAM.

to be cut, for example the Mylar of a wing and carbon fiber of the wing base, move the two different types of cuts to different layers. Figure A.9 shows a prepared step 2 part.

A.11 Prepare for laser scanning software

Last, go to "Tool path" → "Laser Scanner..." within the CircuitCAM software. This step will create squares on the part representing the laser scanner cutting field. A pop-up dialog shown in Figure A.10 will appear. On this dialog select the layer that has the largest dimensions, typically "ProtoLaserTop Contour" or "ProtoLaserTop Hatch." Additionally if there are fiducials being used, step 2 parts, and the fiducial circles happen to land on the lines separating the scanning fields, be sure to check the box "Cover fiducials on layer:" to prevent issues later with Circuit Master. The part is now ready to be exported to Circuit Master which is done by selecting "File" → "Export" → "LPKF" → "LPKF Proto Laser U." This will then import the file automatically into Circuit Master. Make sure Circuit Master is open and the laser has been warmed up, these steps will be covered in the next appendix.
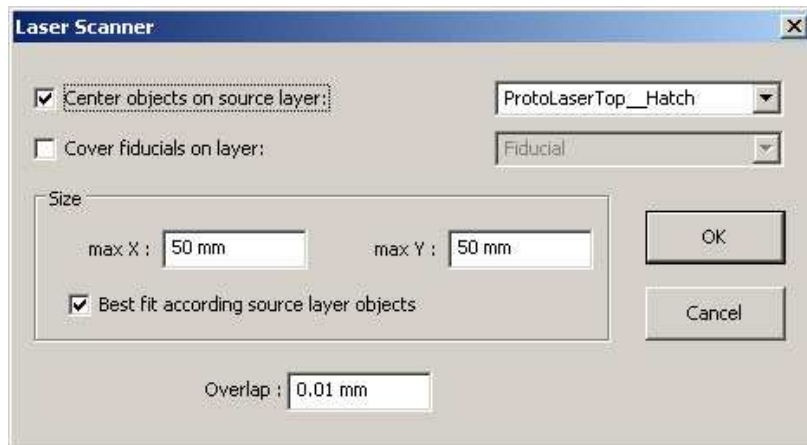
Figure A.10: The Circuit CAM laser scanner dialog box

Appendix B. AFIT FWMAV Smart Composite Manufacturing Process

The AFIT SMC process has evolved as the equipment, materials, and procedures have evolved. Presented in this appendix is the current methodology in creating FWMAV's at AFIT using the SCM process. This process utilizes a variety of specific materials and tools.

1. Carbon fiber

    The current ultra high strength carbon fiber AFIT uses was from Patz Materials and Technologies pre-impregnated with resign with the following specs and pricing:

    - Material: PMT-F6/YSH70 3K, 12 inch wide

    - FAW: 50gsm $\pm$3gsm

    - RC: 40% $\pm$5%

    - Minimum Qty: 300 ft^2

    - Price: \$20.50/ft^2

    This carbon fiber tape was cut into square sheets when received and then placed in a freezer to preserve the carbon fiber until used. The carbon fiber sheets have a backing material that prevents them from sticking together.

2. Pyralux

    Pyralux is a sheet adhesive that is used to bond layers of cooked carbon fiber to Kapton film. The specific Pyralux used is FR 1500. The last quote for purchase had a roll of 50 square feet cost \$195 and a roll of 100 square feet cost \$390. The Pyralux has a backing paper attached which gives the film strength until used.

3. Porous Teflon coated fiber glass

    This will be referred as porous Teflon and is used in the curing of the carbon fiber and also in the laser micromachining process.

4. Non-porous Teflon coated fiber glass

   This will be referred as non-porous Teflon and is used in the curing of carbon fiber, curing of Pyralux to carbon fiber, the bonding of the carbon fiber/Kapton layers, and also in the laser micromachining process.

5. Kapton film

   Two different sizes of Kapton HN films are used. For most construction the thinnest sized 12.5 micron Kapton is used as flexures. In the production of the wing/passive rotation part, a thicker 25 micron Kapton film is used. The Kapton comes on rolls and is cut into sheets before laser micromachining parts.

6. Mylar film

   The Mylar film is a thinner film than Kapton, only 2.5 micron thick and comes in small circular pre-cut sheets. It is used as the membrane in the wings. The excess is then cut away using through laser micromachining.

7. Bleeder cloth

   The bleeder cloth used is Airweave SS FR, which is a fire retardant polyester bleeder cloth. This cloth is used in the curing of the carbon fiber process and absorbs the extra resign in the pre-impregnated carbon fiber when the carbon fiber is placed in a heated press.

8. LPKF Multipress

   The multipress is a heated press that is used to cure the carbon fiber, attach the Pyralux, and bond the carbon fiber/Kapton layers together. The press has many specific plates which have a specific order of stacking as well as many different programed settings. These details will be covered later.

9. LPKF Proto Laser U

   This is the laser used to cut the carbon fiber, Kapton, and Mylar. It uses a software program called Circuit Master to operate. Its specific operation will

125

be covered later. The laser also uses a vacuum to provide suction to keep parts flat and remove ablated materials during laser micromachining.

The overall SCM process is a complex multi-step procedure. The steps will be covered in the order they would need to be performed. Not all parts require all steps. Some parts, such as the angle of attack stops, do not require folding, and thus do not need Pyralux or Kapton. For these parts omit the steps of the process that involve the adhesion of Pyralux, Kapton, and additional layers of carbon fiber. The overall steps required are listed below:

1. Carbon fiber curing

2. Pyralux adhesion

3. Laser micromachining step 1 and Kapton

4. Temporarily align and bond step 1 and Kapton

5. Permanently bond step 1 and Kapton

6. Laser micromachining step 2

7. Assemble prototype

B.1   Carbon Fiber 0-90-0 Preparation

In this step three layers of carbon fiber will be laid up and then cured in the Multipress heated press. First, the three sheets need to be cut down in size from the 12 inch by 12 inch squares into the 8 inch by 11 inch pieces. Figure B.1 shows the template used to cut the carbon. In this example the carbon was cut with the fibers in the longer direction. This is used for the first and third layers of carbon. The second layer of carbon is cut with the fibers aligned in the shorter direction. A rolling wheel fabric cutter is used to cut the carbon fiber out along the template. After the three layers of carbon fiber have been cut they should be stacked on non-porous Teflon and pressed together with the backing paper removed. This will make one sheet with the fibers oriented in a 0-90-0 degree layout. Next, the press plates need to be assembled

126
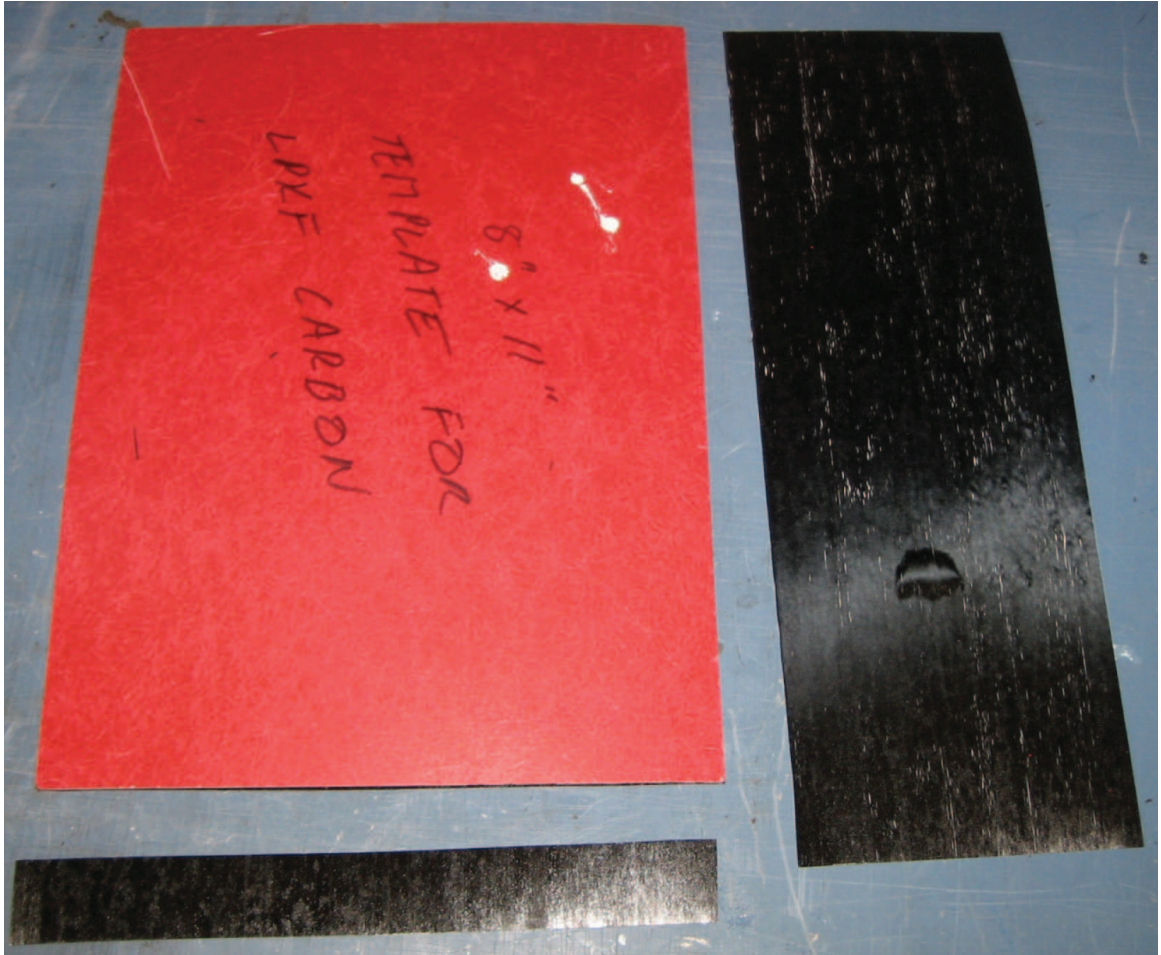
Figure B.1: Carbon cut from square sheet in the "0" direction utilizing the carbon cutting template.

to cure the carbon fiber. The plates starting with the bottom and working to the top have the following layers, the layers of Teflon should be cut to the dimension of the internal press plates and the bleeder cloth should be cut to be slightly larger than the carbon fiber sheets, but smaller than the Teflon sheets:

1. Blue felt pad

2. Bottom press plate

3. Internal pad

4. Bottom internal plate

5. Non-porous Teflon

6. Bleeder cloth

7. Porous Teflon

8. Three layer layup of carbon fiber

9. Porous Teflon

10. Bleeder cloth

11. Non-porous Teflon

12. Top internal plate

13. Internal pad

14. Top press plate

15. Blue felt pad

This assembled stack is placed into the press and the press is run using profile 1, pressing without preheating. To operate the press the up and down arrows navigate the menu, the right arrow is used as an "OK" button, and the left arrow is used as a "back" button. The press will go through a long heated pressing cycle followed by a cooling phase, which takes roughly 2.5 hours to complete. After the press has finished cooling the press will beep, press left arrow to stop the beeping and remove the plate

stack from the press. Disassemble the press plate stack and discard the used bleeder cloths. The porous Teflon will be used later in the laser micromachining phase, but should only be used once for curing carbon fiber. The non-porous Teflon can be used multiple times. Be sure to wear gloves when handling the blue felt pads as it extends the service life of the pads. When removing the layers of Teflon and bleeder cloth it is normal for the carbon to curl up some. Once the carbon is free of the Teflon and bleeder cloth it should lay flat again. This completes the creation of a sheet of cured carbon fiber. In a simple structure this carbon fiber sheet can be immediately machined into parts. For parts that will be folded into structures additional steps need be taken as follows.

B.2 *Pyralux Adhesion*

For more complex folding structures Pyralux is needed to bond the layers of carbon fiber and Kapton together. To attach Pyralux to a cured sheet of carbon fiber created in the previous step, start by cutting a sheet of Pyralux to the same dimensions as the cured carbon fiber. Next, carefully remove the backing paper from the Pyralux using either tweezers or small precision knife. The Pyralux tears very easily during this step. Some tears are fine but work slowly to minimize the number of tears in the Pyralux. The press can handle attaching Pyralux to up to six sheets of carbon fiber at a time, so it is most efficient to cure six sheets of carbon fiber first and then attach Pyralux to all of them at the same time. The press layup for Pyralux attachment is as follows:

1. Blue felt pad

2. Bottom press plate

3. Internal pad

4. Bottom internal plate

5. Non-porous Teflon

6. Cured carbon fiber 0-90-0 sheet

7. Pyralux with the backing paper removed

8. Non-porous Teflon

9. Cured carbon fiber 0-90-0 sheet

10. Pyralux with the backing paper removed

11. Non-Porous Teflon

   Repeat the layers of non-porous Teflon, carbon fiber, and Pyralux until all six or less sheets are stacked onto the plate. After the last sheet of non-porous Teflon:

12. Top internal plate

13. Internal pad

14. Top press plate

15. Blue felt pad

The press needs to be using profile 3 and should be preheated prior to adding the press plate stack into the press. The pressing and cooling process takes about 1.5 hours. When the press completes, remove and unstack the press plates. The Pyralux should now be attached to one side of each sheet of carbon fiber. These sheets of carbon fiber with Pyralux are now ready for laser micromachining.

B.3   Laser Micromachining Step 1 and Kapton

In this step the carbon fiber with Pyralux attached and Kapton will be laser micromachined. The software used for this is Circuit Master in conjunction with the LPKF ProtoLaser U. To start, the laser needs to complete a warmup cycle each time the Circuit Master software is opened. To accomplish this warmup procedure place a white partially porous vacuum backer board into the laser and close the door of the laser. Then within Circuit Master open the "startupsquare_pl u test.job" file, which is typically found in the recently opened files part of the file menu. Press the "All +" button near the top center of the Circuit Master software. This tells the software that every file that is currently placed in the cutting field will be processed. Next,

Figure B.2: The three pop-ups that are shown and used during the ProtoLaser U warmup procedure.

press the "Start" button. The laser will then pop-up a blue dialog box displaying the laser current state. Eventually, with the current configuration of the laser, there will be an fault. Click "Stop" when the fault shows, this will pop-up another dialog, select "Skip warmup." The laser will then continue its warmup procedure. Another fault will occur during warmup, repeat the work around by selecting "Skip warmup." When the laser finishes warming up it will perform the start up square cut, which is an extremely small, extremely low power part designed just for warming up the laser. Figure B.2 shows the screens and buttons used to by bypass the faults used during the warming up procedure.

Now, create a new file by hitting the new page button under the file menu. Don't save any changes made to the previous file. Next, depending on what part you are making, perform the last step discussed in the previous appendix to import a part to be cut. Circuit Master will ask which file to use for a tool file, see Table B.1 and select the appropriate tool file.

The part should now be visible in the cutting field of Circuit Master. Now, place the sheet to be cut on the vacuum board in the laser. If cutting carbon with Pyralux attached, place a sheet of used porous Teflon on the board first, and then place the

131

Type of material	Tool file
Kapton	O_KAPTON...
Carbon fiber	O_3LAYER...
Carbon fiber/Kapton/Carbon fiber	O_WING_CARBON

Table B.1: Material and tool files used in Circuit Master.

carbon fiber with the Pyralux side faced down. Turn the vacuum on and make sure the sheet is sucked down flat and is on the board square. Place strips of non-porous Teflon around the table covering the gap between the vacuum board and the table to force additional suction on the sheet. The laser is now prepared to cut the part.

Back in Circuit Master go to "Job" → "Tool Assignment..." and make sure every step has a tool assigned to it. Next, in "Job" → "Material" → "Size..." set the thickness to 0.15 mm and check the box for auto-focus. Now in the Camera Image display click "QuickCheck." Load settings for the type of material being cut, file names "LindholmCarbon" work for a sheet of carbon fiber, "LindholmCKC" works for two sheets of carbon fiber with Kapton in the middle layer, "Nonporous" works well for cutting Kapton. Next, using the arrows and text box at the top of Circuit Master, find the edge of the sheet you are cutting by moving the table with the arrows and looking at the Camera Image screen. When the edge is found, move the cutting pattern to the edge by clicking the button to the right of the X coordinates at the top of Circuit Master, click and hold on the part, move the cursor so the edge of the part lines up with the cross hair, which is the edge of the sheet. Now, use the button to the left of the arrows, which appears to have 4 little arrows on it. This button will move the camera/laser to where ever you click in the field, click on the four corners of the part to be cut, and make sure the part is completely on material as opposed to the Teflon sheets or the vacuum board. The part is now ready to cut, if additional copies of the part are desired, the button to the right of the move part button can be pressed, click and drag on a part to copy it, and then repeat the alignment process to make sure the copied part is also completely on the material. Finally, click the "All +" button followed by the "Start" button. The laser will then auto-focus on each

scan field and then fire the laser according to the tool settings. When the laser is complete it will pop-up a dialog stating job complete and how long it took, close the dialog. Press the button to the left of the Start button in the top row, this moves the table close to the laser door. When the table stops moving, shut the vacuum off and remove the part. Using a sharp pick or knife, poke out any features that should have been removed but are just stuck. This entire process is the same for Kapton or carbon fiber, the only difference is the carbon fiber has the layer of used porous Teflon below it and the laser makes more passes cutting it.

B.4 Temporarily Align and Bond Step 1 and Kapton

Once the step 1a, step 1b, and Kapton parts are cutout, they need to be aligned and temporarily bonded together. An adhesive stick is used for this along with some machined blocks with alignment pins. Start by putting adhesive on the Pyralux side of one of the sheets of carbon fiber, take care to avoid getting glue in the pockets cutout in the part. Place the carbon sheet on the alignment block. Next place the Kapton part onto the alignment block, making sure the label Top lines up. Last, put adhesive on the second sheet of carbon fiber (on the Pyralux side) and place onto the alignment block. Firmly press the three layers together, then remove from the alignment block.

B.5 Permanently Bond Step 1 and Kapton

The next step is to permanently bond the three layers together by using the press to activate the Pyralux. Set the press plates up as follows:

1. Blue felt pad

2. Bottom press plate

3. Internal pad

4. Bottom internal plate

5. Non-porous Teflon

6. Aligned and temporarily bonded parts

7. Non-porous Teflon

8. Top internal plate

9. Internal pad

10. Top press plate

11. Blue felt pad

If making wings and using Mylar, the Mylar just needs to be placed on the non-porous Teflon before the part and smoothed out. Then place the part on top the Mylar, no Pyralux is required to adhere the Mylar to the carbon fiber. Also, when making wings, shims are needed to support the wing venation during the press process. To make these shims, use the wing membrane shape of carbon cutout in step 1b, along with a wing membrane shape of non-porous Teflon. Place the non-porous Teflon into the wing section of the part followed by the carbon fiber wing shape, Pyralux down. This completes the shim. These shims can be reused and after the first use the non-porous Teflon sticks to the carbon fiber shim making their use easier. Run profile 2 on the press without a preheat cycle. When the press completes in about 2 hours, dissemble the stack and remove the permanently bonded parts. If bonding wings, leave the shim in place until after the next section is complete.

B.6   Laser Micromachining Step 2

This step is performed the same way step 1 was performed with some slight additions and changes. First, use the vacuum board with alignment pins placed on them. Then export the step 2 file from Circuit CAM into Circuit Master. For tool assignment, be sure to set the hatch layer to "Hatch no laser," any carbon to be cut to "Wing base," and any Mylar to be cut to "Mylar."

Next, go to the Camera image, quick check, and load the settings "Lindholm-CKC." Next, in the Camera image, Options, set the percentages to 40 and check

the box to confirm fiducial placement. Now turn on the vacuum and place sheets of non-porous Teflon covering the vacuum board except for the part to be cut.

Now align the part in Circuit Master with the part on the board as was done before. Next, click "Add +" and then "Start." The laser will then perform an auto-focus for each scanning field, then it will do the fiducial alignment. For each fiducial, the computer vision system will try to automatically align, however, it typically does a poor job since it was designed to find dark circles on light surfaces and this is the exact opposite. After it tries to find each fiducial a pop-up dialog will appear with arrows and a text box. Use these arrows to move the cross hairs in the Camera image to the fiducial, use the text box to change how far the camera moves with each arrow press. This step is vital to get properly finished parts. After the four fiducials have been identified one of two things happens. The desirable event is the laser starts cutting and eventually reports when it is complete. The other option is it will report the fiducials were too far out of specifications. If this happens, repeat the above steps by pressing "All +" again followed by "Start." If this does not correct the problem typically the vacuum system needs a filter to be changed out. If that does not resolve the issue, the camera image system may need recalibration. The manual for Circuit Master is on the computer and contains procedures for this, or contact LPKF and they can walk through the computer vision calibration steps.

Once the laser successfully completes the part, turn the vacuum off and remove the part, use a sharp pick or knife to remove any parts not quite cut completely through, or you can repeat the cutting process. The settings are fairly conservative to prevent excessive burning on the vacuum board, so typically the parts need a little bit of manual work to remove pieces. For wings, you should use a knife to scratch off any Mylar that is covering the passive rotation joint area, and use a sharp pick to slide between the shim and wing veins to remove the shim.

The part is now complete and ready to be part of an assembly.

B.7 Assemble Prototype

Assembling the prototype varies depending on if it is single-wing, multi-wing, commercial actuators vs. custom actuators, etc. Some guidelines will be given in this section to assist with any kind of assembly.

- Make shims according to the assembled prototype in CAD and use for alignment and placement of floating parts like actuators

- Very thin cyanoacrylate, or super glues work best for flowing into flexures that need to be fixed

- Thicker cyanoacrylate can be added to dried joints for strength reinforcement or for filling any potential gaps

- Use extreme caution when gluing around eventual flexible joints like the linkage and passive rotation joint, these parts will be ruined if glue gets on the flexures

- Clamping tweezers in third-hand vices are useful to fix the prototype to a certain geometry before gluing

- Use a stiff wire or needle to apply glue

- Incorporate items like e-clips and pin alignment holes to assist in assembly

Appendix C. *MATLABCode Overview for Static Testing*

The code presented in this appendix will be shown in abbreviated form with focus on the inputs, outputs, and utility of the given code structure. The code structure has been designed from the standpoint of reusability and flexibility. This code was designed to run with MATLAB 2011b, 32-bit version. Newer versions of MATLAB and the 64-bit version use a different method of interfacing with the NI ADC/DAC box. The code could be updated with minimal impact to most of the scripts and functions.

C.1 *SWF_FRF_BD.m*

This code that will capture data used to create and model the FRFs of a single-wing flapper or for a single wing of a FWMAV as seen in Figures 4.4 and 5.5. The code is run as a script, BD stands for bias drive. There are versions for running the actuators in a non-bias drive which follow the same with only slightly different structure. The inputs are all set as values near the top of the script. Recommended values are for a single-wing flapper mechanism. The key output is a mat file to be used with the EZERA eigenstructure realization program to model the FRF, which then allows for the collection of the parameters required for the DHPC-BABM control scheme.

Inputs		
Variable	**Description**	**Recommended Value**
plotFlag	1 plot,0 no plot	1
simFlag	1 sim data, 0 collect data	0
maxVAC	maximum voltage AC	200
Bias	bias voltage	100
amp	amplitude in %	0.05
avg	# of averages	10
overlap	% of overlap	0.50
simNoise	% of noise for sim	0.05
SampleSeconds	time for test	60
TareSeconds	time for tare	1
desiredCutFreq	max frequency	70
eraName	file name use with EZERA	–

Outputs	
Variable	**Description**
H1_Y1	H1 FRF
H2_Y1	H2 FRF
AVG_CX1_Y1	Coherence
era mat file	mat file named in input

NI DAQ Configuration	
Outputs (DAC)	
Channel	**Cable**
0	Bias Signal
1	Drive Signal
Inputs (ADC)	
Channel	**Cable**
22	Displacement
21	Measured Drive Signal

C.2 SWF_Test_BD.m

This code will capture data of varying BABM parameters, frequencies, or a single test run for a single-wing flapper using the bias drive configuration. There is a similar code for non-bias drive and for a FWMAV called Static_MAV_Test. The code is run as a script the inputs are all set as values near the top of the script. This script will call a function which will run each test specified in the script. That function will call another function which runs each test the specified number of samples desired. The split-cycle mat file contains frequency response data variables "H1" and "H2" which are at the resonant frequency and twice resonant frequency. Typically these values are obtained by interrogating the FRF model created using ERA. The test matrix input is a variable named "TM" that contains one test configuration per row. The first column is the amplitude, the second is the split-cycle parameter, and the third is the bias. All input and output data are stored into a data structure named "data."

	Inputs	
Variable	**Description**	**Recommended Value**
Split-cycle	file with split-cycle data	–
Test matrix	file test matrix	–
maxVAC	maximum allowed voltage AC	200
Bias	bias voltage	100
samples	number of samples for each test	5
simFlag	1 sim data, 0 collect data	0
testFlag	0 single, 1 varying freq., 2 test matrix	–
w	single or range of frequencies	first resonance
eta	bias value for test case 0/1	–
AR	amplitude for test case 0/1	–
tauR	split-cycle parameter for test case 0/1	–

Outputs	
Variable	**Description**
data	top data structure
data.Test	array of structures one for each test in test matrix
data.Test(#).BABM	structure of stored inputs of BABM parameters
data.Test(#).Raw	structure of all recorded input vectors and output vectors
data.Test(#).ave	structure of cycle-averaged output data
data.Test(#).sigma	structure of the standard deviations of cycle-averaged data
data.Test(#).S	structure of sampling rate and timing data
data.Test(#).Units	structure of units the data is in

NI DAQ Configuration	
Outputs (DAC)	
Channel	**Cable**
0	Bias Signal
1	Drive Signal
3	Trigger for Video
Inputs (ADC)	
Channel	**Cable**
0	Bias Voltage
1	Bias Current
2	Drive Voltage
3	Drive Current
6	Nano17 Channel 1
7	Nano17 Channel 2
16	Nano17 Channel 3
17	Nano17 Channel 4
18	Nano17 Channel 5
19	Nano17 Channel 6
22	Displacement

C.3   BABM.m

This code will be presented in its entirety as it forms the DHPC based split-cycle wave forms key in the BABM control scheme. This function can be placed into any other code to create the open-loop wing trajectory drive signal. The function itself contains two other functions "DHPC" and "biharmonic_gen." These functions are used in the construction of the DHPC split-cycle waveform. The inputs and outputs of the function are shown below:

Inputs		Outputs	
Variable	**Description**	**Variable**	**Description**
t	vector of time	VR	drive signal right wing
w	ω in rad/sec	VL	drive signal left wing
BABMs	input parameters		
BABMs.eta	η		
BABMs.tauR	τ right wing		
BABMs.tauL	τ left wing		
BABMs.AR	A right wing		
BABMs.AL	A left wing		
BABMs.const	DHPC Constants		
BABMs.const.M1pR	M_1 right wing		
BABMs.const.M2pR	M_2 right wing		
BABMs.const.M1pL	M_1 left wing		
BABMs.const.M2pL	M_2 left wing		
BABMs.const.beta1pR	β_1 right wing		
BABMs.const.beta2pR	β_2 right wing		
BABMs.const.beta1pL	β_1 left wing		
BABMs.const.beta2pL	β_2 left wing		

```
function [VR VL] = BABM(t,w,BABMs)
%% BABM.m
% Garrison Lindholm
% 21 September 2011
% Changelog:
% 18 May 2012 structure input
%
% Summary: Function is designed to take the desired signal length,
```

141

```matlab
% drive frequency, BABM parameters, and FRF plant information and
% then output the DHPC compensated signals corresponding to the
% BABM parameters. Both DHPC and BABM techniques and terminology
% is from Michael Anderson's work on FWMAV during is Ph.D.
% research.

tauR = BABMs.tauR;
tauL = BABMs.tauL;
AR = BABMs.AR;
AL = BABMs.AL;
eta = BABMs.eta;
M1pR = BABMs.const.M1pR;
M2pR = BABMs.const.M2pR;
M1pL = BABMs.const.M1pL;
M2pL = BABMs.const.M2pL;
beta1pR = BABMs.const.beta1pR;
beta2pR = BABMs.const.beta2pR;
beta1pL = BABMs.const.beta1pL;
beta2pL = BABMs.const.beta2pL;


VR = AR.*(DHPC(tauR,M1pR,M2pR,beta1pR,beta2pR,w,t)+eta);
VL = AL.*(DHPC(tauL,M1pL,M2pL,beta1pL,beta2pL,w,t)+eta);


function V = DHPC(tau,M1p,M2p,beta1p,beta2p,w,t)
%% DHPC
% Garrison Lindholm
% 21 September 2011
% Inputs:
%   tau:        stroke reversal time shift
%   M1p—beta2p: FRF plant parameters
%   w:          flapping frequency
%   t:          desired length of signal (time)
% Outputs:
%   V:          DHPC compensated signal for desired tau
```

142

```matlab
[M1 beta1 M2] = biharmonic_gen(tau);


M1pc = M1/M1p;
M2pc = M2/M2p;
beta1pc = beta1-beta1p;
% beta2pc = beta2-beta2p; % Not needed


V = M1pc.*cos(w.*t+beta1pc)-M2pc.*sin(2.*w.*t+2.*beta1pc);
V = V./max(abs(V));
V = V.';


function [M1 beta1 M2 beta2] = biharmonic_gen(tau)
%% biharmonic_gen
% Garrison Lindholm
% 21 September 2011
% Inputs:
%   tau:        stroke reversal time shift
% Outputs:
%   M1-beta2: approximated phasor form of 2-term fourier
%             transform of a split cycle waveform
M1 = cos(2*tau);
M2 = 0.34*sin(3.3*tau);
beta1 = -2*tau;
beta2 = -4*tau+pi/2;
```

Appendix D.   Thrust Data for Figures 5.4 and 5.7

The tables presented in this appendix contain all the data collected to calculate $\partial T/\partial \tau$ shown in Figures 5.4 and 5.7.

Table D.1: Cycle-averaged thrust vs. angle of attack stop and split-cycle parameter

Angle of Attack Stop (deg)	Cycle Averaged Thrust (gF)				
30	-0.069	-0.052	-0.045	-0.043	-0.032
40	-0.053	-0.035	-0.020	-0.018	0.003
45	0.004	0.018	0.024	-0.015	-0.001
50	0.002	-0.011	-0.015	-0.025	-0.034
60	0.064	0.064	0.034	-0.004	-0.014
Split-Cycle Parameter (τ)	-0.050	-0.025	0.000	0.025	0.050

Table D.2: Cycle-averaged thrust vs. passive rotation joint stiffness and split-cycle parameter

Rotation Joint Stiffness (xOriginal)	Cycle Averaged Thrust (gF)				
1.00	0.004	0.018	0.024	-0.015	-0.001
1.25	-0.020	-0.028	-0.032	-0.039	-0.045
1.50	-0.028	-0.028	-0.039	-0.058	-0.040
2.00	-0.015	-0.001	-0.016	-0.034	-0.035
2.50	0.012	0.004	-0.006	-0.018	-0.025
3.00	-0.024	-0.030	-0.037	-0.044	-0.050
Split-Cycle Parameter (τ)	-0.050	-0.025	0.000	0.025	0.050

Bibliography

1. Anderson, M. L., Sladek, N. J., and Cobb, R. G., "Evaluation of Bi-Harmonic Amplitude and Bias Modulation for Flapping Wing MAV Control," *Proceedings from the 49th AIAA Aerospace Sciences Meeting including the New Horizons Forum and Aerospace Exposition*, 1/4 2011.

2. Ellington, C. P. and Ellington, C. P., "The aerodynamics of hovering insect flight. I. The quasi-steady analysis," *Philosophical Transactions of the Royal Society of London. B, Biological Sciences*, Vol. 305, No. 1122, 1984, pp. 1–15.

3. Ellington, C. P., "The novel aerodynamics of insect flight: applications to micro-air vehicles," *Journal of Experimental Biology*, Vol. 202, No. 23, 1999, pp. 3439–3448.

4. Dickinson, M. H., Lehmann, F. O., and Sane, S. P., "Wing rotation and the aerodynamic basis of insect flight," *Science*, Vol. 284, No. 5422, 1999, pp. 1954–1960.

5. Sane, S. P. and Dickinson, M. H., "The control of flight force by a flapping wing: lift and drag production," *Journal of experimental biology*, Vol. 204, No. 15, 2001, pp. 2607–2626.

6. Khan, Z. A. and Agrawal, S. K., "Force and moment characterization of flapping wings for micro air vehicle application," *Proceedings of the 2005 American Control Conference*, IEEE, 2005, pp. 1515–1520.

7. Ansari, S. A., Żbikowski, R., and Knowles, K., "Aerodynamic modelling of insect-like flapping flight for micro air vehicles," *Progress in Aerospace Sciences*, Vol. 42, No. 2, 2 2006, pp. 129–172.

8. Adity, K. and Malolan, V., "Investigation of strouhal number effect on flapping wing micro air vehicle," *Proceedings from the 45th AIAA Aerospace Sciences Meeting and Exhibit*, 1/8 2007.

9. Whitney, J. P. and Wood, R. J., "Aeromechanics of passive rotation in flapping flight," *Journal of Fluid Mechanics*, Vol. 660, No. 1, 2010, pp. 197–220.

10. Tekell, J. P., "Reynolds Number Effects on Thrust Coefficients and PIV for Flapping Wing Micro Air Vehicles," Tech. rep., DTIC Document, 2012.

11. DeLuca, A. M., "Aerodynamic Performance and Particle Image Velocimetery of Piezo Actuated Biomimetic Manduca Sexta Engineered Wings Towards the Design and Application of a Flapping Wing Flight Vehicle," *Dissertation, Air Force Institute of Technology*, 2013.

12. Wood, R. J., Steltz, E., and Fearing, R. S., "Optimal energy density piezoelectric bending actuators," *Sensors and Actuators A: Physical*, Vol. 119, No. 2, 4/13 2005, pp. 476–488.

13. Fearing, R. S., Chiang, K. H., Dickinson, M. H., Pick, D. L., Sitti, M., and Yan, J., "Wing transmission for a micromechanical flying insect," *Proceedings of the 2000 IEEE International Conference on Robotics and Automation*, Vol. 2, IEEE, 2000, pp. 1509–1516.

14. Sitti, M., "PZT actuated four-bar mechanism with two flexible links for micromechanical flying insect thorax," *Proceedings of the 2001 IEEE International Conference on Robotics and Automation*, Vol. 4, IEEE, 2001, pp. 3893–3900.

15. Yan, J., Avadhanula, S., Sitti, M., Wood, R. J., and Fearing, R. S., "Thorax Design and Wing Control for a Micromechanical Flying Insect," *Proceedings from the 39th Annual Allerton Conf on Communication, Control and Computing*, Vol. 39, 2001, pp. 952–961.

16. Agrawal, S. K., Madangopal, R., and Khan, Z. A., "Biologically inspired design of small flapping wing air vehicles using four-bar mechanisms and quasi-steady aerodynamics," *Journal of Mechanical Design*, 2004, pp. 1–8.

17. Avadhanula, S., Wood, R. J., Steltz, E., Yan, J., and Fearing, R. S., "Lift force improvements for the micromechanical flying insect," *Proceedings from the IEEE/RSJ International Conference on Intelligent Robots and Systems*, Vol. 2, IEEE, 2003, pp. 1350–1356.

18. Mueller, T. J., Kellogg, J. C., Ifju, P. G., and Shkarayev, S. V., *Introduction to the design of fixed-wing micro air vehicles: including three case studies*, American Institute of Aeronautics and Astronautics, 2007.

19. Wood, R. J., Steltz, E., and Fearing, R. S., "Nonlinear performance limits for high energy density piezoelectric bending actuators," *Proceedings from the 2005 IEEE International Conference on Robotics and Automation*, IEEE, 2005, pp. 3633–3640.

20. Wood, R. J., "Design, fabrication, and analysis of a 3DOF, 3cm flapping-wing MAV," *Proceedings from the 2007 IEEE/RSJ International Conference on Intelligent Robots and Systems*, 2007, pp. 1576–1581.

21. Wood, R. J., Avadhanula, S., Sahai, R., Steltz, E., and Fearing, R. S., "Microrobot design using fiber reinforced composites," *Journal of Mechanical Design*, Vol. 130, No. 5, 2008.

22. Yan, J., Wood, R. J., Avadhanula, S., Sitti, M., and Fearing, R. S., "Towards flapping wing control for a micromechanical flying insect," *Proceedings from the IEEE International Conference on Robotics and Automation*, Vol. 4, 2001, pp. 3901–3908.

23. Wilson, N. and Wereley, N., "Experimental Investigation of Flapping Wing Performance in Hover," *Proceedings from the 48th AIAA/ASME/ASCE/AHS/ASC Structures, Structural Dynamics, and Materials Conference*, 4/23 2007.

24. Wood, R. J., "The first takeoff of a biologically inspired at-scale robotic insect," *IEEE Transactions on Robotics*, Vol. 24, No. 2, 2008, pp. 341–347.

25. Oppenheimer, M. W., Doman, D. B., and Sigthorsson, D. O., "Dynamics and Control of a Biomimetic Vehicle Using Biased Wingbeat Forcing Functions: Part I-Aerodynamic Model," *Proceedings of the 48th AIAA Aerospace Sciences Meeting Including the New Horizons Forum and Exposition*, 2010.

26. Doman, D. and Sigthorsson, M. O. D., "Dynamics and control of a biomimetic vehicle using biased wingbeat forcing functions: Part II-Control," *Proceedings of the 48th AIAA Aerospace Sciences Meeting Including the New Horizons Forum and Exposition*, 2010.

27. Doman, D. B., Oppenheimer, M. W., and Sigthorsson, D. O., "Wingbeat shape modulation for flapping-wing micro-air-vehicle control during hover," *Journal of guidance, control, and dynamics*, Vol. 33, No. 3, 2010, pp. 724–739.

28. Oppenheimer, M. W., Dornan, D. B., and Sigthorsson, D. O., "Dynamics and Control of a Minimally Actuated Biomimetic Vehicle: Part II-Control," *Proceedings of the AIAA Atmospheric Flight Mechanics Conference, Chicago, IL*, 2009.

29. Anderson, M. L., O'Hara, R. P., and Cobb, R. G., "Design, Fabrication, and Testing of an Insect-Sized MAV Wing Flapping Mechanism," *Proceedings from the 49th AIAA Aerospace Sciences Meeting*, 1/4 2011.

30. Whitney, J. P., Sreetharan, P. S., Ma, K. Y., and Wood, R. J., "Pop-up book MEMS," *Journal of Micromechanics and Microengineering*, Vol. 21, No. 11, 2011, pp. 115021–115027.

31. DeLeón, N. E. and Palazotto, A., "The Evaluation of a Biologically Inspired Engineered MAV Wing Compared to the Manduca Sexta Wing under Simulated Flapping Conditions," *International Journal of Micro Air Vehicles*, Vol. 3, No. 3, 2011, pp. 149–168.

32. DeLeón, N., "Manufacturing and Evaluation of a Biologically Inspired Engineered MAV Wing Compared to the Manduca Sexta Wing Under Simulated Flapping Conditions," Tech. rep., DTIC Document, 2011.

33. O'Hara, R. P., "The Material Property and Structural Dynamic Characterization of the Manduca Sexta Forewing for Application to Flapping Micro Air Vehicle Design," *Dissertation, Air Force Institute of Technology*, 2011.

34. O'Hara, R., DeLeón, N., and Palazotto, A., "Structural Identification and Simulation of the Manduca Sexta Forewing," *Proceedings of the 2011 AIAA Conference on Structures, Structural Dynamics, and Materials*, 2011.

35. Taylor, G. K. and Thomas, A. L. R., "Dynamic flight stability in the desert locust Schistocerca gregaria," *Journal of Experimental Biology*, Vol. 206, No. 16, 2003, pp. 2803–2829.

36. Taylor, G. K., Bomphrey, R. J., and Hoen, J., "Insect flight dynamics and control," *Proceedings of the 44th AIAA Aerospace Sciences Meeting and Exhibit*, 2006, pp. 1–12.

37. Sun, M. and Xiong, Y., "Dynamic flight stability of a hovering bumblebee," *Journal of experimental biology*, Vol. 208, No. 3, 2005, pp. 447–459.

38. Sun, M. and Wang, J. K., "Flight stabilization control of a hovering model insect," *Journal of Experimental Biology*, Vol. 210, No. 15, 2007, pp. 2714–2722.

39. Deng, X., Schenato, L., Wu, W. C., and Sastry, S. S., "Flapping flight for biomimetic robotic insects: Part I-system modeling," *Proceedings from the IEEE Transactions on Robotics*, Vol. 22, No. 4, 2006, pp. 776–788.

40. Deng, X., Schenato, L., and Sastry, S. S., "Flapping flight for biomimetic robotic insects: Part II-flight control design," *Proceedings from the IEEE Transactions on Robotics*, Vol. 22, No. 4, 2006, pp. 789–803.

41. Khan, Z. A. and Agrawal, S. K., "Control of Longitudinal Flight Dynamics of a Flapping-Wing Micro Air Vehicle Using Time-Averaged Model and Differential Flatness Based Controller," 01/01 2007.

42. Bolender, M. A., "Open-Loop Stability of Flapping Flight in Hover," *Proceedings from the AIAA Guidance, Navigation, and Control Conference*, 8/2 2010.

43. Faruque, I. and Humbert, J. S., "Dipteran insect flight dynamics. Part 1 Longitudinal motion about hover," *Journal of theoretical biology*, Vol. 264, No. 2, 5/21 2010, pp. 538–552.

44. Faruque, I. and Humbert, J. S., "Dipteran insect flight dynamics. Part 2: Lateral–directional motion about hover," *Journal of theoretical biology*, Vol. 265, No. 3, 8/7 2010, pp. 306–313.

45. Rakotomamonjy, T., Ouladsine, M., and Moing, T. L., "Longitudinal modelling and control of a flapping-wing micro aerial vehicle," *Control Engineering Practice*, Vol. 18, No. 7, 7 2010, pp. 679–690.

46. Yilmaz, A., "Design and Development of a Flapping Wing Micro Air Vehicle," *Swiss Federal Institute of Technology Zurich, Autonomous Systems Lab*, 2010.

47. Ellington, C. P., "The aerodynamics of hovering insect flight. IV. Aerodynamic mechanisms," *Philosophical Transactions of the Royal Society of London. B, Biological Sciences*, Vol. 305, No. 1122, 1984, pp. 79–113.

48. Dickinson, M., "The effects of wing rotation on unsteady aerodynamic performance at low Reynolds numbers," *Journal of experimental biology*, Vol. 192, No. 1, 1994, pp. 179–206.

49. Byl, K., "A passive dynamic approach for flapping-wing micro-aerial vehicle control," *ASME Dynamic Systems and Control Conference, Cambridge, Massachusetts, USA*, 2010, pp. 13–15.

50. Serrani, A., "Robust hovering control of a single-DOF flapping wing MAV," *American Control Conference (ACC), 2010*, IEEE, 2010, pp. 1302–1307.

51. Mahjoubi, H. and Byl, K., "Steering and horizontal motion control in insect-inspired flapping-wing MAVs: the tunable impedance approach," *American Control Conference (ACC), 2012*, IEEE, 2012, pp. 901–908.

52. Rakotomamonjy, T., Ouladsine, M., and Moing, T. L., "Modelization and kinematics optimization for a flapping-wing microair vehicle," *Journal of Aircraft*, Vol. 44, No. 1, 2007, pp. 217–231.

53. Orlowski, C. T. and Girard, A. R., "Modeling and simulation of nonlinear dynamics of flapping wing micro air vehicles," *AIAA journal*, Vol. 49, No. 5, 2011, pp. 969–981.

54. Orlowski, C. T. and Girard, A. R., "Longitudinal Flight Dynamics of Flapping-Wing Micro Air Vehicles," *Journal of Guidance, Control, and Dynamics*, Vol. 35, No. 4, 2012, pp. 1115–1131.

55. Pérez-Arancibia, N. O., Whitney, J. P., and Wood, R. J., "Lift force control of a flapping-wing microrobot," *Proceedings of the 2010 American Control Conference (ACC)*, IEEE, 2011, pp. 4761–4768.

56. Pérez-Arancibia, N. O., Whitney, J. P., and Wood, R. J., "Lift force control of flapping-wing microrobots using adaptive feedforward schemes," *IEEE/ASME Transactions on Mechatronics*, IEEE, 2013, pp. 155–168.

57. Pérez-Arancibia, N. O., Ma, K. Y., Galloway, K. C., Greenberg, J. D., and Wood, R. J., "First controlled vertical flight of a biologically inspired microrobot," *Bioinspiration & Biomimetics*, Vol. 6, No. 3, 2011.

58. Karpelson, M., Whitney, J. P., Wei, G. Y., and Wood, R. J., "Energetics of Flapping-wing Robotic Insects: Towards Autonomous Hovering Flight," *2010 IEEE/RSJ International Conference on Intelligent Robots and Systems (IROS)*, IEEE, 2010, pp. 1630–1637.

59. Avadhanula, S., *Design, Fabrication and Control of the Micromechanical Flying Insect*, Ph.D. thesis, University of California, Berkeley, 2007.

60. Lin, S. H., Hsiao, F. Y., Chen, C. L., and Shen, J. F., "Altitude control of flapping-wing MAV using vision-based navigation," *American Control Conference (ACC), 2010*, IEEE, 2010, pp. 21–26.

61. Baek, S. S., Garcia Bermudez, F. L., and Fearing, R. S., "Flight control for target seeking by 13 gram ornithopter," *2011 IEEE/RSJ International Conference on Intelligent Robots and Systems (IROS)*, IEEE, 2011, pp. 2674–2681.

62. Richter, C. and Lipson, H., "Untethered hovering flapping flight of a 3D-printed mechanical insect," *Artificial life*, Vol. 17, No. 2, 2011, pp. 73–86.

63. Sunada, S., Hatayama, Y., and Tokutake, H., "Pitch, roll, and yaw damping of a flapping wing," *AIAA Journal*, Vol. 48, No. 6, 2010, pp. 1261–1265.

64. Grauer, J. A. and Hubbard, J. E., "Inertial measurements from flight data of a flapping-wing ornithopter," *Journal of Guidance, Control, and Dynamics*, Vol. 32, No. 1, 2009, pp. 326–331.

65. Zdunich, P., Bilyk, D., MacMaster, M., Loewen, D., DeLaurier, J., Kornbluh, R., Low, T., Stanford, S., and Holeman, D., "Development and testing of the mentor flapping-wing micro air vehicle," *Journal of Aircraft*, Vol. 44, No. 5, 2007, pp. 1701–1711.

66. Anderson, M. L. and Cobb, R. G., "Frequency Response of a Micro Air Vehicle Wing Flapping Mechanism to Non-Harmonic Forcing," *Proceedings from the 51st AIAA/ASME/ASCE/AHS/ASC Structures, Structural Dynamics, and Materials Conference*, 4/12 2010.

67. Anderson, M. L. and Cobb, R. G., "Toward Flapping Wing Control of Micro Air Vehicles," *Journal of guidance, control, and dynamics*, Vol. 35, No. 1, 2012, pp. 296–308.

68. Anderson, M. L. and Cobb, R. G., "Techniques for Non-Harmonic Wing Flapping for the Control of Micro Air Vehicles," *Proceedings from the AIAA Guidance, Navigation, and Control Conference*, 8/2 2010.

69. Woods, R. D., Liebst, B. S., and Cobb, R. G., "A state-space model of a large, lightly damped space structure," *Proceedings from the AIAA Guidance, Navigation and Control Conference*, 1995, pp. 345–355.

70. Cobb, R. G. and Liebst, B. S., "Structural damage identification using assigned partial eigenstructure," *AIAA Journal*, Vol. 35, No. 1, 1997, pp. 152–158.

71. Sladek, N. J., "Flapping Wing Micro Air Vehicle Wing Manufacture and Force Testing," *Thesis, Air Force Institute of Technology (AU), Wright-Patterson AFB OH*, 2013.

72. MathWorks®, "Tracking Cars Using Background Estimation," http://www.mathworks.com/products/computer-vision/code-examples.html?file=/products/demos/shipping/vision/viptraffic.html, Last accessed: 11 Feb 2014.

73. Pintaric, T. and Kaufmann, H., "A rigid-body target design methodology for optical pose-tracking systems," *Proceedings from the 2008 ACM symposium on Virtual reality software and technology*, 2008, pp. 73–76.

74. Jansen, C., Steinicke, F., Hinrichs, K., Vahrenhold, J., and Schwald, B., "Performance improvement for optical tracking by adapting marker arrangements," *Proceedings from the IEEE VR 2007 Workshop on Trends and Issues in Tracking for Virtual Environments*, 2007.

75. Steinicke, F., Jansen, C., Hinrichs, K., Vahrenhold, J., and Schwald, B., "Generating Optimized Marker-based Rigid Bodies for Optical Tracking Systems," *Proceedings from the 2nd International Conference on Computer Vision Theory and Applications*, 2007.

76. Bouguet, J. Y., "Camera calibration toolbox for matlab," *URL http://www. vision. caltech. edu/bouguetj/calib_doc*, 2009.

77. Heikkila, J. and Silven, O., "A four-step camera calibration procedure with implicit image correction," *Proceedings from the IEEE Computer Society Conference on Computer Vision and Pattern Recognition*, 1997, pp. 1106–1112.

78. Eggert, D. W., Lorusso, A., and Fisher, R. B., "Estimating 3-D rigid body transformations: a comparison of four major algorithms," *Machine Vision and Applications*, Vol. 9, No. 5, 1997, pp. 272–290.

79. Arun, K. S., Huang, T. S., and Blostein, S. D., "Least-squares fitting of two 3-D point sets," *IEEE Transactions on Pattern Analysis and Machine Intelligence*, Vol. 9, No. 5, 1987, pp. 698–700.

80. Horn, B. K. P., Hilden, H. M., and Negahdaripour, S., "Closed-form solution of absolute orientation using orthonormal matrices," *Journal of the Optical Society of America. A, Optics and image science*, Vol. 5, No. 7, 1988, pp. 1127–1135.

81. Horn, B. K. P., "Closed-form solution of absolute orientation using unit quaternions," *Journal of the Optical Society of America. A, Optics and image science*, Vol. 4, No. 4, 1987, pp. 629–642.

82. Walker, M. W., Shao, L., and Volz, R. A., "Estimating 3-D location parameters using dual number quaternions," *CVGIP: image understanding*, Vol. 54, No. 3, 1991, pp. 358–367.

83. Hart, M., "The Spherical Pendulum," http://www.maths.surrey.ac.uk/ explore/michaelspages/documentation/Spherical.pdf, Last accessed: 15 Feb 2014.

84. Lenzen, R. K., *Development of Optimized Piezoelectric Bending Actuators for Use in an Insect Sized Flapping Wing Micro Air Vehicle*, Ph.D. thesis, Air Force Institute of Technology, 2013.

Vita

Captain Garrison J. Lindholm graduated from Amery High School in Amery, WI. He entered undergraduate studies at the University of Minnesota in Minneapolis, MN where he graduated with a Bachelor of Science degree in Aerospace Engineering in May 2006. In October 2006 he was commissioned in the United States Air Force through ROTC.

He was assigned to the test engineering group at Edwards Air Force Base in CA. He served as a Global Hawk subsystems flight test engineer and hypersonic flight test engineer. While stationed at Edwards Air Force Base, he received his Master of Science degree in Engineering from California State Polytechnic University, Ponoma.

In January 2011 he entered the Graduate School of Engineering and Management at the Air Force Institute of Technology. Upon graduation he will be assigned to the Air Force Research Laboratory's, Capabilities Integration Division, Wright-Patterson Air Force Base, OH.

Permanent address: 1864 4th Street
HQ AFRL/XPR
Capabilities Integration Division
Wright-Patterson AFB, OH 45433

REPORT DOCUMENTATION PAGE

The public reporting burden for this collection of information is estimated to average 1 hour per response, including the time for reviewing instructions, searching existing data sources, gathering and maintaining the data needed, and completing and reviewing the collection of information. Send comments regarding this burden estimate or any other aspect of this collection of information, including suggestions for reducing the burden, to Department of Defense, Washington Headquarters Services, Directorate for Information Operations and Reports (0704-0188), 1215 Jefferson Davis Highway, Suite 1204, Arlington, VA 22202-4302. Respondents should be aware that notwithstanding any other provision of law, no person shall be subject to any penalty for failing to comply with a collection of information if it does not display a currently valid OMB control number.
PLEASE DO NOT RETURN YOUR FORM TO THE ABOVE ADDRESS.

1. REPORT DATE *(DD-MM-YYYY)*	2. REPORT TYPE	3. DATES COVERED *(From - To)*

4. TITLE AND SUBTITLE

5a. CONTRACT NUMBER

5b. GRANT NUMBER

5c. PROGRAM ELEMENT NUMBER

6. AUTHOR(S)

5d. PROJECT NUMBER

5e. TASK NUMBER

5f. WORK UNIT NUMBER

7. PERFORMING ORGANIZATION NAME(S) AND ADDRESS(ES)

8. PERFORMING ORGANIZATION REPORT NUMBER

9. SPONSORING/MONITORING AGENCY NAME(S) AND ADDRESS(ES)

10. SPONSOR/MONITOR'S ACRONYM(S)

11. SPONSOR/MONITOR'S REPORT NUMBER(S)

12. DISTRIBUTION/AVAILABILITY STATEMENT

13. SUPPLEMENTARY NOTES

14. ABSTRACT

15. SUBJECT TERMS

16. SECURITY CLASSIFICATION OF:			17. LIMITATION OF ABSTRACT	18. NUMBER OF PAGES	19a. NAME OF RESPONSIBLE PERSON
a. REPORT	b. ABSTRACT	c. THIS PAGE			
					19b. TELEPHONE NUMBER *(Include area code)*